

# TABLE OF CONTENTS

ABSTRACT.....	ii
ACKNOWLEDGEMENTS.....	iii
TABLE OF CONTENTS.....	iv
LIST OF FIGURES .....	vii
LIST OF TABLES.....	xv
Chapter 1 Introduction.....	1
1.1 Overview.....	1
1.2 Research Objective .....	2
1.3 Outline.....	3
1.4 References.....	4
Chapter 2 Literature Review.....	5
2.1 Fracture Mechanics.....	5
2.1.1 Introduction.....	5
2.1.2 Stress intensity approach.....	5
2.1.3 Energy release rate approach .....	9
2.1.4 Interfacial cracking .....	10
2.1.5 J-Integral .....	11
2.2 Fracture-based measurement techniques for thin – film adhesion.....	14
2.2.1 Blister test .....	14
2.2.2 Indentation tests .....	17
2.3 Effect of residual stress on coating delamination .....	20
2.4 Summary .....	21
2.5 Figures.....	22
2.6 References.....	27
Chapter 3 Experimental Procedure.....	32
3.1 Introduction.....	32
3.2 Specimen Preparation .....	32
3.3 Probe Test .....	33

3.3.1	Implementation using Optical Microscopy.....	34
3.3.2	Implementation using WYKO <sup>®</sup> Optical Profiler .....	37
3.4	Summary .....	40
3.5	Figures.....	41
3.6	References.....	51
Chapter 4	Analytical Methods.....	52
4.1	Introduction.....	52
4.2	Shaft – loaded blister approximation .....	52
4.2.1	Theory .....	53
4.2.2	Results and discussion .....	57
4.3	Curvature Method .....	61
4.3.1	Theory .....	61
4.3.2	Implementation .....	65
4.3.3	Results and discussion .....	67
4.4	Summary .....	68
4.5	Figures.....	70
4.6	References.....	90
Chapter 5	Numerical Methods.....	91
5.1	Introduction.....	91
5.2	Displacement field-based finite element model.....	91
5.2.1	Introduction.....	91
5.2.2	Implementation .....	92
5.2.3	Results and discussion .....	96
5.3	Contact interaction analysis .....	98
5.3.1	Introduction.....	98
5.3.2	An overview of contact interaction analysis in ABAQUS/Standard .....	98
5.3.3	Implementation .....	100
5.3.4	Effect of residual stress.....	102
5.3.5	Results and discussion .....	103
5.4	Summary .....	104
5.5	Tables.....	105

5.6	Figures.....	106
5.7	References.....	127
Chapter 6	Summary.....	128
6.1	Overview.....	128
6.2	Comparison with Xu’s work.....	128
6.3	Comparison with Mount’s work.....	129
6.4	Summary.....	130
6.4.1	Probe bending.....	132
6.5	Tables.....	133
6.6	Figures.....	134
6.7	References.....	149
Appendix A	.....	150
Appendix B	.....	154
Appendix C	.....	157
Appendix D	.....	163

## LIST OF FIGURES

Figure 2-1 Three modes of fracture .....	22
Figure 2-2 A schematic illustration of the stresses near the tip of a crack in an elastic material .....	22
Figure 2-3 A schematic of the local orthogonal Cartesian coordinate system at the points on the crack front used to define J-Integral in three-dimensions.....	23
Figure 2-4 A schematic of a pressurized circular blister configuration.....	24
Figure 2-5 A schematic of a shaft-loaded circular blister configuration .....	24
Figure 2-6 Mechanical response of a thin blistering plate. Delamination occurs at A and follows the path AB .....	25
Figure 2-7 A schematic illustration of indentation-induced delamination (a) No buckling during indentation (b) double-buckling during indentation (c) single-buckling after removing the indenter tip .....	25
Figure 2-8 Indentation induced delamination: (a) AFM deflection image (b) height image (c) cross sectional trace.....	26
Figure 3-1 A schematic illustration of the probe advancing beneath a coating that is debonding from the substrate.....	41
Figure 3-2 Chemical structure of the components of model epoxy adhesive.....	41
Figure 3-3 A schematic illustration of specimen fabrication for the probe test.....	42
Figure 3-4 A schematic diagram of the experimental probe test setup under the optical microscope .....	43
Figure 3-5 A typical debonding event in the coating for the coating (70 $\mu$ m)/Si substrate specimen using a probe angle of 25 $^{\circ}$ .....	44
Figure 3-6 Debond growth in the coating at different probe penetration distances ( $\delta$ ) for the coating (70 $\mu$ m)/Si substrate specimen using a probe angle of 25 $^{\circ}$ .....	45
Figure 3-7 Plots of debond area (A) and debond aspect ratio ( $\gamma$ ) as a function of probe penetration distance ( $\delta$ ) for the coating (70 $\mu$ m)/Si substrate specimen using a probe angle of 25 $^{\circ}$ .....	46

Figure 3-8 Plots of debond radius ( $a$ ) along the probe direction as a function of probe penetration distance ( $\delta$ ) for the coating ( $70\mu\text{m}$ )/Si substrate specimen using a probe angle of $25^\circ$ .....	47
Figure 3-9 A schematic of the experimental probe test setup under the WYKO <sup>®</sup> optical profiler.....	47
Figure 3-10 A schematic illustration of the working principle of the interferometric-based WYKO <sup>®</sup> optical profiler .....	48
Figure 3-11 Debond surface topography using WYKO <sup>®</sup> optical profiler for the coating ( $70\mu\text{m}$ )/Si substrate specimen using a probe angle of $25^\circ$ .....	49
Figure 3-12 A surface topography image obtained using the WYKO <sup>®</sup> profiler for a debond of larger size than the field of view of the objective lens; image quality is bad in regions of steep gradient and a cropped image of the debond is obtained .....	49
Figure 3-13 An illustration of the envelope for the debond surface topography data obtained near the crack front region .....	50
Figure 4-1 A typical debonding event in the coating for the epoxy coating ( $70\mu\text{m}$ )/Si substrate specimen and using a probe angle of $25^\circ$ (Scale: 20X).....	70
Figure 4-2 A schematic of a shaft-loaded circular blister configuration .....	71
Figure 4-3 A schematic of the probe test geometry parameters .....	71
Figure 4-4 Plots of debond radius ( $a$ ) along the probe direction as a function of probe penetration distance ( $\delta$ ) for the epoxy coating ( $70\mu\text{m}$ )/Si substrate specimen using a probe angle of $25^\circ$ .....	72
Figure 4-5 Plots of non-dimensionalized debond radius ( $a/h$ ) as a function of non-dimensionalized coating deflection ( $w_0/h$ ) for the epoxy coating ( $70\mu\text{m}$ )/Si substrate specimen and using a probe angle of $25^\circ$ ; $h$ is the coating thickness. ....	73
Figure 4-6 Plots of interfacial fracture energy ( $\mathcal{G}_c$ ) vs. probe penetration distance ( $\delta$ ) calculated using thin plate – small deflection theory. The debonds were created using the probe test technique in an epoxy coating( $70\mu\text{m}$ )/Si substrate specimen and using a probe angle of $25^\circ$ .....	74
Figure 4-7 Plots of interfacial fracture energy ( $\mathcal{G}_c$ ) vs. probe penetration distance ( $\delta$ ) calculated using thin plate – large deflection theory. The debonds were created using the	

probe test technique in an epoxy coating(70 μm)/Si substrate specimen and using a probe angle of 25° ..... 75

Figure 4-8 Plots of interfacial fracture energy ( $G_c$ ) vs. probe penetration distance ( $\delta$ ) calculated using thick plate – large deflection theory. The debonds were created using the probe test technique in an epoxy coating(70 μm)/Si substrate specimen and using a probe angle of 25° ..... 76

Figure 4-9 Comparison of interfacial fracture energy ( $G_c$ ) calculated using different plate theory formulations. The debonds were created using the probe test technique in an epoxy coating(70 μm)/Si substrate specimen and using a probe angle of 25° ..... 77

Figure 4-10 A schematic representation of the debonded layer of a thin adhesive coating on a substrate..... 78

Figure 4-11 An image of the debond surface topography obtained using WYKO<sup>®</sup> optical profiler for the adhesive coating (70μm)/Si substrate specimen and a probing angle of 25° ..... 79

Figure 4-12 A surface topography image obtained using the WYKO<sup>®</sup> profiler for a debond of larger size than the field of view of the objective lens; bad data points are present in regions of steep gradient and a cropped image of the debond is obtained. .... 80

Figure 4-13 An illustration of the displacement profile along a radial direction of the crack front in a typical debond; 50 % of the debond area away from the crack front region is cropped (the un-cropped region is shown as shaded region). ..... 81

Figure 4-14 A comparative illustration of the experimental crack front image and the applied analytical polynomial fit, for a debond created using the probe test technique in an epoxy coating(70 μm)/Si substrate specimen and using a probe angle of 25° ..... 82

Figure 4-15 A typical  $z$  vs  $\tilde{r}$  displacement profile for a debond created using the probe test technique in an adhesive coating(70 μm)/Si substrate specimen and a probing angle of 25° ..... 83

Figure 4-16 Plots of interfacial fracture energy,  $G_c$  along the crack front ( $-45^\circ \leq \theta \leq 45^\circ$ ) of debond # 1 calculated using curvature method. The debond was created using the probe test technique in an epoxy coating(70 μm)/Si substrate specimen and using a probe angle of 25° ..... 84

Figure 4-17 Plots of interfacial fracture energy,  $\mathcal{G}_c$  along the crack front ( $-45^\circ \leq \theta \leq 45^\circ$ ) of debond # 2 calculated using curvature method. The debond was created using the probe test technique in an epoxy coating(70  $\mu\text{m}$ )/Si substrate specimen and using a probe angle of  $25^\circ$ ..... 85

Figure 4-18 Plots of interfacial fracture energy,  $\mathcal{G}_c$  along the crack front ( $-45^\circ \leq \theta \leq 45^\circ$ ) of debond # 3 calculated using curvature method. The debond was created using the probe test technique in an epoxy coating(70  $\mu\text{m}$ )/Si substrate specimen and using a probe angle of  $25^\circ$ ..... 86

Figure 4-19 Plots of interfacial fracture energy,  $\mathcal{G}_c$  along the crack front ( $-45^\circ \leq \theta \leq 45^\circ$ ) of debond # 4 calculated using curvature method. The debond was created using the probe test technique in an epoxy coating(70  $\mu\text{m}$ )/Si substrate specimen and using a probe angle of  $25^\circ$ ..... 87

Figure 4-20 Plots of interfacial fracture energy,  $\mathcal{G}_c$  along the crack front ( $-45^\circ \leq \theta \leq 45^\circ$ ) of debond # 5 calculated using curvature method. The debond was created using the probe test technique in an epoxy coating(70  $\mu\text{m}$ )/Si substrate specimen and using a probe angle of  $25^\circ$ ..... 88

Figure 4-21 Plots of interfacial fracture energy,  $\mathcal{G}_c$  averaged near the center of the crack front ( $-5^\circ \leq \theta \leq 5^\circ$ ) vs. probe penetration distance ( $\delta$ ) calculated using curvature method. The debonds were created using the probe test technique in an epoxy coating(70  $\mu\text{m}$ )/Si substrate specimen and using a probe angle of  $25^\circ$ ..... 89

Figure 5-1 A surface topography image obtained using the WYKO<sup>®</sup> profiler for a debond of larger size than the field of view of the objective lens; bad data points are present in regions of steep gradient and a cropped image of the debond is obtained. .... 106

Figure 5-2 A schematic illustration of a typical crack front profile ..... 107

Figure 5-3 A comparative illustration of the experimental crack front image and the applied analytical polynomial fit, for a debond created using the probe test technique in an epoxy coating(70  $\mu\text{m}$ )/Si substrate specimen and using a probe angle of  $25^\circ$  ..... 108

Figure 5-4 An illustration of the second – order, iso - parametric three – dimensional continuum elements available in ABAQUS ..... 109

Figure 5-5 An illustration of the radial-type finite element mesh for the coating used in the displacement-field based FEA model ..... 109

Figure 5-6 A schematic illustration of the concentrated node spacing towards the crack front, also note the quarter-point spacing at the crack front ..... 110

Figure 5-7 A contour plot of the displacement magnitude ( $u$ ) of the debonded coating obtained using displacement-field based finite element simulation. The thickness of the coating is  $70\ \mu\text{m}$  and the probe angle is  $25^\circ$ ..... 111

Figure 5-8 Plots of interfacial fracture energy,  $\mathcal{G}_c$  along the crack front ( $-45^\circ \leq \theta \leq 45^\circ$ ) of Debond # 1 obtained from displacement-field based FEA model. The debond was created using the probe test technique in an epoxy coating( $70\ \mu\text{m}$ )/Si substrate specimen and a probe angle of  $25^\circ$ . ..... 112

Figure 5-9 Plots of interfacial fracture energy,  $\mathcal{G}_c$  along the crack front ( $-45^\circ \leq \theta \leq 45^\circ$ ) of Debond # 2 obtained from displacement-field based FEA model. The debond was created using the probe test technique in an epoxy coating( $70\ \mu\text{m}$ )/Si substrate specimen and a probe angle of  $25^\circ$ . ..... 113

Figure 5-10 Plots of interfacial fracture energy,  $\mathcal{G}_c$  along the crack front ( $-45^\circ \leq \theta \leq 45^\circ$ ) of Debond # 3 obtained from displacement-field based FEA model. The debond was created using the probe test technique in an epoxy coating( $70\ \mu\text{m}$ )/Si substrate specimen and a probe angle of  $25^\circ$  ..... 114

Figure 5-11 Plots of interfacial fracture energy,  $\mathcal{G}_c$  along the crack front ( $-45^\circ \leq \theta \leq 45^\circ$ ) of Debond # 4 obtained from displacement-field based FEA model. The debond was created using the probe test technique in an epoxy coating( $70\ \mu\text{m}$ )/Si substrate specimen and a probe angle of  $25^\circ$  ..... 115

Figure 5-12 Plots of interfacial fracture energy,  $\mathcal{G}_c$  along the crack front ( $-45^\circ \leq \theta \leq 45^\circ$ ) for Debond #1 -  $\delta = 200$  micron, obtained using displacement-field based FEA model, showing the effect of mesh refinement on  $\mathcal{G}_c$  values. The debond was created using the probe test technique in an epoxy coating( $70\ \mu\text{m}$ )/Si substrate specimen and a probe angle of  $25^\circ$ ..... 116

Figure 5-13 Plots of interfacial fracture energy,  $G_c$  along the crack front ( $-45^\circ \leq \theta \leq 45^\circ$ ) for Debond #1 -  $\delta = 250$  micron, obtained using displacement-field based FEA model, showing the effect of mesh refinement on  $G_c$  values. The debond was created using the probe test technique in an epoxy coating(70  $\mu\text{m}$ )/Si substrate specimen and a probe angle of  $25^\circ$  ..... 117

Figure 5-14 Plots of interfacial fracture energy,  $G_c$  averaged near the center of the crack front ( $-5^\circ \leq \theta \leq 5^\circ$ ) vs. probe penetration distance ( $\delta$ ) obtained using displacement-field based FEA model. The debonds were created using the probe test technique in an epoxy coating(70  $\mu\text{m}$ )/Si substrate specimen and using a probe angle of  $25^\circ$  ..... 118

Figure 5-15 A typical debonding event in the coating for the coating (70 $\mu\text{m}$ )/Si substrate specimen using a probe angle of  $25^\circ$  ..... 119

Figure 5-16 Plot of average debond radius (a) along the probe direction over 5 different debonds as a function of probe penetration distance ( $\delta$ ) for the coating (70 $\mu\text{m}$ )/Si substrate specimen and using a probe angle of  $25^\circ$  ..... 120

Figure 5-17 A schematic of the geometric profile of the probe..... 120

Figure 5-18 Equivalent nodal loads produced by a constant pressure on the second-order element face in contact simulations ..... 121

Figure 5-19 A schematic of the finite element mesh used for contact interaction simulation..... 121

Figure 5-20 A contour plot of the out-of-plane displacement ( $u_2$ ) of the debonded coating obtained using finite element contact interaction simulation. The thickness of the coating is 70  $\mu\text{m}$  and the probe angle is  $25^\circ$ ..... 122

Figure 5-21 Plots of interfacial fracture energy,  $G_c$  along the crack front ( $-90^\circ \leq \theta \leq 90^\circ$ ) calculated using finite element contact interaction method. The debond was created using the probe test technique in an epoxy coating(70  $\mu\text{m}$ )/Si substrate specimen and a probe angle of  $25^\circ$ ..... 123

Figure 5-22 Plot of interfacial fracture energy,  $G_c$  averaged near the center of the crack front ( $-5^\circ \leq \theta \leq 5^\circ$ ) vs. probe penetration distance ( $\delta$ ), calculated using finite element

contact interaction method. The debonds were created using the probe test technique in an epoxy coating (70 μm)/Si substrate specimen and a probe angle of 25° ..... 124

Figure 5-23 Plots of interfacial fracture energy,  $G_c$  along the crack front ( $-90^\circ \leq \theta \leq 90^\circ$ ) for  $\delta = 200$  micron calculated with and without the presence of residual stress in the finite element contact interaction model. The debond was created using the probe test technique in an epoxy coating(70 μm)/Si substrate specimen and a probe angle of 25° ..... 125

Figure 5-24 Plots of interfacial fracture energy,  $G_c$  along the crack front ( $-90^\circ \leq \theta \leq 90^\circ$ ) for  $\delta = 250$  micron calculated with and without the presence of residual stress in the finite element contact interaction model. The debond was created using the probe test technique in an epoxy coating(70 μm)/Si substrate specimen and a probe angle of 25° ..... 126

Figure 6-1 Debond radii along (x-axis) and perpendicular (y-axis) to probe direction versus probe penetration distance measured for a debond in model epoxy/Si bonded specimen under dry conditions. Coating thickness is 75 μm..... 134

Figure 6-2 Plots of debond radius (a) along the probe direction (x-axis) as a function of probe penetration distance ( $\delta$ ) for the coating (70μm)/Si substrate specimen and using a probe angle of 25° ..... 135

Figure 6-3 Debond radii along (x-axis) and perpendicular (y-axis) to probe direction versus  $w_0$ , the debond height at the free edge of the coating measured for a debond in model epoxy/ Si bonded specimen under dry conditions. Coating thickness is 75μm... 136

Figure 6-4 Plots of debond radius (a) as a function of coating deflection ( $w_0$ ) for the epoxy coating (70μm)/Si substrate specimen and using a probe angle of 25°; h is the coating thickness..... 137

Figure 6-5 Debond area as a function of probe penetration distance for a model epoxy coated as-received Si front side and back side specimens tested under dry conditions . 138

Figure 6-6 Plots of debond area (A) and debond aspect ratio ( $\gamma$ ) as a function of probe penetration distance ( $\delta$ ) for the coating (70μm)/Si substrate specimen using a probe angle of 25° ..... 139

Figure 6-7 Interfacial fracture energy ( $G_c$ ) versus probe penetration distance for a debond in the model epoxy/ Si specimen under dry conditions. Coating thickness is 80 μm .... 140

Figure 6-8 Plot of interfacial fracture energy ( $\mathcal{G}_c$ ) vs. probe penetration distance ( $\delta$ ) calculated using thin plate – small deflection theory. The  $\mathcal{G}_c$  values shown were averaged over five different debonds which were created using the probe test technique in an epoxy coating(70  $\mu\text{m}$ )/Si substrate specimen and using a probe angle of 25°. ..... 141

Figure 6-9 Graphical representation of von Mises stresses of an edge-loaded thin film 142

Figure 6-10 Plot of log of  $\mathcal{G}_{tot}$  along the crack front with varying debond radius and no residual stress ..... 143

Figure 6-11 Plot of log of  $\mathcal{G}_{tot}$  along the crack front with varying debond radius and residual stress ..... 144

Figure 6-12 Plots of interfacial fracture energy,  $\mathcal{G}_c$  along the crack front ( $-90^\circ \leq \theta \leq 90^\circ$ ) calculated using finite element contact interaction method. The debond was created using the probe test technique in an epoxy coating(70  $\mu\text{m}$ )/Si substrate specimen and a probe angle of 25° ..... 145

Figure 6-13 Plots of interfacial fracture energy,  $\mathcal{G}_c$  along the crack front ( $-90^\circ \leq \theta \leq 90^\circ$ ) for  $\delta = 200$  micron calculated with and without the presence of residual stress in the finite element contact interaction model. The debond was created using the probe test technique in an epoxy coating(70  $\mu\text{m}$ )/Si substrate specimen and a probe angle of 25° ..... 146

Figure 6-14 Comparison of interfacial fracture energy ( $\mathcal{G}_c$ ) calculated using different analytical and FEA based techniques in the present research. The debonds were created using the probe test technique in an epoxy coating(70  $\mu\text{m}$ )/Si substrate specimen and using a probe angle of 25° ..... 147

Figure 6-15 A schematic illustration of the loading and boundary conditions on the probe in contact with the coating and the substrate in the probe test experiment..... 148

## **LIST OF TABLES**

Table 5-1 Material properties of the coating.....	105
Table 6-1 A matrix summarizing the different experimental data used with the corresponding analytical/numerical techniques for analyzing the probe test geometry .	133

# Chapter 1 Introduction

## 1.1 Overview

Coating and thin film adhesion is a very important property not only for microelectronics and magnetic recording industries, but also for emerging technologies such as data transmission through optical switches that are dependent on micro-electromechanical systems (MEMS) [1]. In general, coatings find use in a wide variety of industries, normally to serve one or more of the following purposes [2]:

- i. to protect the surface from corrosion;
- ii. to control friction and wear;
- iii. to alter physical properties, such as reflectivity, color, conductivity, etc

Coatings can fail in several modes including delamination, fracture, erosive wear, and general yield. The weakest part in coating systems is commonly the interface; thus, for many material systems, interfacial delamination becomes the dominant failure mechanism [3], especially with long term exposure to challenging environments. Delamination of a coating refers to the loss of adhesion of the coating from the substrate, and, if the coating stresses are compressive, may result in buckling driven delamination. Residual stresses, thermal mismatch stresses, environmental attack, and impact or contact stresses are some of the causes of delamination. Another important delamination – induced failure mechanism seen in metallic or ceramic coating systems, for example, thermal barrier coating systems, is due to thermal gradient and thermal mechanical fatigue [4, 5] .

Qualitative tests such as the tape test or the pull-off test [6-8] are often used to monitor coating adhesion, since they are quick and easy to perform. While for some applications this qualitative comparison is sufficient, quantitative adhesion values are often desired for understanding factors contributing to coating adhesion, for numerical simulations and life-time predictions.

Most adhesion tests empirically infer the adhesive strength by subjecting the specimen to some external load and measuring the critical value at which the test

specimen fails [9]. The results of these tests are reported as the force at failure divided by the bonded area. However, in practical joints, the maximum stress will be significantly higher than this average value. The failure initiation in the joint is most likely to be related to the maximum stress rather than the average stress value measured and reported.

An alternate approach using linear elastic fracture mechanics (LEFM) views the adhesive coating as a system in which failure (typically the growth of a crack) requires that the stresses at the crack tip be sufficient to break bonds. The analysis in this approach involves using an energy balance, and the hypothesis used is that even if the stresses are very large, a crack can grow only if sufficient energy is released from the stress field to account for energy required to create the new crack surface as the fractured region enlarges. The critical value of this energy release rate associated with delamination of adhesive coatings is known as interfacial fracture energy ( $G_c$ ).

There are a number of different techniques for measuring coating adhesion based on the LEFM approach. However, there are no universal tests for measuring coating adhesion. This can be explained by the variety of coating systems even a single industry (e.g. microelectronics) may deal with. These represent different types of dissimilar material interfaces that are present in modern electronic devices (metal/metal, metal/ceramic, polymer/metal, polymer/ceramic, etc). Some of the other variations among these coating systems are the degree of adhesion of the coatings, coating thickness and visco-elastic properties of the coating. As a result, a test that works with one coating system may not necessarily work with another. Hence, a versatile and effective test procedure is desired for the purpose of evaluating the adhesion of thin film microelectronics coatings. The ability to perform the test on a range of specimen geometries is preferred so that the technique can be applied to as-produced components. Also, the specimens should be simple to fabricate with minimal specimen preparation and without any need for auxiliary adhesives, backings, over-layers etc.

## 1.2 Research Objective

In the present work, a test technique, referred to as the *probe test*, has been developed as a quantitative tool for measuring the adhesion in thin adhesive films and coatings. The technique was initially developed as a qualitative test by the Hewlett-

Packard Company for measuring adhesion of thin film microelectronic coatings. In this study, a standard test procedure has been developed for testing a thin adhesive coating/substrate system. The sample system used is a thin film epoxy polymer coated silicon system. The interfacial fracture energy ( $G_c$ ) (or critical strain energy release rate) was used as a quantitative measure of the adhesion in a given coating system. Hence using experimental data from the probe test, analytical and numerical techniques have been developed to determine the interfacial fracture energy ( $G_c$ ) for the given adhesive coating/substrate system.

### **1.3 Outline**

This thesis is divided into six chapters and each chapter is briefly described as follows:

Chapter 1 gives a brief description of background information related to this research and presents the objectives of this study along with the organization of this thesis.

Chapter 2 provides a literature review of fracture mechanics fundamentals and the existing fracture-based test techniques for measuring adhesion of thin films and coatings.

Chapter 3 describes the experimental procedure of the probe test method for measuring the adhesion in thin adhesive films and coatings.

Chapter 4 describes the analytical techniques which have been developed to provide a quantitative measure of the adhesion in a given adhesive coating/substrate system, using the probe test technique.

Chapter 5 presents the finite element techniques which have been used to model the geometry of the adhesive coating in the probe test method.

Chapter 6 summarizes the current research and provides a comparison with previous research done in this area.

## 1.4 References

1. Volinsky, A.A., N.R. Moody, and W.W. Gerberich, *Interfacial toughness measurements for thin films on substrates*. Acta Materialia, 2002. **50**(3): p. 441-466.
2. Dillard, D.A. and A.V. Pocius, *The mechanics of adhesion*. Adhesion science and engineering, ed. A.V. Pocius. Vol. 1. 2002, Amsterdam ; Boston: Elsevier.
3. Wiklund, U., J. Gunnars, and S. Hogmark, *Influence of residual stresses on fracture and delamination of thin hard coatings*. Wear, 1999. **232**(2): p. 262-269.
4. Qian, G., T. Nakamura, and C.C. Berndt, *Effects of thermal gradient and residual stresses on thermal barrier coating fracture*. Mechanics of Materials, 1998. **27**(2): p. 91-110.
5. Zhou, Y.C. and T. Hashida, *Delamination cracking in thermal barrier coating system*. Journal of Engineering for Gas Turbines and Power-Transactions of the Asme, 2002. **124**(4): p. 922-930.
6. Jacobsson, R., *Measurement of Adhesion of Thin-Films*. Thin Solid Films, 1976. **34**(2): p. 191-199.
7. Ohring, M., *The materials science of thin films*. 1992, Boston: Academic Press.
8. Steinmann, P.A. and H.E. Hintermann, *A Review of the Mechanical Tests for Assessment of Thin-Film Adhesion*. Journal of Vacuum Science & Technology a-Vacuum Surfaces and Films, 1989. **7**(3): p. 2267-2272.
9. Pocius, A.V., *Adhesion and adhesives technology : an introduction*. 1997, Munich; New York; Cincinnati: Hanser Publishers; Hanser/Gardner Publications.

## Chapter 2 Literature Review

### 2.1 Fracture Mechanics

#### 2.1.1 Introduction

The field of fracture mechanics attempts to quantify the relationship between failure stress, flaw size, and material properties. According to the traditional strength of materials approach to structural design, a material is assumed to be adequate if its strength is greater than the expected applied stress. Such an approach attempts to guard against brittle fracture by imposing a safety factor on the strength of the material to get the maximum allowable design stress. The fracture mechanics approach instead uses a critical combination of three variables: applied stress, flaw size and fracture toughness. This approach makes it possible to determine whether a crack of given length in a material of known fracture toughness is dangerous because it will propagate to fracture at a given stress level. It also permits the selection of materials for resistance to fracture and a design selection which is most resistant to fracture. Most fracture mechanics methodologies assume linear elastic behavior, although more advanced approaches incorporate nonlinear material behavior such as yielding. There are two alternative approaches to linear elastic fracture analysis (LEFM): the stress intensity approach and the energy release rate approach.

#### 2.1.2 Stress intensity approach

The stress intensity factor approach, based on the work by Irwin [1], develops the concept that the fracture toughness should be measured in terms of resistance to crack propagation. According to this approach, fracture occurs when the applied stress intensity factor,  $K$ , exceeds a critical value,  $K_c$ , which is a material property.

In general, there are three modes of deformation that could be applied to the crack, as shown in Figure 2-1. Mode I, the crack – opening mode, refers to a tensile stress applied normal to the faces of the crack. Mode II, the sliding mode or forward shear mode, refers to a shear stress applied normal to the leading edge of the crack but in the

plane of the crack. Mode III, the anti-plane shear or tearing mode, is for shearing stress applied parallel to the leading edge of the crack.

For two-dimensional linear elasticity, Williams derived the form of the displacement and stress fields in the vicinity of a corner [2] and, subsequently, the limiting case of a crack tip [3]. Based on this work, the following analysis on the stress distribution in the region surrounding a crack tip in a linearly elastic homogenous material is presented.

In the region surrounding a crack tip (Figure 2-2) in an infinite elastic medium, the equilibrium equations can be expressed as:

$$\nabla^4 \phi = 0 \quad (2.1)$$

where  $\phi$  is the Airy stress function, which satisfies the compatibility conditions and is given as:

$$\begin{aligned} \sigma_{rr} &= \frac{1}{r} \frac{\partial \phi}{\partial r} + \frac{1}{r^2} \frac{\partial^2 \phi}{\partial \theta^2} \\ \sigma_{\theta\theta} &= \frac{\partial^2 \phi}{\partial r^2} \\ \sigma_{r\theta} &= -\frac{\partial}{\partial r} \left( \frac{1}{r} \frac{\partial \phi}{\partial \theta} \right) \end{aligned} \quad (2.2)$$

The stress components ( $\sigma_{rr}, \sigma_{\theta\theta}, \sigma_{r\theta}$ ) in Equation (2.2) are illustrated in Figure 2-2. Using the method of separation of variables, the stress function can be expressed as:

$$\phi(r, \theta) = r^{\lambda+1} f(\theta) \quad (2.3)$$

Thus, using Equation (2.3), Equation (2.1) can be re-written as:

$$\nabla^4 \phi = f'''' + 2(\lambda^2 + 1)f'' + (\lambda^2 - 1)^2 f = 0 \quad (2.4)$$

Assuming the following solution functional form:

$$f(\theta) = Ae^{\beta\theta} \quad (2.5)$$

the characteristic Equation (2.4) can be solved using Equations (2.1), (2.2) and (2.5). The stress function and stress components are thus obtained as:

$$\phi(r, \theta) = r^{\lambda+1} [C_1 \cos(\lambda-1)\theta + C_2 \sin(\lambda-1)\theta + C_3 \cos(\lambda+1)\theta + C_4 \sin(\lambda+1)\theta]$$

$$\begin{aligned} \sigma_{rr} = & -\lambda r^{\lambda-1} [(\lambda-3) \{C_1 \cos(\lambda-1)\theta + C_2 \sin(\lambda-1)\theta\} + \\ & (\lambda+1) \{C_3 \cos(\lambda+1)\theta + C_4 \sin(\lambda+1)\theta\}] \end{aligned} \quad (2.6)$$

$$\sigma_{\theta\theta} = \lambda(\lambda+1)r^{\lambda-1} [C_1 \cos(\lambda-1)\theta + C_2 \sin(\lambda-1)\theta + C_3 \cos(\lambda+1)\theta + C_4 \sin(\lambda+1)\theta]$$

$$\begin{aligned} \sigma_{r\theta} = & -\lambda r^{\lambda-1} [(\lambda-1) \{-C_1 \sin(\lambda-1)\theta + C_2 \cos(\lambda-1)\theta\} + \\ & (\lambda+1) \{-C_3 \sin(\lambda+1)\theta + C_4 \cos(\lambda+1)\theta\}] \end{aligned}$$

The boundary conditions for the free – free edges (Figure 2-2) can be expressed as:

$$\begin{aligned} \text{At } \theta = \alpha: & \quad \sigma_{\theta\theta}(r, \alpha) = 0 & \quad \sigma_{r\theta}(r, \alpha) = 0 \\ \text{At } \theta = -\alpha: & \quad \sigma_{\theta\theta}(r, -\alpha) = 0 & \quad \sigma_{r\theta}(r, -\alpha) = 0 \end{aligned} \quad (2.7)$$

Applying the boundary conditions to Equation (2.6), the equations decouple into two sets for Mode I and Mode II fracture:

$$\begin{bmatrix} \cos(\lambda-1)\alpha & \cos(\lambda+1)\alpha \\ (\lambda-1)\sin(\lambda-1)\alpha & (\lambda+1)\sin(\lambda+1)\alpha \end{bmatrix} \begin{pmatrix} C_1 \\ C_3 \end{pmatrix} = \begin{pmatrix} 0 \\ 0 \end{pmatrix} \Rightarrow \text{Mode I} \quad (2.8)$$

$$\begin{bmatrix} \sin(\lambda-1)\alpha & \sin(\lambda+1)\alpha \\ (\lambda-1)\cos(\lambda-1)\alpha & (\lambda+1)\cos(\lambda+1)\alpha \end{bmatrix} \begin{pmatrix} C_2 \\ C_4 \end{pmatrix} = \begin{pmatrix} 0 \\ 0 \end{pmatrix} \Rightarrow \text{Mode II}$$

For a sharp crack,  $\alpha \rightarrow \pi$ , the elastic stress field in the vicinity of the crack tip is thus obtained as:

$$\begin{aligned} \sigma_{rr}(r, \theta) = & \frac{1}{4\sqrt{r}} \left\{ C_{11} \left[ \left( 5 \cos \frac{\theta}{2} - \cos \frac{3}{2} \theta \right) \right] + C_{21} \left[ -5 \sin \frac{\theta}{2} + 3 \sin \frac{3}{2} \theta \right] \right\} + O(r^{1/2}) \\ \sigma_{\theta\theta}(r, \theta) = & \frac{1}{4\sqrt{r}} \left\{ C_{11} \left[ \left( 3 \cos \frac{\theta}{2} + \cos \frac{3}{2} \theta \right) \right] + C_{21} \left[ -3 \sin \frac{\theta}{2} - 3 \sin \frac{3}{2} \theta \right] \right\} + O(r^{1/2}) \\ \sigma_{r\theta}(r, \theta) = & \frac{1}{4\sqrt{r}} \left\{ C_{11} \left[ \left( \sin \frac{\theta}{2} + \sin \frac{3}{2} \theta \right) \right] + C_{21} \left[ \cos \frac{\theta}{2} + 3 \cos \frac{3}{2} \theta \right] \right\} + O(r^{1/2}) \end{aligned} \quad (2.9)$$

The stress function in Equation (2.9) contains symmetric and anti-symmetric components, with respect to  $\theta = 0$ . Thus,  $C_{22} = 0$  implies the case of symmetric loading (Mode I) and  $C_{11} = 0$  implies pure anti-symmetric loading (Mode II).

Finally, the stress and displacement field solutions in the vicinity of the crack tip for pure mode I and mode II fracture are given by Equations (2.10) and (2.11) respectively.

For pure mode I (opening mode):

$$\begin{aligned}
\sigma_{rr}(r, \theta) &= \frac{1}{4} \frac{K_I}{\sqrt{2\pi r}} \left( 5 \cos \frac{\theta}{2} - \cos \frac{3}{2} \theta \right) \\
\sigma_{\theta\theta}(r, \theta) &= \frac{1}{4} \frac{K_I}{\sqrt{2\pi r}} \left( 3 \cos \frac{\theta}{2} + \cos \frac{3}{2} \theta \right) \\
\sigma_{r\theta}(r, \theta) &= \frac{1}{4} \frac{K_I}{\sqrt{2\pi r}} \left( \sin \frac{\theta}{2} + \sin \frac{3}{2} \theta \right) \\
u_r(r, \theta) &= \frac{1}{4} \frac{K_I}{\mu} \sqrt{\frac{r}{2\pi}} \left( (2\kappa - 1) \cos \frac{\theta}{2} - \cos \frac{3}{2} \theta \right) \\
u_\theta(r, \theta) &= \frac{1}{4} \frac{K_I}{\mu} \sqrt{\frac{r}{2\pi}} \left( -(2\kappa + 1) \sin \frac{\theta}{2} + \sin \frac{3}{2} \theta \right)
\end{aligned} \tag{2.10}$$

For pure mode II (sliding mode):

$$\begin{aligned}
\sigma_{rr}(r, \theta) &= \frac{1}{4} \frac{K_{II}}{\sqrt{2\pi r}} \left( -5 \sin \frac{\theta}{2} + 3 \sin \frac{3}{2} \theta \right) \\
\sigma_{\theta\theta}(r, \theta) &= \frac{1}{4} \frac{K_{II}}{\sqrt{2\pi r}} \left( -3 \sin \frac{\theta}{2} - 3 \sin \frac{3}{2} \theta \right) \\
\sigma_{r\theta}(r, \theta) &= \frac{1}{4} \frac{K_{II}}{\sqrt{2\pi r}} \left( \cos \frac{\theta}{2} + 3 \cos \frac{3}{2} \theta \right) \\
u_r(r, \theta) &= \frac{1}{4} \frac{K_{II}}{\mu} \sqrt{\frac{r}{2\pi}} \left( -(2\kappa - 1) \sin \frac{\theta}{2} + 3 \sin \frac{3}{2} \theta \right) \\
u_\theta(r, \theta) &= \frac{1}{4} \frac{K_{II}}{\mu} \sqrt{\frac{r}{2\pi}} \left( -(2\kappa + 1) \cos \frac{\theta}{2} + 3 \cos \frac{3}{2} \theta \right)
\end{aligned} \tag{2.11}$$

where  $\mu$  is the shear modulus of the material, and  $\kappa$  is defined as a function of the Poisson's ratio  $\nu$  of the material as :

$$\begin{aligned}
k &= \frac{3-\nu}{1+\nu} \quad \text{for plane stress } (\sigma_{zz} = \sigma_{rz} = \sigma_{\theta z} = 0) \\
k &= 3-4\nu \quad \text{for plane strain } (\sigma_{zz} = \nu(\sigma_{rr} + \sigma_{\theta\theta}))
\end{aligned} \tag{2.12}$$

In Equations (2.10) and (2.11), the mode I and mode II stress intensity factors  $K_I$  and  $K_{II}$  are defined as:

$$K_I = \lim_{r \rightarrow 0} \sigma_{\theta\theta}(r, 0) \sqrt{2\pi r} \quad (2.13)$$

$$K_{II} = \lim_{r \rightarrow 0} \sigma_{r\theta}(r, 0) \sqrt{2\pi r}$$

The above analysis can be extended to pure mode III fracture to obtain the solutions for the out-of-plane shear stresses ( $\sigma_{rz}, \sigma_{\theta z}$ ) and out-of-plane displacement ( $u_z$ ) in the vicinity of the crack tip, given as [4]:

$$\begin{aligned} \sigma_{rz}(r, \theta) &= -\frac{K_{III}}{\sqrt{2\pi r}} \sin \frac{\theta}{2} \\ \sigma_{\theta z}(r, \theta) &= \frac{K_{III}}{\sqrt{2\pi r}} \cos \frac{\theta}{2} \\ u_z(r, \theta) &= \frac{2K_{III}}{\mu} \sqrt{\frac{r}{2\pi}} \sin \frac{\theta}{2} \end{aligned} \quad (2.14)$$

where the mode III stress intensity factor  $K_{III}$  is defined as:

$$K_{III} = \lim_{r \rightarrow 0} \sigma_{\theta z}(r, 0) \sqrt{2\pi r} \quad (2.15)$$

### 2.1.3 Energy release rate approach

The energy release rate approach states that crack extension (i.e., fracture) occurs when the energy available for crack growth is sufficient to overcome the resistance of the material. The material resistance may include the surface energy, plastic work, or other types of energy dissipation associated with a propagating crack.

Griffith [5] was the first to propose the energy criterion for fracture, but Irwin [6] is primarily responsible for developing the present version of this approach. According to this energy balance approach, during a quasi-static increment of crack area,  $dA$ , there can be no change in the total energy ( $E$ ) of the cracked body. The total energy ( $E$ ) is composed of the potential energy of deformation ( $U$ ) and the surface energy ( $S$ ). Therefore, during crack extension:

$$dE = dU + dS = 0 \quad (2.16)$$

For a linear elastic material, the rate of change of potential energy with respect to crack area,  $dA$  is defined as the energy release rate  $G$ .

$$\mathcal{G} = -\frac{dU}{dA} \quad (2.17)$$

At the moment of fracture:

$$\mathcal{G} = \mathcal{G}_c \quad (2.18)$$

where  $\mathcal{G}_c$  is defined as the critical energy release rate or fracture energy and is a measure of the fracture resistance of the material.

For a linear elastic material, the energy release rate  $\mathcal{G}$  can be related to the stress intensity factors ( $K_I, K_{II}, K_{III}$ ) by the following relationship [4]:

$$\mathcal{G} = \frac{1}{\bar{E}}(K_I^2 + K_{II}^2) + \frac{1}{2\mu} K_{III}^2 \quad (2.19)$$

where  $\bar{E} = E$  for plane stress and  $\bar{E} = E/(1-\nu^2)$  for plane strain.

#### 2.1.4 Interfacial cracking

A crack in an interface with a fracture toughness that is distinct from the materials joined across it can experience either kinking or straight-ahead propagation under mixed-mode loading depending on a number of factors, including the relative toughness of the interface to that of the adjoining materials. Solutions to bimaterial interface crack problem has been presented by Rice et al [7, 8]. The dominant stresses near the tip of an interface crack between material 1 and material 2 are given as [8]:

$$\sigma_{\alpha\beta} = \frac{\text{Re}[Kr^{i\varepsilon}]}{\sqrt{2\pi r}} \sigma_{\alpha\beta}^I(\theta, \varepsilon) + \frac{\text{Im}[Kr^{i\varepsilon}]}{\sqrt{2\pi r}} \sigma_{\alpha\beta}^{II}(\theta, \varepsilon) \quad (2.20)$$

where  $\varepsilon$  is the bimaterial constant defined as:

$$\varepsilon = \frac{1}{2\pi} \ln \left( \frac{1-\beta}{1+\beta} \right) \quad (2.21)$$

and  $\beta$  is one of the Dundurs [9] parameter for elastic bimaterials, defined as:

$$\beta = \frac{\mu_1(\kappa_2 - 1) - \mu_2(\kappa_1 - 1)}{\mu_1(\kappa_2 + 1) + \mu_2(\kappa_1 + 1)} \quad (2.22)$$

In Equation (2.20), the complex stress intensity factor  $K = K_1 + iK_2$  has real and imaginary parts  $K_1$  and  $K_2$ , respectively which are similar to mode I and II stress

intensity factors for monolithic materials. The quantities  $\sigma_{\alpha\beta}^I(\theta, \varepsilon)$  and  $\sigma_{\alpha\beta}^{II}(\theta, \varepsilon)$  are given in polar coordinates by Rice et al [10]. The normalized stresses ahead of the crack tip are given as [11]:

$$\sigma_{yy} + i\sigma_{xy} = \frac{(K_1 + iK_2)}{\sqrt{2\pi r}} r^{i\varepsilon} \quad (2.23)$$

where  $r^{i\varepsilon} = \cos(\varepsilon \ln r) + i \sin(\varepsilon \ln r)$  is an oscillating singularity which results in an interpenetration of the crack faces. The associated crack frank displacements a distance  $r$  behind the tip,  $\delta_i = u_i(r, \theta = \pi) - u_i(r, \theta = -\pi)$ , are given as [12]:

$$\delta_1 + i\delta_2 = \frac{8}{(1 + 2i\varepsilon) \cosh(\pi\varepsilon)} \frac{K_1 + iK_2}{E^*} \left(\frac{r}{2\pi}\right)^{1/2} r^{i\varepsilon} \quad (2.24)$$

where

$$\frac{1}{E^*} = \frac{1}{2} \left( \frac{1}{\bar{E}_1} + \frac{1}{\bar{E}_2} \right) \quad (2.25)$$

and  $\bar{E}_i = E_i / (1 - \nu_i^2)$  for plane strain and  $\bar{E}_i = E_i$  plane stress

The energy release rate for crack advance along the interface is given as:

$$\mathcal{G} = \frac{(1 - \beta^2)}{E^*} (K_1^2 + K_2^2) \quad (2.26)$$

The present study focuses on the interfacial fracture in a thin adhesive coating/substrate system. However, the solution outlined in this section on bimaterial interfacial fracture has not been used in the present work. Instead, the present work uses an energy balance approach which is equivalent to the approach in this section.

### 2.1.5 J-Integral

The J-integral is widely accepted as a fracture mechanics parameter for both linear and nonlinear material response. It is related to the energy release associated with crack growth and is a measure of the intensity of deformation at a notch or crack tip, especially for nonlinear materials. In a linear elastic analysis, the J-integral is equivalent to the energy release rate,  $\mathcal{G}$  and it can also be related to the stress intensity factors. The J-integral, introduced by Rice [13], was originally a two-dimensional line integral.

Considering a path  $\Gamma$  which encloses the crack tip and with initial and final points which lie on the two crack faces, the J-integral is defined as [13]:

$$J = \int_{\Gamma} \left( W dy - \mathbf{T} \cdot \frac{\partial \mathbf{u}}{\partial x} ds \right) \quad (2.27)$$

where  $W$  is the strain energy density,  $\mathbf{T}$  is the traction vector defined according to the outward normal along  $\Gamma$ ,  $\mathbf{u}$  is the displacement vector and  $ds$  is an element of arc length along  $\Gamma$ . The integral is evaluated in a counterclockwise sense starting from the bottom crack surface and ending on the top surface.

The J-integral can be extended to three dimensions by considering a crack with a tangentially continuous front, as shown in Figure 2-3. The local direction of virtual crack extension is given by  $\mathbf{q}$ , which is the perpendicular to the local crack front and lies in the crack plane [14]. Asymptotically, as  $r \rightarrow 0$ , the conditions for path independence apply on any contour in the  $x_1$ - $x_2$  plane, which is perpendicular to the crack front at  $s$ . Hence, the J-integral defined in this plane can be used to represent the point-wise energy release rate along the crack front as

$$J(s) = \lim_{\Gamma \rightarrow 0} \int_{\Gamma} \mathbf{n} \cdot \mathbf{H} \cdot \mathbf{q} d\Gamma \quad (2.28)$$

where  $\Gamma$  is a contour beginning on the bottom crack surface and ending on the top surface; the limit  $\Gamma \rightarrow 0$  indicates that  $\Gamma$  shrinks onto the crack tip and  $\mathbf{n}$  is the outward normal to  $\Gamma$ .  $\mathbf{H}$  is defined as

$$\mathbf{H} = W\mathbf{I} - T \frac{\partial \mathbf{u}}{\partial \mathbf{x}} \quad (2.29)$$

For elastic material behavior  $W$  is the elastic strain energy; for elastic-plastic or elastic-viscoplastic material behavior  $W$  is defined as the elastic strain energy density plus the plastic dissipation, thus representing the strain energy in an “equivalent elastic material”.

For a virtual crack advance  $\lambda(s)$  in the plane of a three-dimensional crack, the energy release rate is given by

$$\bar{J} = \int_L J(s) \lambda(s) ds = \lim_{\Gamma \rightarrow 0} \int_{A_s} \lambda(s) \mathbf{n} \cdot \mathbf{H} \cdot \mathbf{q} dA \quad (2.30)$$

where  $L$  denotes the crack front under consideration;  $dA$  is a surface element on a vanishingly small tubular surface enclosing the crack tip (i.e.,  $dA = dsd\Gamma$ ); and  $\mathbf{n}$  is the outward normal to  $dA$ .

The stress intensity factor can be related to J-integral for a linear elastic material through [14]:

$$J = \frac{1}{8\pi} \mathbf{K}^T \cdot \mathbf{B}^{-1} \cdot \mathbf{K} \quad (2.31)$$

where  $\mathbf{K} = [K_I, K_{II}, K_{III}]^T$  and  $\mathbf{B}$  is called the pre-logarithmic energy factor matrix.

Using the divergence theorem, the J-integral can be extended to 3D by considering a tubular surface around the crack front. This domain integral method is used to evaluate contour integrals in the finite element code ABAQUS. Courtin et al [15] have compared the crack opening displacement extrapolation technique (see Equations (2.10) and (2.11)) which uses singular finite elements in the vicinity of the crack tip with the J-integral approach. The results were obtained using 2D and 3D ABAQUS finite element models on compact tension specimens and cracked round bars; the J-integral approach is shown to provide the same results with good agreement with the displacement extrapolation technique. The J-integral method is particularly attractive because it is simple to use, adds little to the cost of the analysis, and provides excellent accuracy, even with rather coarse meshes. The knowledge of the exact displacement field in the vicinity of the crack tip is not required and the use of singular finite elements is no longer essential. Also, theoretically, the J-integral quantity is path independent. As a result, the values can be obtained quite far away from the crack tip.

In ABAQUS/Standard, the \*CONTOUR INTEGRAL option offers the evaluation of the J-integral and the stress intensity factors for fracture mechanics studies. Several contour integral evaluations are possible at each location along a crack. In a finite element model each evaluation can be thought of as the virtual motion of a block of material surrounding the crack tip (in two dimensions) or surrounding each node along the crack line (in three dimensions). Each such block is defined by contours: each contour is a ring of elements completely surrounding the crack tip or the nodes along the crack line from one crack face to the opposite crack face. These rings of elements are defined recursively to surround all previous contours. ABAQUS/Standard automatically finds the

elements that form each ring from the regions given as the crack-tip or crack-line definition. Each contour provides an evaluation of the contour integral. The number of evaluations possible is the number of contours, which can be specified by using the CONTOURS parameter in the \*CONTOUR INTEGRAL option.

## 2.2 Fracture-based measurement techniques for thin – film adhesion

### 2.2.1 Blister test

The blister test has been used to measure the interfacial fracture energy for a debond at the interface of a thin film and a substrate [16, 17]. It consists of a thin layer of material adhering to or bonded to a rigid substrate except for a central unbonded portion where loading is applied. When the unbonded region is loaded, by applying a hydrostatic pressure ( $p$ ) (Figure 2-4) or a shaft load ( $F$ ) (Figure 2-5), the film lifts off the substrate and forms a blister whose radius stays fixed until a critical pressure is reached. At this value the radius of the blister increases in size due to adhesive failure along the interface [18]. The interfacial fracture energy can be deduced from an energy balance method that relates the applied critical load ( $p_c$  or  $F_c$ ), blister height ( $w_c$ ) and debond radius ( $a$ ). The standard circular blister test has been widely used to measure the adhesion of thin film structures typically used in the microelectronic packaging industry, e.g. diamond thin films [19] and polyimide films on silicon surfaces [20].

The blister test for an isotropic film and substrate has been analyzed by Jensen [21], for a circular debond zone. For small deflections of a thin plate, the fracture energy,  $G_c$ , for constant pressure loading is given as (Figure 2-4):

$$G_c = \frac{p_c w_c}{2}, \quad w_c = p_c \frac{3(1-\nu^2)a^4}{16Eh^3} \quad (2.32)$$

and for a shaft loaded blister as (Figure 2-5):

$$G_c = \frac{F_c w_c}{2\pi a^2}, \quad w_c = F_c \frac{3(1-\nu^2)a^2}{4\pi E h^3} \quad (2.33)$$

where  $E$  and  $\nu$  are the elastic modulus and Poisson ratio of the film and  $h$  is the thickness.

Hinkley [22] gave an approximate solution of the pressurized circular blister geometry without residual stress using membrane theory and assuming that the pressurized blister stretched to a spherical cap profile. The strain energy release rate for the pressurized blister was given as:

$$G_c = 0.25 p_c w_c, \quad p_c = \frac{8w_c^3 Eh}{3a^4(1-\nu)} \quad (2.34)$$

where  $w_c$  is the blister height at the critical pressure  $p_c$  for blister growth. The analysis used an incorrect energy balance formulation. Gent and Lewandowski [23] later gave a corrected version of the solution, assuming  $\nu = 0.5$ , as:

$$G_c = 0.65 p_c w_c; \quad p_c = \frac{4.75w_c^3 Eh}{a^4} \quad (2.35)$$

Briscoe and Panesar [24] used the pressurized circular blister test to study the adhesion of a polyurethane elastomeric adhesive to a steel substrate and showed that an analysis based exclusively upon the stored stretching energy better explained the observed blister deflection and fracture energy (obtained using peel tests for the same system) for the used system rather than one using stored bending energy. The analytical expression for fracture energy was given as:

$$G_c = \left[ \frac{p_c^4 a^4}{576 Eh(1-\nu^2)} \right]^{1/3} \quad (2.36)$$

O'Brien et al [25] have used a shaft loaded blister test to measure the applied strain energy rate rate ( $\mathcal{G}$ ) of pressure sensitive adhesive tape bonded to a rigid substrate. Arjun and Wan [26] gave an approximate analytical solution for a pressurized blister without residual stress from first principles for the standard pressurized blister test. The results show that  $\mathcal{G}$  depends on the loading history, with the transition from bending to stretching with increasing load. For a typical blister test mechanical response as shown in Figure 2-6, the strain energy release rate is given as:

$$\mathcal{G} = \lim_{\Delta A \rightarrow 0} \frac{1}{\Delta A} \int_0^V \Delta p dV = \int_0^V \frac{2\pi^2 D}{h^{n-1}} \left[ \frac{n+2}{A^{n+3}} \right] kV^n \times dV \quad (2.37)$$

where  $V$  is the blister volume,  $h$  is film thickness,  $D$  is the film flexural rigidity,  $k$  is a proportionality constant,  $A$  is the crack area,  $A = \pi a^2$ ; where  $a$  is the blister radius. Depending on the degree of deformation,  $n$  ranges from 1 to 3 as the dominant response goes from bending to stretching. Wan et al [27] obtained approximate analytical solutions for a clamped circular film in the presence of uniform residual tension. This analyses has been used in [28, 29] to derive the strain energy release rate for the circular blister in the presence of uniform tensile residual stress. The normalized strain energy release rate for a pressurized blister is given as:

$$\chi = \frac{\mathcal{G}}{pV/A} = \left( \frac{n}{n+1} \right) \left( \frac{a}{2V} \right) \frac{dV}{da} \quad (2.38)$$

and for a shaft loaded blister as:

$$\chi = \frac{\mathcal{G}}{Fw_0/A} = \left( \frac{n}{n+1} \right) \left( \frac{a}{2w_0} \right) \frac{dw_0}{da} \quad (2.39)$$

A major disadvantage of the standard pressurized circular blister test is that the strain energy release rate ( $\mathcal{G}$ ) increases as the blister radius ( $a$ ) increases, resulting in non-stable debonding under constant pressure loading [30]. Also, if the film is too thin or adheres too strongly, the blister may burst before debonding is initiated. To overcome this problem, alternative blister configurations have been proposed to measure the adhesion of thin films bonded on rigid substrates. Chang et al [31] proposed a constrained blister test that permits nearly constant strain energy release rate testing of adhesive bonds. This was achieved by placing a flat constrain above the blister to limit its deformation. Thus, the displaced blister volume becomes approximately proportional to the debond area and under constant pressure loading this resulted in a nearly constant strain energy release rate test. Neglecting the energy dissipation due to viscoelastic effects and frictional slipping, the critical strain energy release rate ( $\mathcal{G}_c$ ) was given as [32]:

$$\mathcal{G}_c = p_c w q \quad (2.40)$$

where  $p_c$  is the critical debonding pressure in the blister,  $w$  is the constrain height and  $q$  is a correction factor that depends on the debond radius ( $a$ ) and the length of the suspended region of the blister. Using finite element analysis, the linear relationship of

strain energy release rate ( $G$ ) with pressure ( $p$ ) and constrain height ( $w$ ), as predicted by Equation (2.40) has been verified [32]. Other variations of the standard blister test include the island [33, 34] and the peninsula blister [35] geometries and the inverted-blister test method [36].

Goussev [37] has presented an alternate method of estimating the interfacial fracture energy in a blister test by characterizing the maximum bending moment ( $M_{\max}$ ) at the crack tip just prior to debonding. The pressurized blister test experiments were conducted using two commercial polymer films bonded to polymethylmethacrylate (PMMA) and polytetrafluoroethylene (PTFE) substrates and the blister profile was measured experimentally using a scanning capacitance microscope. The blister curvature in the vicinity of the crack front, measured experimentally, has been used to calculate  $M_{\max}$  and thereby the fracture energy. A detailed discussion on this approach has been presented in Chapter 4.

## 2.2.2 Indentation tests

Indentation tests are widely used to characterize the properties of thin films and coatings. The approach has several benefits: only a small specimen with little or no preparation is needed to perform the test, a single indentation test can potentially supply several material properties such as hardness, modulus and yield. Nano-indentation has been used for measuring the elastic modulus and hardness of thin films [38]. In case of a thin film coated on a rigid substrate, indentation can be used to delaminate the film from the substrate. By measuring the length of the crack generated at the interface between the film and its substrate and depending on indenter geometry, the interfacial fracture energy can be calculated. The two most popular indenter geometries for measuring brittle thin film adhesion are the cone (plane stress) and the wedge (plane strain) geometries.

### 2.2.2.1 Conical Indentation

Marshall and Evans [39] proposed a method for determination of interfacial toughness for the conical indentation induced thin film delamination. The method accounted for the film buckling event through elastic buckling. The interfacial fracture energy was given as [39]:

$$\frac{G_c E_f}{(1-\nu_f)} = \frac{1}{2} h \sigma_I^2 (1+\nu_f) + (1-\alpha)(h\sigma_R^2) - (1-\alpha)(\sigma_I - \sigma_B)^2 \quad (2.41)$$

where  $E_f$  and  $\nu_f$  are the thin film's elastic modulus and Poisson ratio, respectively,  $h$  is the film thickness and  $\sigma_R$  is the residual stress in the film. Here, a conical diamond tip is indented into the tested thin film and plastically deforms a volume of  $2V_I$  [Figure 2-7(a)]. Indentation causes nucleation and propagation of the interfacial crack. If the indenter is driven deep enough so that the crack reaches its critical buckling length, the film double buckles during indentation. [Figure 2-7(b)]. If the crack length does not reach its critical buckling length on each side of the indenter, single buckling might occur upon tip removal [Figure 2-7(c)]. When the tip is removed, the film under the indenter is no longer under constraint, so it may form a single buckle even in the initial double-buckling case.

The indentation stress,  $\sigma_I$  can be calculated by using the indentation volume,  $V_I$  [39, 40]:

$$\sigma_I = \frac{V_I E_f}{2\pi h a^2 (1-\nu_f)} \quad (2.42)$$

The indentation volume,  $V_I$ , can be calculated from the plastic indentation depth using the tip geometry, and the crack length,  $a$ , which can be directly measured by using microscopy or profilometry techniques [40]. If the crack is driven far enough by the indenter, the film can buckle and then the Euler buckling stress,  $\sigma_B$ , comes into play, which is given as [39, 40]:

$$\sigma_B = \frac{\mu^2 h^2 E_f}{12 a^2 (1-\nu_f)} \quad (2.43)$$

where  $\mu$  is a constant, which depends on the boundary conditions. The term  $\alpha$  is unity if the film does not buckle, otherwise,  $\alpha$  represents the slope of the buckling load versus the edge displacement after buckling and is given as:

$$\alpha = 1 - \frac{1}{1 + 0.902(1-\nu_f)} \quad (2.44)$$

Li et al. [41] have applied nano-indentation combined with atomic force microscopy to measure the fracture toughness of polystyrene/glass interfaces. The film delaminated

when the inelastic penetration depth was approximately equal to, or exceeded, the film thickness. The fracture surface was analyzed by AFM, to characterize the morphology of the indents. The indentation contact radius and delamination size were measured using AFM (Figure 2-8). The fracture toughness of the polystyrenes/glass interface was calculated using Equation (2.41). Kriese, et al. [42] have presented a multilayer indentation approach that extended the single layer analysis developed by Marshalls and Evans [39] for the general case of a multilayer, using standard bending and thin-plate analyses. Thus, this can be applied for measurements using the indentation technique in film/substrate systems that are multilayered.

### 2.2.2.2 Microwedge Indentation

DeBoer and Gerberich [43, 44] have proposed a Microwedge Indentation Test (MWIT) to evaluate the thin film fine line on a thick substrate structure as a fracture mechanics test specimen. In the MWIT, a sharp 90° included angle microwedge uniformly impinges on a thin film line of finite width, and plastically deforms an indentation volume of  $2V_0$  (Figure 2-7), thus the analysis under the assumption of plane strain is appropriate. As the indentation proceeds, an interfacial crack between the interconnect line and the substrate develops if the interface is weak. From this adhesion can be calculated [43]:

$$G_c = \frac{E'_f V_0^2}{2b^2 h a^2} \quad (2.45)$$

where  $a$  is the crack length,  $b$  is the line width,  $E'_f$  is the plane strain elastic modulus of the film and is given as:

$$E'_f = \frac{E_f}{1-\nu_f} \quad (2.46)$$

The  $1/a^2$  dependence in Equation (2.45) is much stronger than the  $1/a^4$  dependence in the conical case, Equation (2.41), meaning that cracks will travel much further for the same indentation volume. This is a direct consequence of the greater driving force of the wedge indenter relative to the conical indenter.

## 2.3 Effect of residual stress on coating delamination

Residual stresses are generated in most coatings as a result of the manufacturing process [45]. They can be introduced by volume changes associated with crosslinking or crystallization, by temperature changes, and by variations in moisture content or other diluents that may occur during processing, curing, or service life [27]. Also, if there is a mismatch in thermal expansion between the coatings and substrate material, significant stresses can build up during cooling from a high deposition temperature [45]. Residual stresses within a coating can lead to [27]:

- i. delamination and premature failures due to the significant interfacial stresses that can occur near free edges and other flaws,
- ii. damage such as environmental stress cracking in service conditions,
- iii. dimensional instability

For a thin, isotropic coating, the residual stress generated in the coating as the coating/substrate system is cooled from temperature  $T_2$  to  $T_1$  is given as [4]:

$$\sigma_r = \int_{T_2}^{T_1} \frac{E_f}{1-\nu_f} (\alpha_f - \alpha_s) dT \quad (2.47)$$

where  $E_f$  is the elastic modulus and  $\nu_f$  is the Poisson's ratio of the coating,  $\alpha_f$  and  $\alpha_s$  are the coefficients of thermal expansion of the coating and substrate respectively. The ability of the coating to carry stresses is significantly reduced when the coating is heated above its glass transition temperature ( $T_g$ ), hence  $T_2$  can be replaced with  $T_g$  in Equation (2.47).

A commonly used experimental method to measure residual stress is the cantilever technique. In this technique, a thin substrate is cantilevered and, as a coating is deposited on it, strains develop in the coating/substrate system due to residual stresses. Using elementary beam theory, the average residual stress in the coating can be related to the curvature before,  $R_b$ , and after,  $R_a$  the coating is deposited using the well-known Stoney equation [46], given as [4]:

$$\sigma_r = \frac{1}{6} \frac{E_s h_s^2}{(1-\nu_s) h_f} \left( \frac{1}{R_a} - \frac{1}{R_b} \right) \quad (2.48)$$

where  $E_s$  is the elastic modulus,  $\nu_s$  is the Poisson's ratio and  $h_s$  is the thickness of the substrate; and  $h_f$  is the thickness of the coating. The radius of curvature or the cantilever end deflection can be measured in real time using optical methods such as laser reflective interferometry[47-49], laser scanning interferometry [50] etc, to monitor the development of residual stress.

## 2.4 Summary

The literature review showed that a number of different techniques exist for measuring coating adhesion. However, there are no universal tests for measuring coating adhesion. This can be explained by the variety of coating systems even a single industry (e.g. microelectronics) may deal with. These represent different types of dissimilar material interfaces that are present in modern electronic devices (metal/metal, metal/ceramic, polymer/metal, polymer/ceramic, etc). Some of the other variations among these coating systems are the degree of adhesion of the coatings, coating thickness and viscoelastic properties of the coating. As a result, a test that works with one coating system may not necessarily work with another. Hence, a versatile and effective test procedure is desired for the purpose of evaluating the adhesion of thin film microelectronics coatings. The objective of this study is to develop a test technique, referred to as the *probe test*, as a quantitative tool for measuring the adhesion in thin adhesive films and coatings. The probe test technique provides the ability to perform the test on a range of specimen geometries and can be applied to as-produced components. Also, the test specimens are simple to fabricate with minimal specimen preparation and without any need for auxiliary adhesives, backings, over-layers etc.

## 2.5 Figures

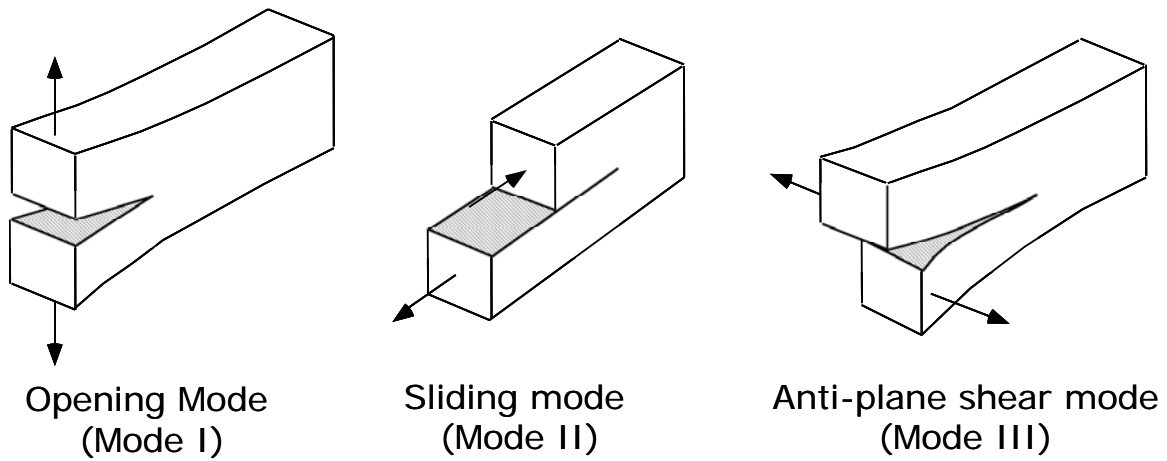


Figure 2-1 Three modes of fracture

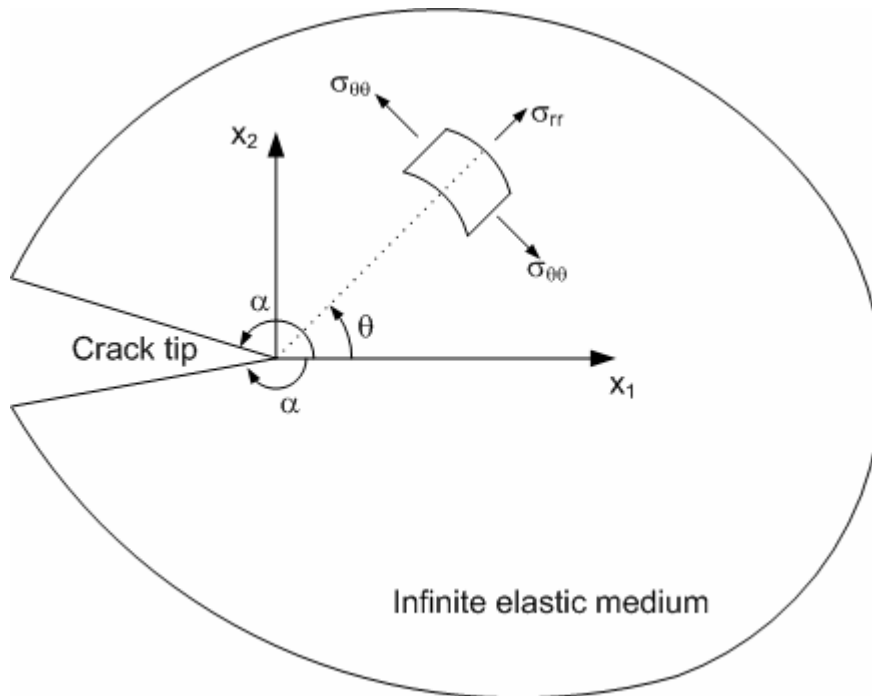
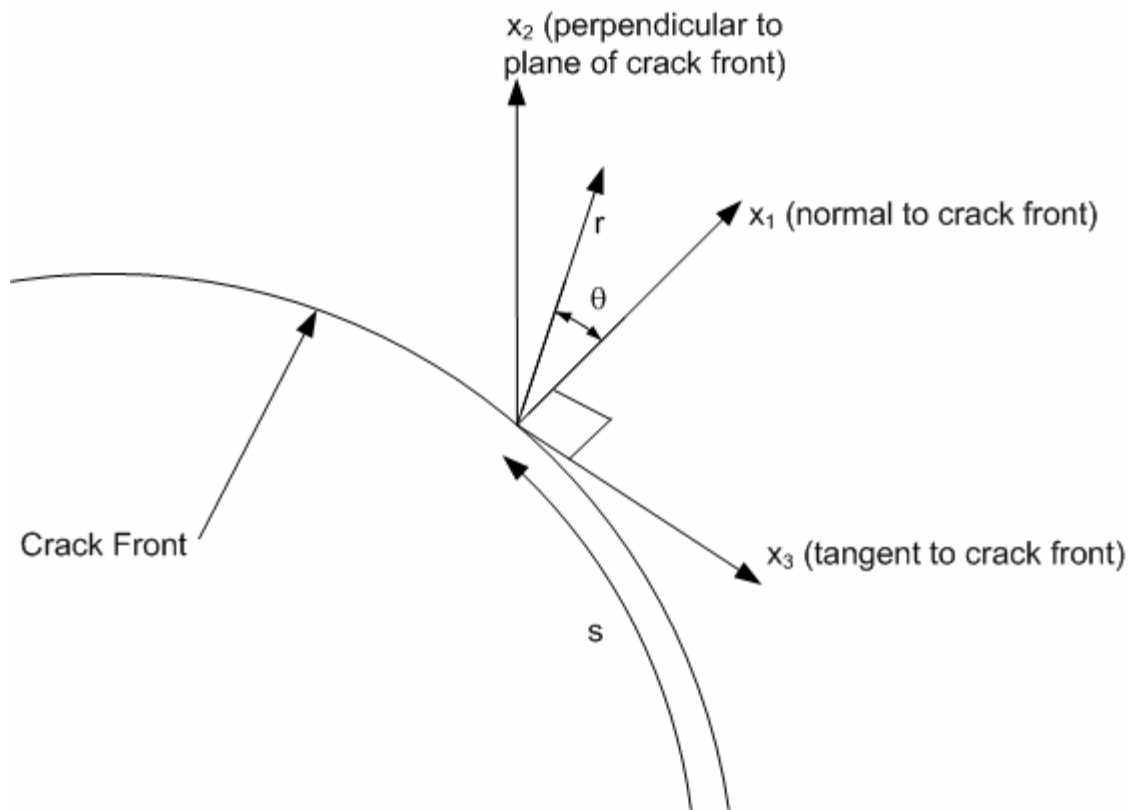
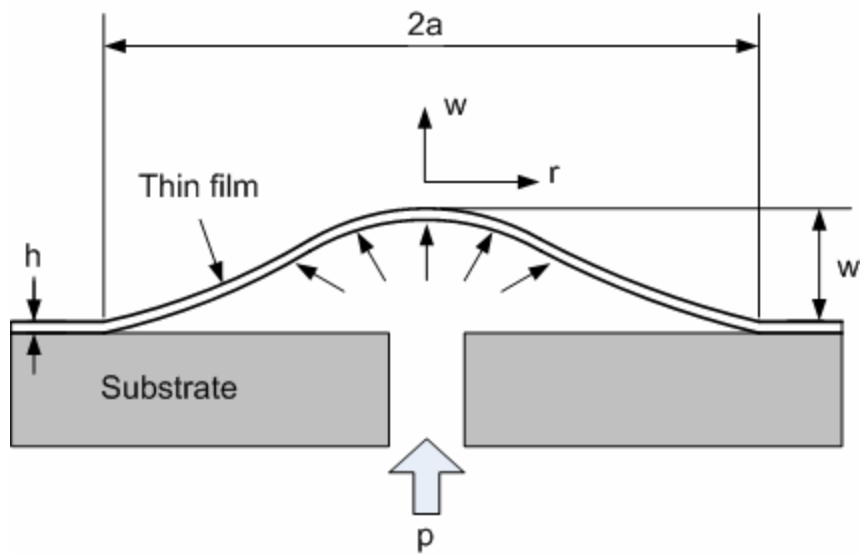


Figure 2-2 A schematic illustration of the stresses near the tip of a crack in an elastic material



**Figure 2-3 A schematic of the local orthogonal Cartesian coordinate system at the points on the crack front used to define J-Integral in three-dimensions**



**Figure 2-4 A schematic of a pressurized circular blister configuration**

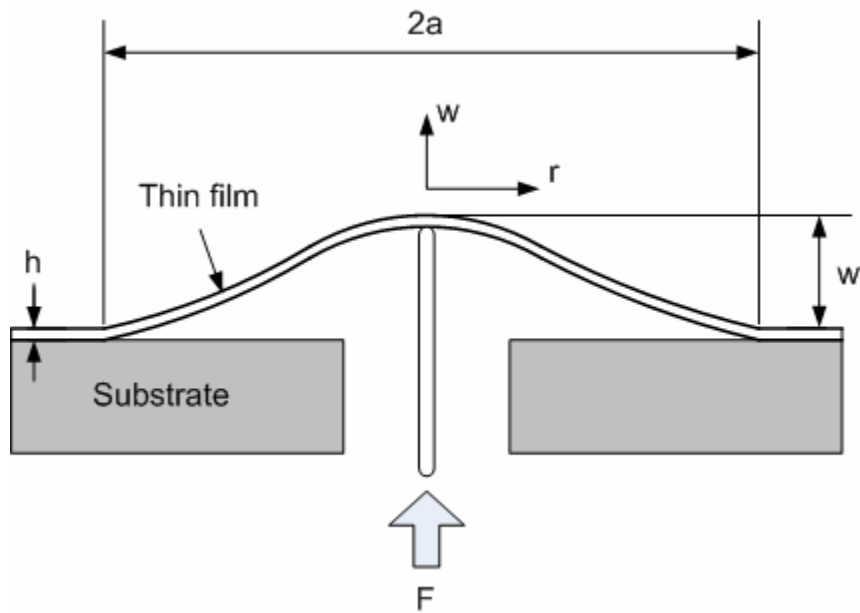


**Figure 2-5 A schematic of a shaft-loaded circular blister configuration**

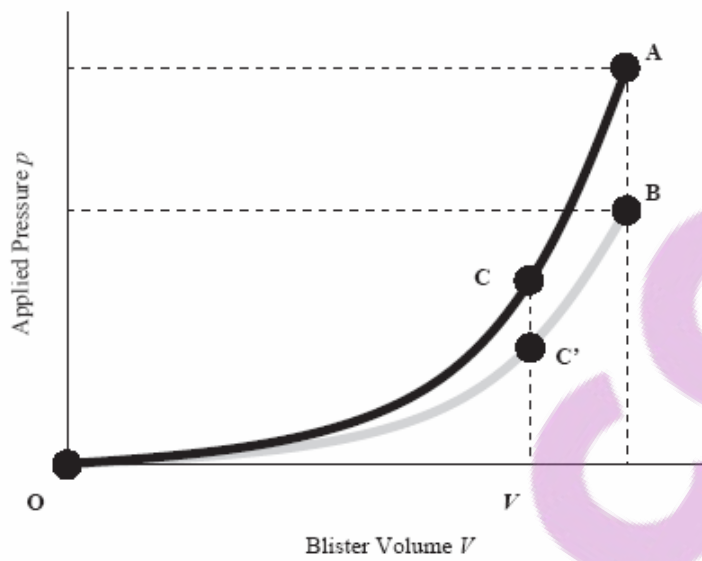


Figure 2-6 Mechanical response of a thin blistering plate. Delamination occurs at A and follows the path AB (Reprinted from [26], with permission from Elsevier)

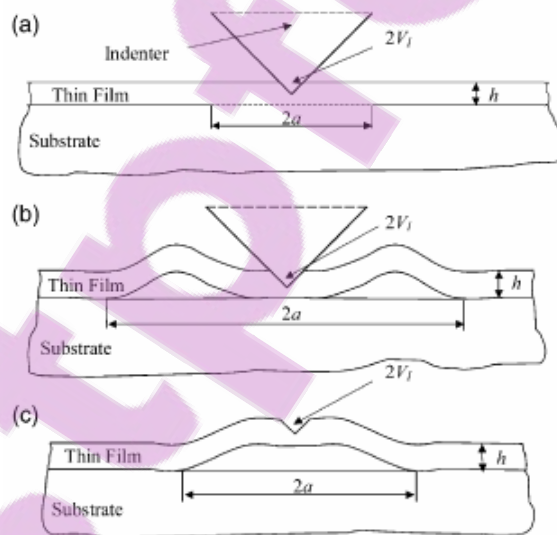
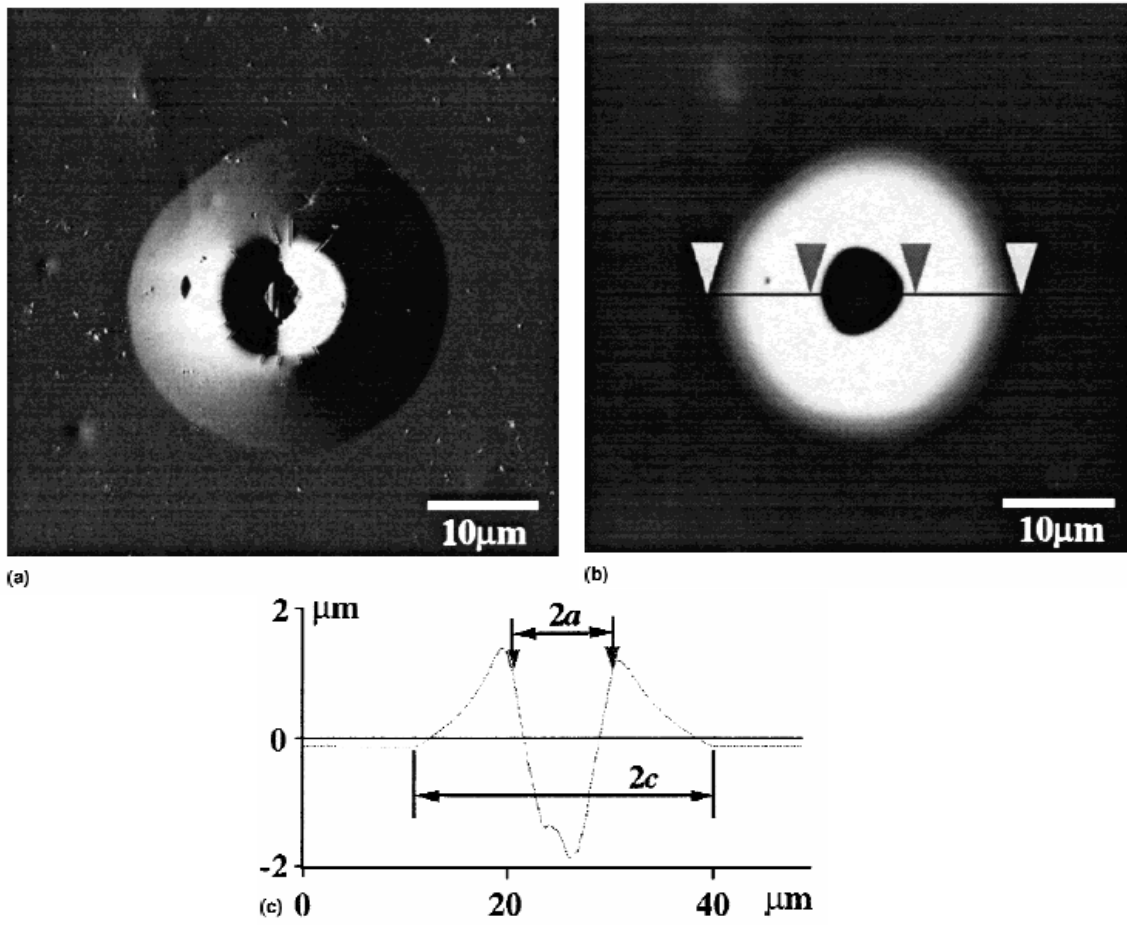


Figure 2-7 A schematic illustration of indentation-induced delamination (a) No buckling during indentation (b) double-buckling during indentation (c) single-buckling after removing the indenter tip (Reprinted from [40], with permission from Elsevier )



**Figure 2-8 Indentation induced delamination: (a) AFM deflection image (b) height image (c) cross sectional trace**

**(Reprinted from [41], with permission from MRS Journal of Materials Research)**

## 2.6 References

1. Irwin, G.R., *Analysis of stresses and strains near the end of a crack traversing a plate*. Journal of Applied Mechanics-Transactions of the ASME, 1957. **24**: p. 361–364.
2. Williams, M.L., *Stress singularities resulting from various boundary conditions in angular corners of plates in extension*. Journal of Applied Mechanics, 1952. **19**: p. 526-528.
3. Williams, M.L., *On the stress distribution at the base of a stationary crack*. Journal of Applied Mechanics, 1957. **24**: p. 109-114.
4. Dillard, D.A. and A.V. Pocius, *The mechanics of adhesion*. Adhesion science and engineering, ed. A.V. Pocius. Vol. 1. 2002, Amsterdam ; Boston: Elsevier.
5. Griffith, A.A., *The Phenomena of Rupture and Flow in Solids*. Philosophical Transactions of the Royal Society of London. Series A, Containing Papers of a Mathematical or Physical Character, 1921. **221**: p. 163-198.
6. Irwin, G.R., *Onset of fast crack propagation in high strength steel and aluminum alloys*. NRL report ; 4763;. 1956, Washington, D.C.: Naval Research Laboratory. i, 15 p.
7. Rice, J.R. and G.C. Sih, *Plane problems of cracks in dissimilar media*. Journal of Applied Mechanics-Transactions of the ASME, 1965. **32**: p. 418-423.
8. Rice, J.R., *Elastic Fracture-Mechanics Concepts for Interfacial Cracks*. Journal of Applied Mechanics-Transactions of the ASME, 1988. **55**(1): p. 98-103.
9. Dundurs, J., *Discussion of edge-bonded dissimilar orthogonal elastic wedges under normal and shear loading*. Journal of Applied Mechanics-Transactions of the ASME, 1969. **36**: p. 650–652.
10. Rice, J.R., Z. Suo, and J.S. Wang, *Mechanics and thermodynamics of brittle interfacial failure in bimaterial systems*. Acta-Scripta Metallurgica Proceedings Series, 1990. **4**(Met.-Ceram. Interfaces): p. 269-294.

11. Hutchinson, J.W., M.E. Mear, and J.R. Rice, *Crack Paralleling an Interface between Dissimilar Materials*. Journal of Applied Mechanics-Transactions of the Asme, 1987. **54**(4): p. 828-832.
12. Hutchinson, J.W. and Z. Suo, *Mixed-Mode Cracking in Layered Materials*. Advances in Applied Mechanics, Vol 29, 1992. **29**: p. 63-191.
13. Rice, J.R., *A path independent integral and the approximate analysis of strain concentration by notches and cracks*. Journal of Applied Mechanics-Transactions of the ASME, 1968. **35**(2): p. 379-386.
14. ABAQUS Inc, *ABAQUS Version 6.5 Documentation*. 2004, ABAQUS, Inc: Providence, RI, USA.
15. Courtin, S., et al., *Advantages of the J-integral approach for calculating stress intensity factors when using the commercial finite element software ABAQUS*. Engineering Fracture Mechanics, 2005. **72**(14): p. 2174-2185.
16. Dannenberg, H., *Measurement of adhesion by a blister method*. Journal of Applied Polymer Science, 1961. **5**(14): p. 125-134.
17. Williams, M.L., *The continuum interpretation for fracture and adhesion*. Journal of Applied Polymer Science, 1969. **13**(1): p. 29-40.
18. Anderson, G.P., J. Bennetts, and K.L. DeVries, *Analysis and testing of adhesive bonds*. 1977, New York: Academic Press. xviii, 255.
19. Sizemore, J., et al., *Measuring the adhesion of diamond thin films to substrates using the blister test*, in *Mechanical Behavior of Diamond and Other Forms of Carbon*, M.D. Drory, et al., Editors. 1995. p. 197-207.
20. Jeong, H.S., et al., *Adhesion Study of Polyimide to Si Surfaces*. Surface and Interface Analysis, 1992. **18**(4): p. 289-292.
21. Jensen, H.M., *The Blister Test for Interface Toughness Measurement*. Engineering Fracture Mechanics, 1991. **40**(3): p. 475-486.
22. Hinkley, J.A., *A Blister Test for Adhesion of Polymer-Films to SiO<sub>2</sub>*. Journal of Adhesion, 1983. **16**(2): p. 115-125.
23. Gent, A.N. and L.H. Lewandowski, *Blow-Off Pressures for Adhering Layers*. Journal of Applied Polymer Science, 1987. **33**(5): p. 1567-1577.

24. Briscoe, B.J. and S.S. Panesar, *The Application of the Blister Test to an Elastomeric Adhesive*. Proceedings of the Royal Society of London Series a-Mathematical Physical and Engineering Sciences, 1991. **433**(1887): p. 23-43.
25. O'Brien, E.P., et al., *Strain energy release rates of a pressure sensitive adhesive measured by the shaft-loaded blister test*. Journal of Adhesion, 2003. **79**(1): p. 69-97.
26. Arjun, A. and K.T. Wan, *Derivation of the strain energy release rate  $G$  from first principles for the pressurized blister test*. International Journal of Adhesion and Adhesives, 2005. **25**(1): p. 13-18.
27. Wan, K.T., S. Guo, and D.A. Dillard, *A theoretical and numerical study of a thin clamped circular film under an external load in the presence of a tensile residual stress*. Thin Solid Films, 2003. **425**(1-2): p. 150-162.
28. Guo, S., *Experimental and numerical investigations on the durability and fracture mechanics of the bonded systems for microelectronics application*, in *Engineering Mechanics*. 2003, University Libraries Virginia Polytechnic Institute and State University: Blacksburg, Va.
29. Guo, S., K.T. Wan, and D.A. Dillard, *A bending-to-stretching analysis of the blister test in the presence of tensile residual stress*. International Journal of Solids and Structures, 2005. **42**(9-10): p. 2771-2784.
30. Lai, Y.H. and D.A. Dillard, *A Study of the Fracture Efficiency Parameter of Blister Tests for Films and Coatings*. Journal of Adhesion Science and Technology, 1994. **8**(6): p. 663-678.
31. Chang, Y.S., Y.H. Lai, and D.A. Dillard, *The Constrained Blister - a Nearly Constant Strain-Energy Release Rate Test for Adhesives*. Journal of Adhesion, 1989. **27**(4): p. 197-211.
32. Lai, Y.H. and D.A. Dillard, *Numerical-Analysis of the Constrained Blister Test*. Journal of Adhesion, 1990. **33**(1-2): p. 63-74.
33. Allen, M.G. and S.D. Senturia, *Analysis of Critical Debonding Pressures of Stressed Thin-Films in the Blister Test*. Journal of Adhesion, 1988. **25**(4): p. 303-315.

34. Allen, M.G. and S.D. Senturia, *Application of the Island Blister Test for Thin-Film Adhesion Measurement*. Journal of Adhesion, 1989. **29**(1-4): p. 219-231.
35. Dillard, D.A. and Y. Bao, *The Peninsula Blister Test - a High and Constant Strain-Energy Release Rate Fracture Specimen for Adhesives*. Journal of Adhesion, 1991. **33**(4): p. 253-271.
36. Fernando, M. and A.J. Kinloch, *Use of the Inverted-Blister Test to Study the Adhesion of Photopolymers*. International Journal of Adhesion and Adhesives, 1990. **10**(2): p. 69-76.
37. Goussev, O.A., K. Zeman, and U.W. Suter, *Local bending moment as a measure of adhesion: The blister test*. Journal of Adhesion, 1996. **56**(1-4): p. 45-57.
38. Oliver, W.C. and G.M. Pharr, *An Improved Technique for Determining Hardness and Elastic-Modulus Using Load and Displacement Sensing Indentation Experiments*. Journal of Materials Research, 1992. **7**(6): p. 1564-1583.
39. Marshall, D.B. and A.G. Evans, *Measurement of Adherence of Residually Stressed Thin-Films by Indentation .1. Mechanics of Interface Delamination*. Journal of Applied Physics, 1984. **56**(10): p. 2632-2638.
40. Volinsky, A.A., N.R. Moody, and W.W. Gerberich, *Interfacial toughness measurements for thin films on substrates*. Acta Materialia, 2002. **50**(3): p. 441-466.
41. Li, M., et al., *Adhesion of polymer-inorganic interfaces by nanoindentation*. Journal of Materials Research, 2001. **16**(12): p. 3378-3388.
42. Kriese, M.D., W.W. Gerberich, and N.R. Moody, *Quantitative adhesion measures of multilayer films: Part I. Indentation mechanics*. Journal of Materials Research, 1999. **14**(7): p. 3007-3018.
43. DeBoer, M.P. and W.W. Gerberich, *Microwedge indentation of the thin film fine line .1. Mechanics*. Acta Materialia, 1996. **44**(8): p. 3169-3175.
44. DeBoer, M.P. and W.W. Gerberich, *Microwedge indentation of the thin film fine line .2. Experiment*. Acta Materialia, 1996. **44**(8): p. 3177-3187.
45. Wiklund, U., J. Gunnars, and S. Hogmark, *Influence of residual stresses on fracture and delamination of thin hard coatings*. Wear, 1999. **232**(2): p. 262-269.

46. Stoney, G.G., *The Tension of Metallic Films Deposited by Electrolysis*. Proceedings of the Royal Society of London. Series A, Containing Papers of a Mathematical and Physical Character, 1909. **82**(553): p. 172-175.
47. Kempf, J., M. Nonnenmacher, and H.H. Wagner, *Electron and Ion-Beam Induced Heating Effects in Solids Measured by Laser Interferometry*. Applied Physics a-Materials Science & Processing, 1993. **56**(4): p. 385-390.
48. Sternheim, M., W. Vangelder, and A.W. Hartman, *A Laser Interferometer System to Monitor Dry Etching of Patterned Silicon*. Journal of the Electrochemical Society, 1983. **130**(3): p. 655-658.
49. Wu, C.H., et al., *Laser Reflective Interferometry for Insitu Monitoring of Diamond Film Growth by Chemical Vapor-Deposition*. Journal of Applied Physics, 1993. **73**(6): p. 2977-2982.
50. Kempf, J., *Optical Insitu Sputter Rate Measurements during Ion Sputtering*. Surface and Interface Analysis, 1982. **4**(3): p. 116-119.

## **Chapter 3      Experimental Procedure**

### **3.1 Introduction**

This chapter describes the experimental procedure of the probe test for measuring the adhesion of thin adhesive films and coatings. The technique was initially developed by the Hewlett-Packard Company for qualitatively measuring the adhesion of thin film microelectronic coatings. The test geometry is shown in Figure 3-1. In this technique, an inclined needle-like probe with a conical tip was advanced underneath the free edge of a thin polymeric coating bonded to a substrate, causing the edge to lift-up from the surface of the substrate. A debond was thus initiated at the loading point and propagated as a semi-circular crack at the interface as the probe slid under the coating. In the present work, the sample system used was a thin film epoxy polymer coated silicon system. Using this epoxy coating/Si substrate system, a standard test procedure was developed for testing a thin adhesive coating/substrate system.

### **3.2 Specimen Preparation**

Silicon wafers (8" in diameter) with polished front surfaces and non-polished back surfaces were obtained from the Sumitomo Mitsubishi Silicon Group. The Si wafers were subjected to surface modification using a silane coupling agent via a sol-gel reaction. This was accomplished by treating the Si wafers in a 0.1M 3-aminopropyltriethoxysilane (3-APS) solution (with 5% v/v 0.1M HCl aqueous solution) for 30 minutes at room temperature. After the silane treatment, the wafers were rinsed with pure ethanol and dried in air at room temperature. The modified wafers were subsequently heated in an oven at 110 °C for about 30 minutes. These wafers were then cut into small pieces (approximately 20 mm x 30 mm x 1 mm) and coated with the model epoxy adhesive to make probe test specimens.

The model epoxy adhesive consists of bis-phenol F diglycidyl ether (Epon 862), 1,4-butanediol (10 phr, i.e., parts per hundred resin), and 4-methyl-2-phenylimidazole (3 phr) as curing agent [1]. The Epon 862 resin has an epoxide equivalent weight of 171

g/mole. Figure 3-2 shows the chemical structure of the components of model epoxy. To prepare the epoxy, a relatively low viscosity clear liquid was obtained by stirring Epon 862 and 1,4-butanediol together at about 80 °C for several minutes. Subsequently, 4-methyl-2-phenylimidazole catalyst was dissolved in this mixture with stirring for about 15 minutes to obtain a homogenous mixture, which was then cast on the Si substrates. The epoxy mixture cast on Si substrates was cured at 130 °C for 1 hour. A differential scanning calorimetry (DSC) study showed that the fully cured model epoxy polymer had a glass transition temperature ( $T_g$ ) of 110 °C [1, 2]. Also, using dynamic mechanical analysis (DMA), the elastic modulus of the fully cured model epoxy was measured as 2.7 GPa [2]. The coefficient of thermal expansion ( $\alpha_{epoxy}$ ) of the model epoxy below the glass transition region was measured using dilatometric studies as  $70 \times 10^{-6} / ^\circ\text{C}$  [2]. The Poisson's ratio of the model epoxy was assumed as 0.32 [3, 4].

The model epoxy adhesive was cast onto the surface modified silicon substrate (approximately 20 mm x 30 mm x 1 mm), using a polytetrafluoroethylene (PTFE) template (approximately 10 mm x 10 mm x 70  $\mu\text{m}$ ) and sandwiched between two PTFE plates, as shown in Figure 3-3. The thickness of the PTFE template thus controlled the epoxy coating thickness to about 70  $\mu\text{m}$ . Another thin PTFE film was placed on top of the coating area to ensure a smooth coating surface. The assembly was held together with two medium size binder clips and cured at 130 °C for 1 hour in air. To ensure the possibility for a precise probe penetration at the coating/substrate interface, excess polymer spew around the square coating area was removed using a razor blade. This process was carried out in a delicate fashion so that the vertical coating edge that is perpendicular to the Si substrate was exposed, while preserving straightness and bond integrity along the coating edge.

### 3.3 Probe Test

The probe test experiment was implemented using either an optical microscope (Section 3.3.1) or an optical profiler (Section 3.3.2) to determine the extent of debonding. The experimental apparatus is shown in Figure 3-4 and Figure 3-9. The debonds were created using a 1  $\mu\text{m}$  tip radius tungsten probe (American Probe & Technologies Inc,

Model: 72T-I3/10x1.24'', 0.02 inch probe shank diameter, 6° cone angle) attached to the articulating arm of a Karl Suss micromanipulator probehead (SUSS PH150). The micromanipulator was attached rigidly to an aluminum plate. The micromanipulator base was encompassed by a rectangular rubber lip, which used a vacuum based system to increase the frictional contact force between the micromanipulator base and the aluminum plate underneath, thus providing a rigid support for the micromanipulator. The epoxy coated silicon substrate specimen was secured onto the microscope/profiler stage with another aluminum clamping plate, such that both the probehead and the specimen were mounted on the same plate. The micromanipulator was operated in XYZ directions by manually turning the knurled thumbscrews. The micromanipulator probe arms facilitated the use of different probe angles in the experiment. A probe angle (defined as the angle between the probe and the plane of the substrate) of  $25.0^\circ \pm 1.0$  was used to obtain results. The micro-probe was positioned until the probe tip just touched the Si substrate surface. This was achieved by observing the probe tip through the microscope as it was vertically moved in the  $z$  – direction until it just came into contact with the Si substrate at which point the probe tip would start moving horizontally in the  $x$  - direction. The micro-probe was aligned perpendicular to the coating edge and was introduced into the coating/Si interface to initiate a debond. The applied force from the probe tip caused an initial deformation in the coating at the interface which in turn created a crack in the coating/Si interface. The propagating crack produced a characteristic semi-circular debond radiating outward from the point of intrusion. As the probe tip advanced along the coating/Si interface, the debond propagated outward, and the profile and dimensions of the debonded area changed accordingly. A schematic of the test geometry is shown in Figure 3-1.

### 3.3.1 Implementation using Optical Microscopy

The probe test experiments were performed on a Nikon UM-2 Measurescope microscope with a digital measuring stage, as shown in Figure 3-4. Figure 3-5 shows a typical debonding event as a result of penetration of the probe tip along the coating/Si interface where  $\delta$  is the probe penetration distance,  $a$  is the debond radius along the probe direction ( $x$  – direction),  $b$  is the debond radius perpendicular to the probe

direction (y – direction),  $h$  is the thickness of the coating and  $w_0$  is the maximum vertical separation distance of the coating from the substrate at the point of intrusion. From the geometry, including the half cone angle of the probe ( $3^\circ$ );  $w_0$  can be related to  $\delta$  as:

$$w_0 = \delta \tan(25^\circ + 3^\circ) = \delta \tan(28^\circ) \quad (3.1)$$

Figure 3-6 shows the growth of the debond in the coating at different probe penetration distances for the specimen. At a probe penetration distance of 100 micron, the initial debond appeared to be very small and circular. At 150 micron, the debond area grew into a semi-circular profile. The coating appeared to be crushed near the initial probe entry region, likely due to the high contact stresses that might occur prior to debonding. As the probe penetration distance increased, the semi-circular crack front became more pronounced and the debond size increased in the x and y directions. The crack front observed in most cases was approximately semi-circular in shape. Also, the size of the debond is related to the interfacial fracture energy; poorer adhesion results in larger debonds for a given probe displacement.

The radii ( $a, b$ ) of the debond in the x and y directions were recorded for successive values of probe penetration distances. In the present study, the crack front was visually observed to be approximately semi-circular in shape, however in order to characterize the shape of the debond using experimental measurements, the shape was assumed as semi-elliptic during measurements, hence the debond radii ( $a, b$ ) along and perpendicular to the probe direction were recorded. The probe penetration distance ( $\delta$ ) was recorded from the x-displacement of the micromanipulator arm. The radii ( $a, b$ ) of the debond were recorded by using the digital measuring stage. From the radii ( $a, b$ ), the area ( $A$ ) of the debond can be calculated as:

$$A = \frac{1}{2} \pi ab \quad (3.2)$$

Also, the aspect ratio ( $\gamma$ ) of the debond lengths is defined as:

$$\gamma = \frac{a}{b} \quad (3.3)$$

Figure 3-7 shows the debond area ( $A$ ) and the debond aspect ratio ( $\gamma$ ) calculated as a function of the probe penetration distance ( $\delta$ ) for the coating/Si specimen. The debond aspect ratio ( $\gamma$ ) values lie in the range  $0.95 \leq \gamma \leq 1.15$ . The shape of the debond can thus be approximated as semi-circular for the further analytical and numerical modeling in the present study. In the study done by Dingying Xu [1] on the probe test technique, it was shown that the debond aspect ratio ( $\gamma$ ) was lower for aged coating/Si specimens which were exposed to thermal and chemical environments. Lower values of debond aspect ratio ( $\gamma$ ) would imply a semi-elliptical shape; thus it can be concluded that under different environmental conditions the debond crack front becomes semi-elliptical in shape.

The experiments were conducted using the same coating/Si specimen for five different debonds; for each debond the measurements were collected for different values of probe penetration distances. Figure 3-8 shows the debond radius ( $a$ ) as a function of the probe penetration distance ( $\delta$ ) for the different debonds created on the coating/Si specimen. It can be observed from Figure 3-8 the debond radius ( $a$ ) is almost linearly dependent on the probe penetration distance ( $\delta$ ). Thus, it can be concluded that the growth of the debond is linearly dependent on the applied displacement (or applied load). The linear dependence of the debond size on the applied load also shows that growth of the crack front is stable and quasi-static, and that there is no slip-stick crack growth behavior. It was also observed from Figure 3-8 that the measured debond radius ( $a$ ) values vary considerably for the five different debonds that were created on the same specimen. This variation in the debond radius ( $a$ ) values could be due to variability of the experimental test method like change in probe angle due to flexing of the probe shaft, difference in the probe incremental displacement etc.

Lastly, a limitation with the optical microscopy technique is that the coating should be optically transparent (at least partially), so that the debond is clearly visible through the optical microscope. Also estimation of the exact position of the crack front as seen through the eyepiece of the microscope is based on the judgment of the human eye (Figure 3-5).

### 3.3.2 Implementation using WYKO® Optical Profiler

In order to use optically opaque epoxy coatings, the probe test experiments were conducted under a WYKO® optical profiler NT2000™. The experimental probe test setup under the WYKO® profiler is shown in Figure 3-9. The WYKO® NT2000™ optical profiler combines non-contact interferometry with advanced automation for highly accurate, 3D surface topography measurements. The working principle of the WYKO® optical profiler is shown in Figure 3-10 [5]. Light from an illuminator is reflected on the interferometric objective lens by a beam-splitter. Once the light reaches the objective, another beam-splitter separates the light into two beams. One beam, the reference beam, reflects from a super smooth reference mirror in the objective, while the other (the test beam) reflects from the surface of the specimen and back to the objective. When the surface of the specimen is in focus, the two light beams recombine and form an interference pattern of light and dark bands called fringes. The interference pattern is received by a CCD camera and the signal is transferred to the computer to be processed by the WYKO® Vision32® (version 2.210) software.

The WYKO® profiler was used in the Vertical Scanning Interferometry (VSI) mode in order to examine the entire debond displacement profile. The VSI mode allows the measurement of rough surfaces and steps up to several millimeters high. In vertical scanning interferometry, white light reflected from a reference mirror combines with light reflected from the sample to produce interference fringes, where the best contrast fringes occurs at best focus. The white - light source is filtered with a neutral density filter, which preserves the short coherent length of the white light, and the system measures the degree of fringe modulation, or coherence. The interferometric objective moves vertically to scan the surface at varying heights. A motor with feedback from an LVDT (linear variable differential transformer) precisely controls the motion. The irradiance signal is thus sampled at fixed intervals as the optical path difference (OPD) is varied by the continuous translation along the vertical axis through focus. Low – frequency components are first removed from the signal; the signal is rectified by square - law

---

® WYKO NT series, NT2000 are registered trademarks of Veeco Instruments Inc.

Copyright © 1999 Veeco Instruments Inc.

detection, and then filtered. Finally, the peak of the low-pass filter output is located and the vertical position that corresponds to the peak is recorded. To increase the resolution of the measurement beyond the sampling interval, a curve-fitting interpolation technique is used. Because white light has a short coherence length, interference fringes are present only over a very shallow depth for each focus position. Fringe contrast at a single sample point reaches a peak as the sample is translated through focus. The system uses a series of advanced computer algorithms to demodulate the envelope of the fringe signal. Finally the vertical position corresponding to the peak of the interference signal is extracted for each point on the surface.

The three dimensional surface topography of the debond created in the coating was measured using the WYKO<sup>®</sup> optical profiler. The profiler recorded the z-displacement for each point (x,y) on the surface of debonded coating. The vertical resolution (i.e. in z – displacement) of the measurement was  $\pm 3\text{nm}$  [5]. The magnification objective used was 10X, which has an optical resolution of  $\pm 1\ \mu\text{m}$ , a working distance of 7.4 mm and a field of view of 0.62 mm x 0.47mm. The practical maximum slope that could be measured using this objective was  $13.1^\circ$  and the spatial (i.e. in x, y) sampling interval using this 10X objective was  $0.84\ \mu\text{m} \times 0.98\ \mu\text{m}$ .

In the probe test experiments, the debonds were created in the coating/Si specimen using a  $1\ \mu\text{m}$  tip radius tungsten probe held at a probing angle of  $25.0^\circ \pm 1.0$ . The measurements were obtained for five different debonds created on the specimen; for each debond the measurements were collected for probe penetration distances ( $\delta$ ) of 100, 150, 200, 250 and 300 microns. A typical debond surface topography obtained is shown in Figure 3-11.

The WYKO<sup>®</sup> profiler was unable to obtain any surface profile in regions where surface gradients exceeded the limits of the 10X objective. As noted earlier, the maximum slope that can be measured using this objective is  $13.1^\circ$ , whereas the debond was created using a probing angle of  $25.0^\circ \pm 1.0$ . Thus, as shown in Figure 3-12, the regions with no surface profile data appear in black in the surface topography image. This limited the measurement of the maximum vertical separation distance of the coating from the substrate ( $w_0$ ) (Figure 3-5). Also, the area of the debond that can be measured is

limited by the field of view of the objective. Hence, as shown in Figure 3-12 and illustrated in Figure 3-13, debond surface topography data was obtained near the crack front of the debond; and for large size debonds, around the centerline of the debond (shown in Figure 3-13), thereby excluding regions away from the debond centerline region. Due to this reason, the interfacial fracture energy calculation along the crack front using the WYKO<sup>®</sup> profiler data is performed using surface topography data in the range  $-45^\circ \leq \theta \leq 45^\circ$ , where  $\theta$  is the angle along the crack front from the debond centerline as shown in Figure 3-13.

Another major problem with the WYKO<sup>®</sup> profiler technique was the large quantity of noise captured in the surface topography data by the optical profiler. This noise creates difficulties in quantitative analysis of the data and was partially removed using band pass filters.

As stated in the Section 3.3.1, the experimental implementation of the probe test under the optical microscope only worked in cases of transparent coatings where the crack front was visible to the human eye through the microscope. For the case of the WYKO<sup>®</sup> optical profiler, the coating surface should be optically opaque and the surface should be sufficiently smooth to allow light to be reflected off the surface in order to obtain a good quality image. This was found to be an advantage since most of the coating systems of interest were opaque in nature. The optical microscope only allows the measurement of the overall size (in terms of radii) of the debond, whereas by using the WYKO<sup>®</sup> profiler, an accurate measurement of displacement profile of the debonded coating, particularly in the region around the crack front, was obtained. Thus, compared to the optical microscopy technique, the displacement profile data from the WYKO<sup>®</sup> profiler allows more versatile and advanced mechanics techniques to be used to model the coating behavior and estimate the interfacial fracture energy, which will be discussed in later chapters. However, the large quantity of noise in the surface topography data from the WYKO<sup>®</sup> profiler was a major problem in obtaining an accurate estimation of interfacial fracture energy ( $G_c$ ).

### 3.4 Summary

The probe test for measuring adhesion of thin films and coatings was implemented under an optical microscope and an optical profiler. A thin film adhesive (epoxy polymer) coated silicon substrate specimen was used to conduct probe test experiments. A semi-circular crack front was observed at the interface of the coating/Si substrate specimen as the probe slid underneath the coating. Using an optical microscope, the debond radius was recorded as a function of probe penetration distance. The experimental data showed that the crack growth was stable and linearly dependent on the applied load. Using the WYKO<sup>®</sup> optical profiler, the vertical displacement profile of the debond around the crack front region was measured for different debond sizes. Using the optical microscope or the WYKO<sup>®</sup> optical profiler, the probe test technique can be used with both transparent as well as opaque coatings. A major limitation with the WYKO<sup>®</sup> profiler technique was the large quantity of noise in the surface topography data obtained from the optical profiler, thus creating difficulties in the quantitative analysis of the data to obtain an accurate estimation of interfacial fracture energy ( $G_c$ ).

### 3.5 Figures

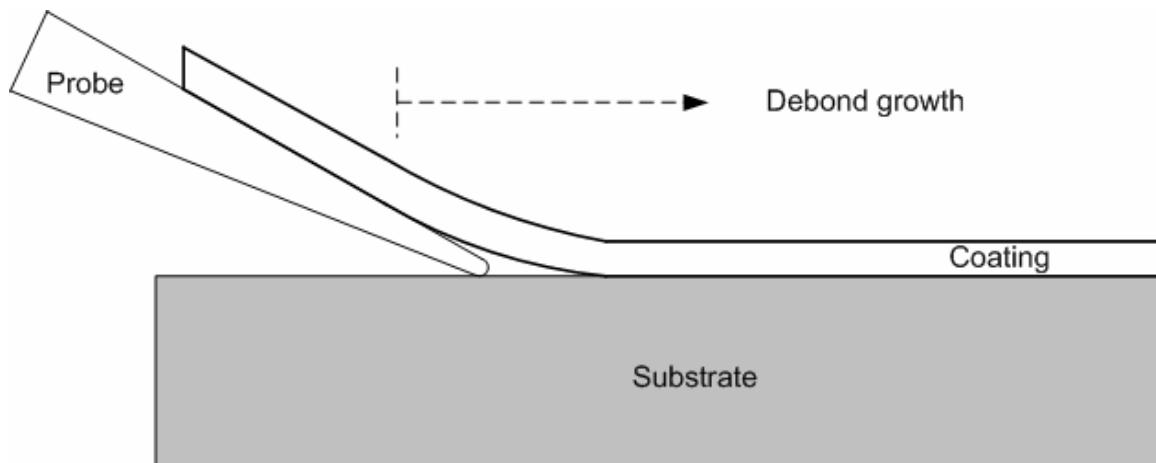


**Figure 3-1** A schematic illustration of the probe advancing beneath a coating that is debonding from the substrate

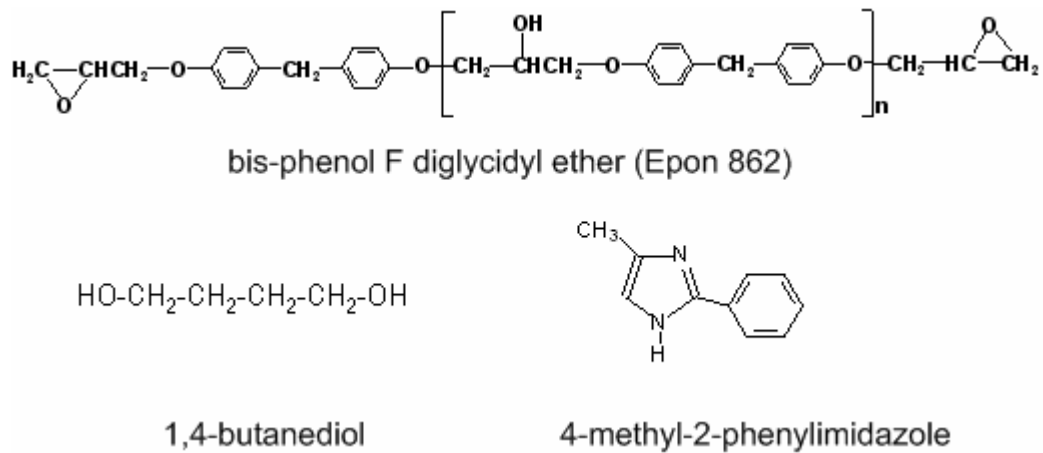


**Figure 3-2** Chemical structure of the components of model epoxy adhesive  
(Reprinted from [1], with permission from author)

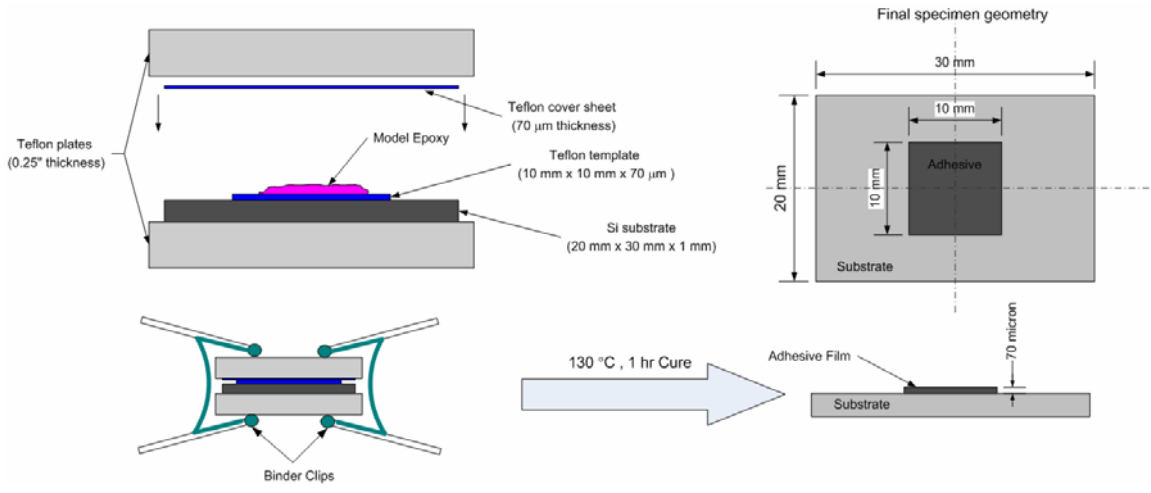


**Figure 3-3 A schematic illustration of specimen fabrication for the probe test**

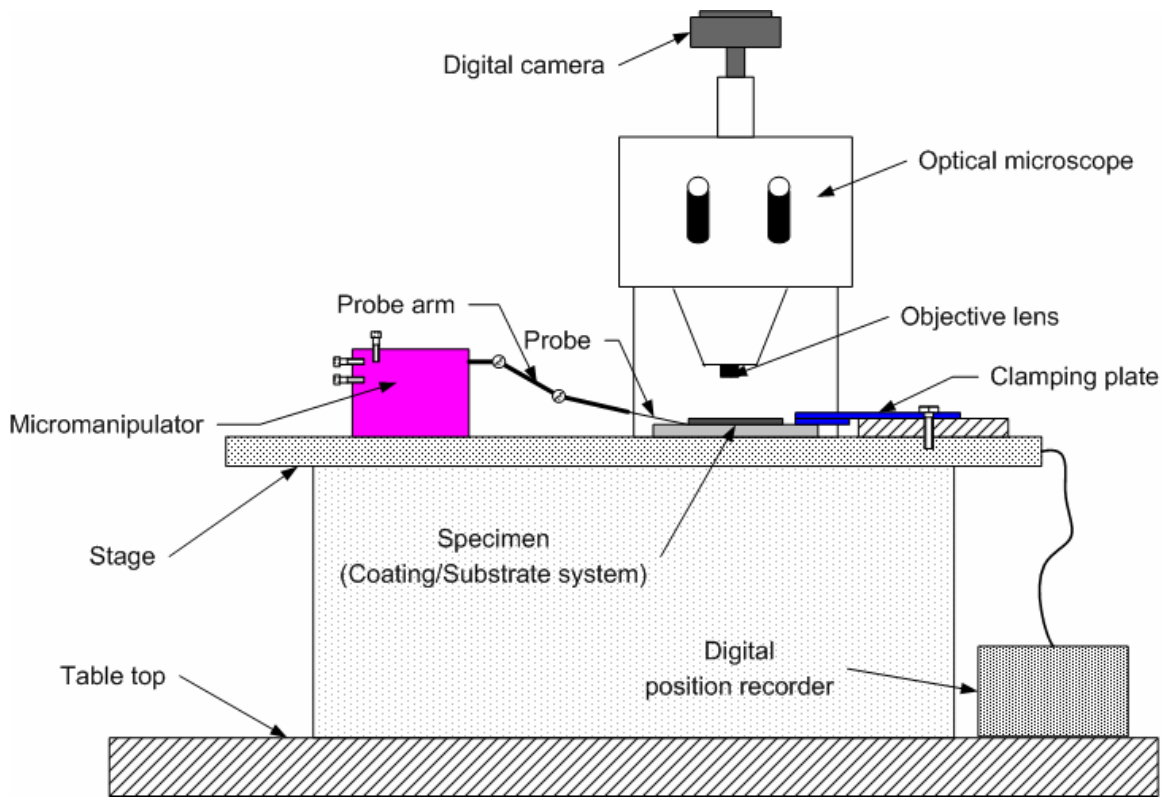


**Figure 3-4 A schematic diagram of the experimental probe test setup under the optical microscope**

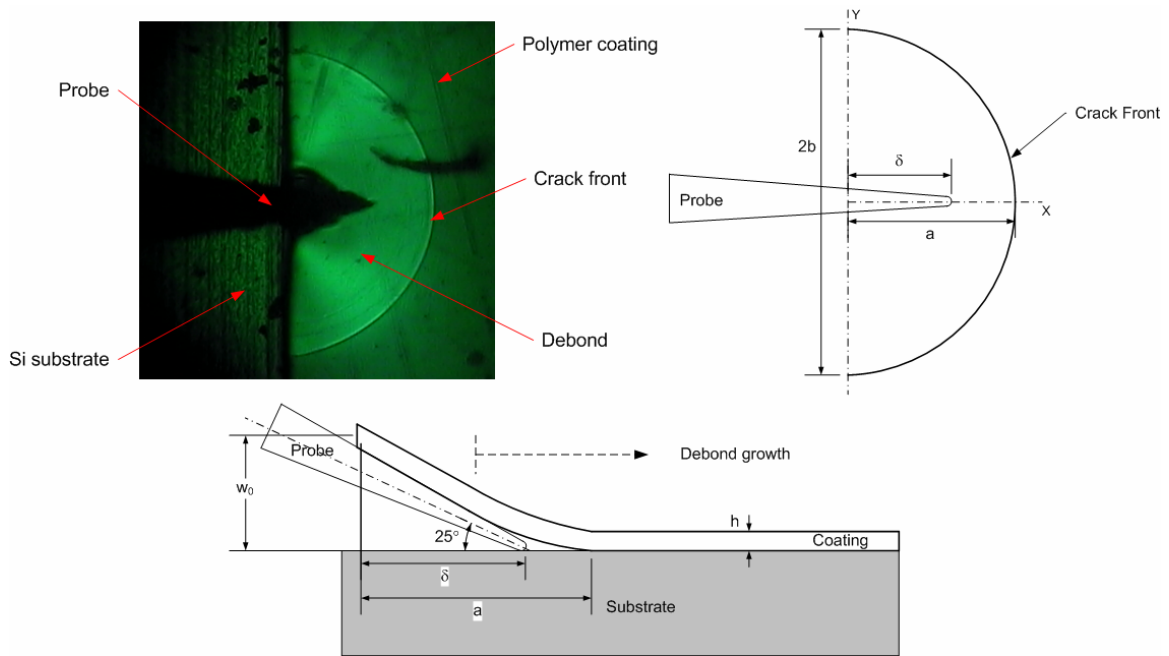


**Figure 3-5 A typical debonding event in the coating for the coating (70 $\mu$ m)/Si substrate specimen using a probe angle of 25 $^\circ$**

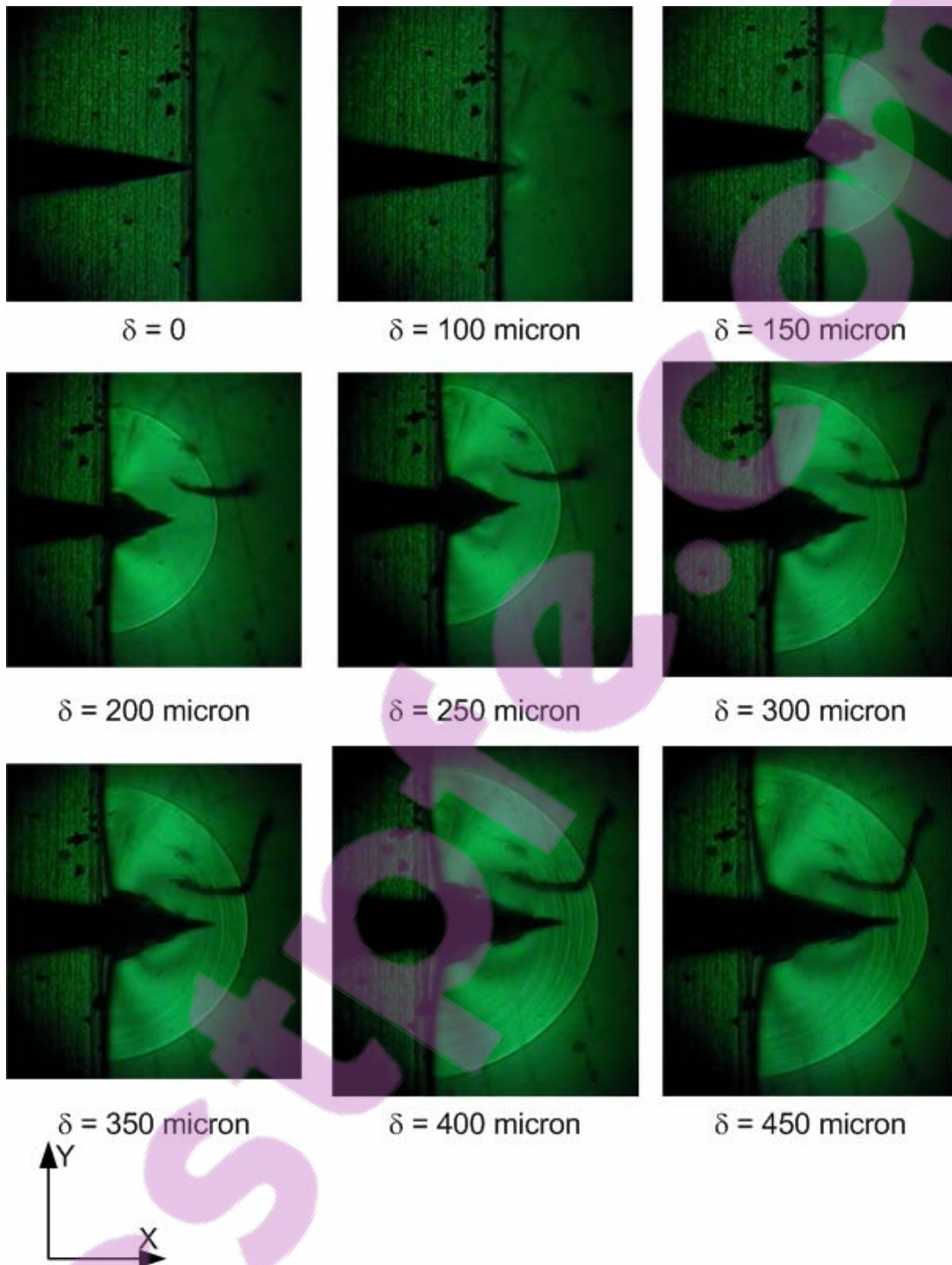


**Figure 3-6 Debond growth in the coating at different probe penetration distances ( $\delta$ ) for the coating (70 $\mu$ m)/Si substrate specimen using a probe angle of 25°**

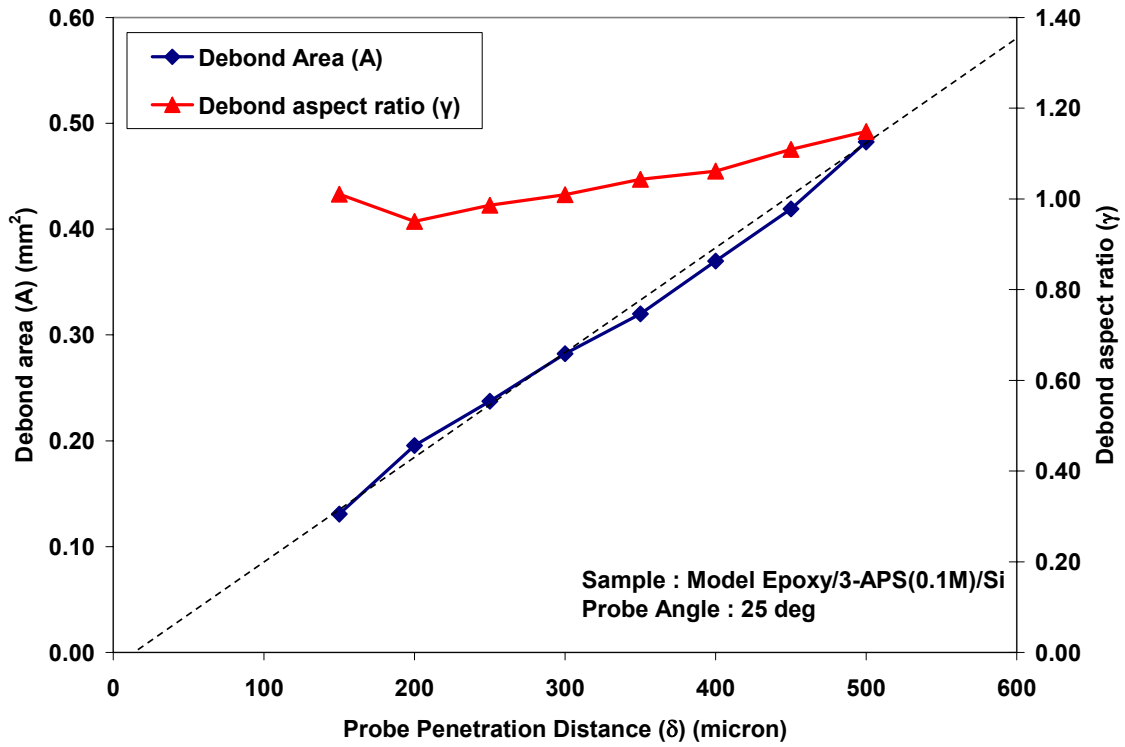


**Figure 3-7 Plots of debond area (A) and debond aspect ratio ( $\gamma$ ) as a function of probe penetration distance ( $\delta$ ) for the coating (70 $\mu\text{m}$ )/Si substrate specimen using a probe angle of 25°**

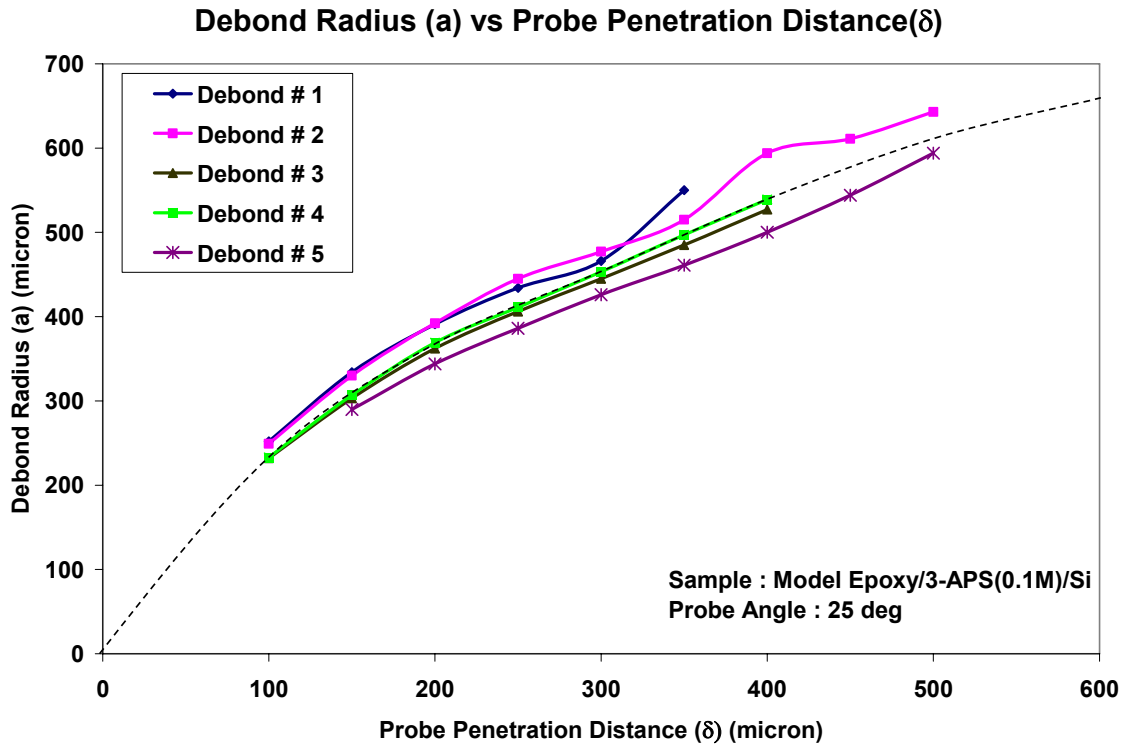


**Figure 3-8 Plots of debond radius (a) along the probe direction as a function of probe penetration distance ( $\delta$ ) for the coating (70 $\mu$ m)/Si substrate specimen using a probe angle of 25°**

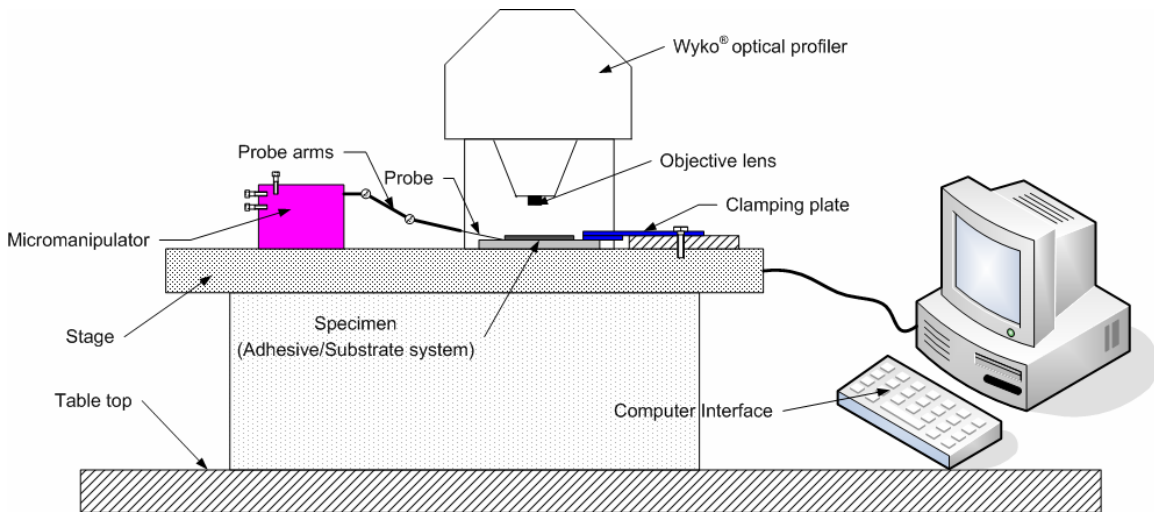


**Figure 3-9 A schematic of the experimental probe test setup under the WYKO® optical profiler**

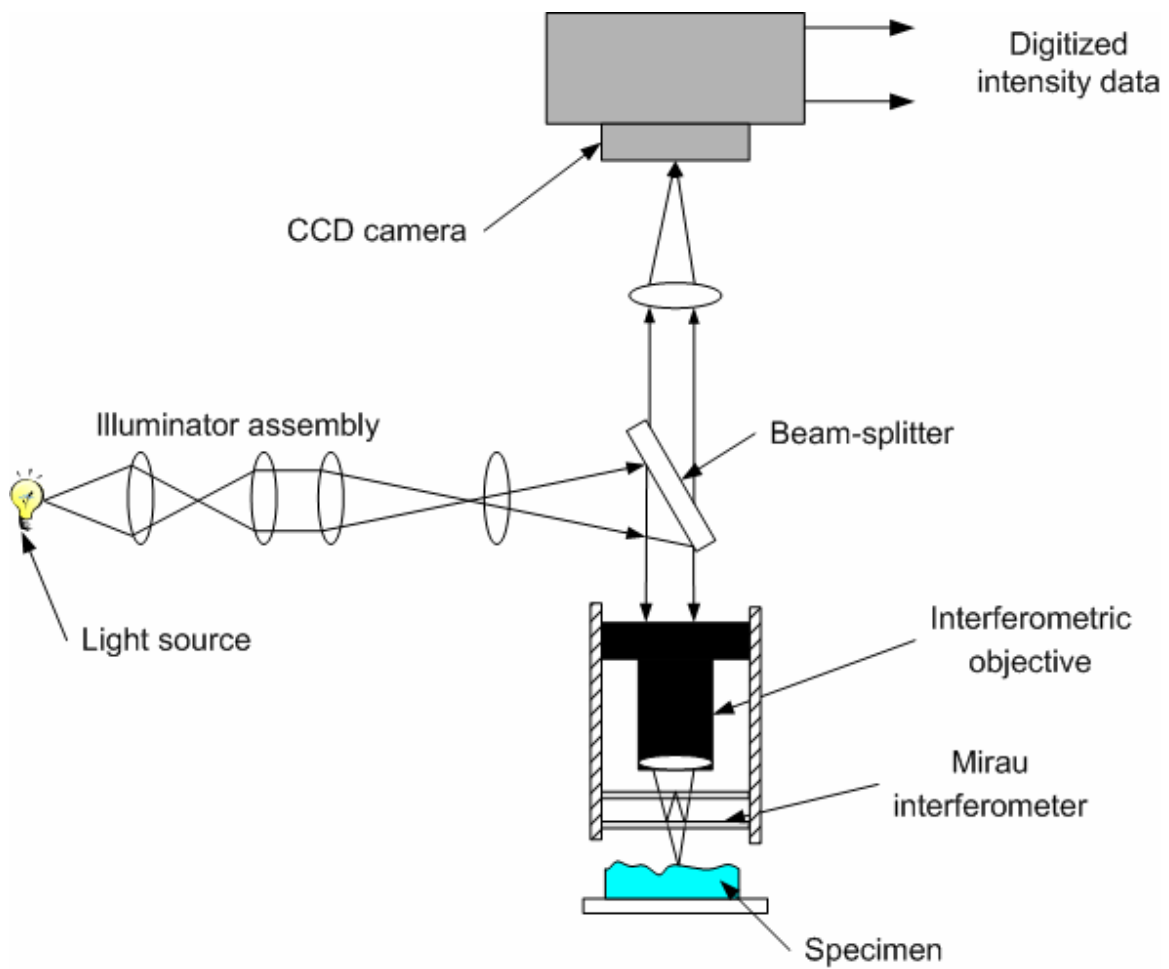


**Figure 3-10 A schematic illustration of the working principle of the interferometric-based WYKO<sup>®</sup> optical profiler**

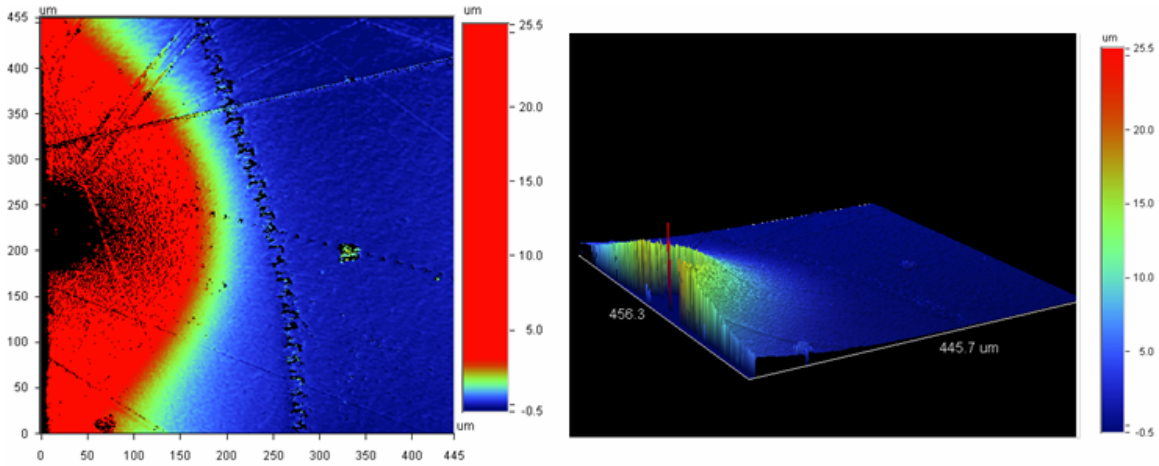


**Figure 3-11** Debond surface topography using WYKO<sup>®</sup> optical profiler for the coating (70 $\mu\text{m}$ )/Si substrate specimen using a probe angle of 25 $^\circ$

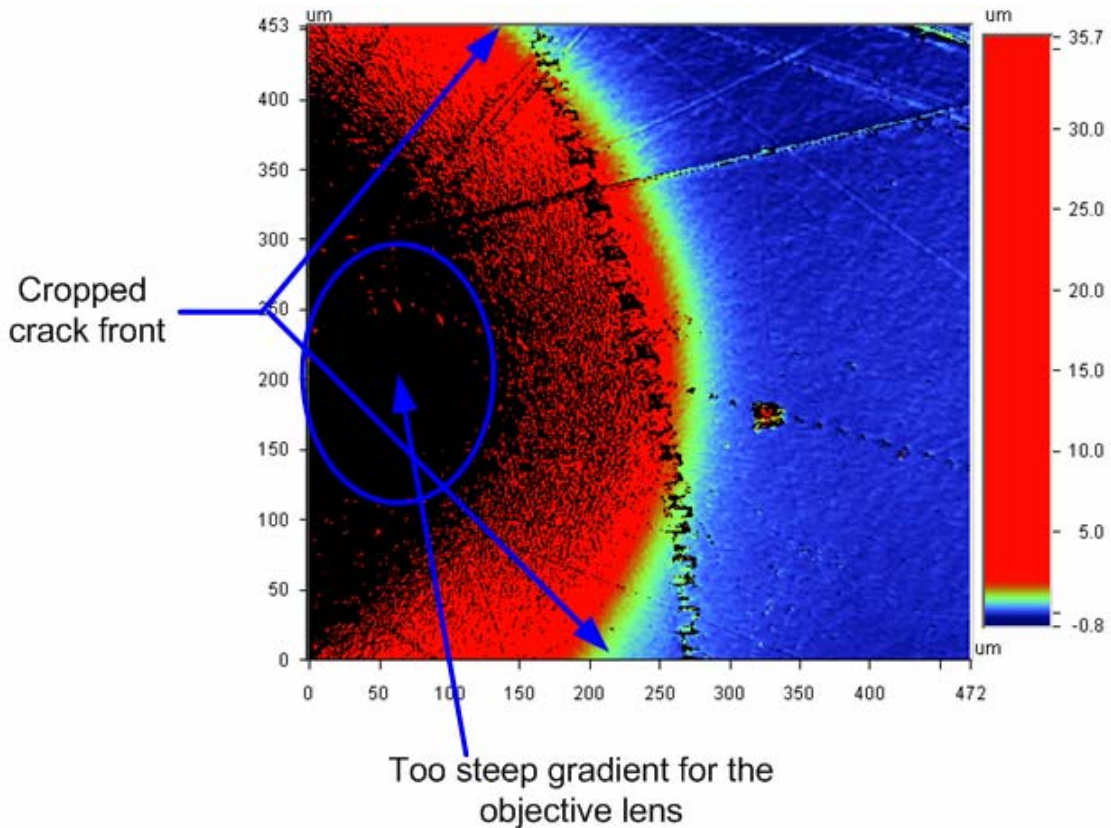


**Figure 3-12** A surface topography image obtained using the WYKO<sup>®</sup> profiler for a debond of larger size than the field of view of the objective lens; image quality is bad in regions of steep gradient and a cropped image of the debond is obtained

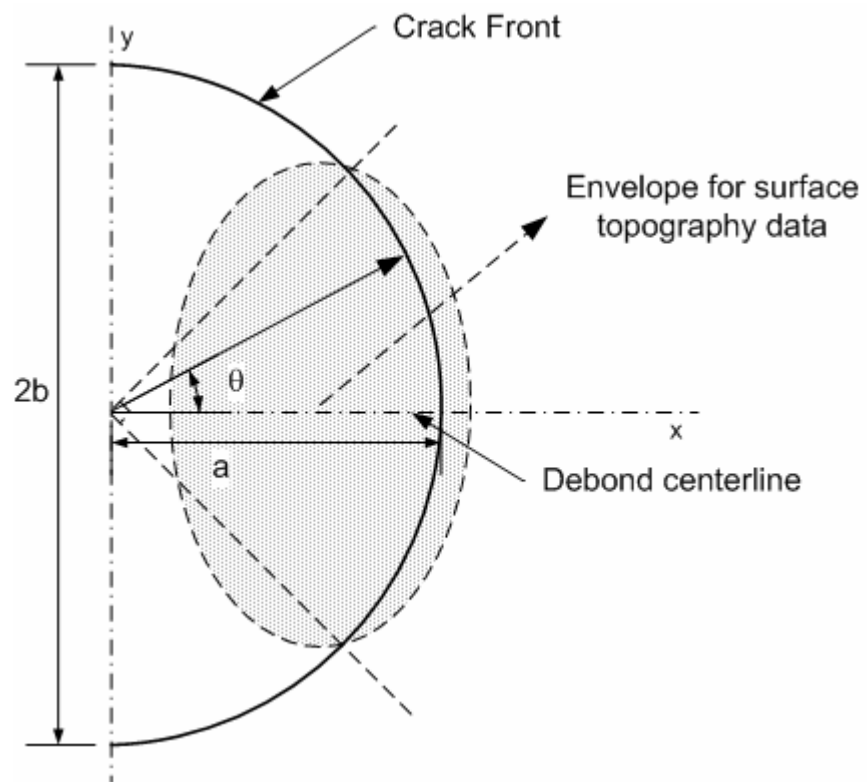


**Figure 3-13 An illustration of the envelope for the debond surface topography data obtained near the crack front region**

### 3.6 References

1. Xu, D., *Durability and adhesion of a model epoxy adhesive bonded to modified silicon substrates*, in *Chemistry*. 2004, University Libraries Virginia Polytechnic Institute and State University: Blacksburg, Va.
2. Case, S.L., *Fundamental importance of fillers, cure condition, and crosslink density on model epoxy properties*, in *Chemistry*. 2003, University Libraries Virginia Polytechnic Institute and State University: Blacksburg, Va.
3. Dillard, D.A., et al. *Experimental evaluation of the probe test for measuring thin film adhesion*. in *Electronic and Photonic Packaging, Electrical Systems and Photonic Design and Nanotechnology - 2003*. 2003.
4. Mount, K.P., *Finite element analysis of probe induced delamination of a thin film at an edge interface*, in *Mechanical Engineering*. 2003, University Libraries Virginia Polytechnic Institute and State University: Blacksburg, Va.
5. Veeco Metrology Group, *Wyko Surface Profilers - Technical Reference Manual*. 1999, Veeco Instruments, Inc: USA

## Chapter 4 Analytical Methods

### 4.1 Introduction

This chapter explores the analytical techniques which have been used to provide a quantitative measure of the adhesion in the epoxy coating/Si substrate system, using the probe test technique. The interfacial fracture energy,  $G_c$  (or critical strain energy release rate), provides an intuitively meaningful measure of the energy required to debond a unit area of an interfacial crack in an adhesive bond and hence characterizes the resistance of the adhesive bond to debond by fracture. Using classical analytical solutions, the probe test geometry, as described in Chapter 2, has been modeled to calculate the interfacial fracture energy for the epoxy coating/Si substrate system using two approaches: shaft – loaded blister approximation and curvature method.

### 4.2 Shaft – loaded blister approximation

The probe test experiments were performed on a Nikon UM-2 Measurescope microscope with a digital measuring stage, as described in Chapter 3. A typical debond created by lifting the edge of a coating is shown in Figure 4-1. The debond was created as the conical probe tip was forced under the coating. The radii of the debond along and perpendicular to the probe direction were recorded for a particular value of probe penetration distance. It was shown in Chapter 3 that the crack front of the debond was approximately semi-circular in shape.

Closed form solutions for the interfacial fracture energy can be obtained [1] for a circular shaft – loaded blister geometry, shown in Figure 4-2. Thus, in order to develop an analytical model for the debond in the probe test geometry, the analytical expressions from the circular shaft – loaded blister geometry were used as an approximation for the probe test geometry. It should be noted that the geometry of the debond in the probe test geometry is similar to a half – blister with a free edge as compared to the approximation used for a circular blister geometry.

The geometry of a shaft – loaded circular blister can be analyzed as a circular plate loaded at the center (Figure 4-2). Since the blister is bonded ahead of the crack tip, a clamped boundary condition can be assumed at the edges of the circular plate. Depending on the maximum deflection ( $w_0$ ) and radius ( $a$ ) of the plate relative to its thickness ( $h$ ), the following classifications are used in literature:

- i. Thin plate:  $\frac{a}{h} > 10$  [2]
- ii. Thick plate:  $0.2 < \frac{a}{h} < 10$  [2]
- iii. Semi – infinite medium:  $\frac{a}{h} < 0.2$  [3]
- iv. Small deflections:  $\frac{w_0}{h} < 0.5$  [1]
- v. Large deflections:  $\frac{w_0}{h} > 0.5$  [1]

For a linearly elastic thin plate, the analytical solutions for small and large deflections of a clamped circular plate have been presented by Timoshenko [1]. The following analysis is presented using a thin plate formulation for small and large deflections of the plate. Also, a correction for thick plates is presented.

## 4.2.1 Theory

### 4.2.1.1 Thin plate - small deflections

Assuming linear elasticity and small deflections ( $\frac{w_0}{h} < 0.5$ ), the deflection profile for a clamped circular plate loaded at the center, as shown in Figure 4-2, is given by Timoshenko's solution [1] as:

$$w(r) = \frac{Pr^2}{8\pi D} \log \frac{r}{a} + \frac{P}{16\pi D} (a^2 - r^2) \quad (4.1)$$

where  $P$  is the applied point load,  $a$  is the blister radius, and  $D$  is the flexural rigidity of the plate. For a homogenous material, the flexural rigidity,  $D$ , can be written as

$$D = \frac{Eh^3}{12(1-\nu^2)} \quad (4.2)$$

where  $E$  is the elastic modulus,  $\nu$  is the Poisson's ratio, and  $h$  is the thickness of the plate. The solution given by Equation (4.1) assumes the following boundary conditions for the clamped edges:

$$\text{At the edges } (r = a): \quad w(a) = 0 \quad \& \quad \left. \frac{dw}{dr} \right|_{r=a} = 0 \quad (4.3)$$

From Equation (4.1), the maximum deflection at the center of the plate ( $r = 0$ ) is given as:

$$w_0 = \frac{Pa^2}{16\pi D} \quad (4.4)$$

The elastic energy stored in an elastic medium is given as:

$$U_E = \int_0^{w_0} P \cdot dw_0 \quad (4.5)$$

Rearranging Equation (4.4) in terms of  $P$ , Equation (4.5) can be written as

$$U_E = \int_0^{w_0} P \cdot dw_0 = \int_0^{w_0} \frac{16\pi D}{a^2} w_0 dw_0 = \frac{8\pi D w_0^2}{a^2} = \frac{1}{2} P w_0 \quad (4.6)$$

The interfacial fracture energy ( $G_c$ ), is related to  $U_E$  as:

$$G_c = \left. \frac{dU_E}{dA} \right|_{w_0} = \frac{1}{2\pi a} \left. \frac{dU_E}{da} \right|_{w_0} \quad (4.7)$$

where  $A$  is the debonded blister area ( $A = \pi a^2$ ).

Using Equation (4.6),  $G_c$  is given as

$$G_c = \frac{1}{2\pi a} \left. \frac{dU_E}{da} \right|_{w_0} = \frac{1}{2\pi a} \frac{d}{da} \left( \frac{P w_0}{2} \right) = \left( \frac{P}{4\pi a} \right) \frac{dw_0}{da} = \frac{P^2}{32\pi^2 D} \quad (4.8)$$

Equation (4.8) for the interfacial fracture energy is load dependent; however, the applied load  $P$  is difficult to measure in the present version of the probe test experiment. As described in Chapter 3, the load applied to advance the probe along the adhesive/substrate interface is achieved by manually turning the micromanipulator thumbscrews. Thus, an alternative displacement-based form of  $G_c$  is obtained by substituting  $P$  from Equation (4.4) into Equation (4.8), and is given as:

$$G_c = \frac{1}{32\pi^2 D} \left( \frac{16\pi D w_0}{a^2} \right)^2 = 8D \frac{w_0^2}{a^4} \quad (4.9)$$

#### 4.2.1.2 Thin plate - large deflections

For large deflections ( $\frac{w_0}{h} > 0.5$ ), the maximum deflection at the center of a clamped circular plate is given by Timoshenko's solution [1, 4] as:

$$16Dw_0 + \frac{191}{648}Ehw_0^3 = \frac{Pa^2}{\pi} \quad (4.10)$$

This solution assumes the following boundary conditions for loosely clamped edges, wherein out-of-plane deflections are prevented but in-plane displacements are free:

$$\begin{aligned} \text{At the edges } (r = a): \quad w(a) = 0 \quad ; \quad \left. \frac{dw}{dr} \right|_{r=a} = 0 & \quad \text{Bending BCs} \\ N_r|_{r=a} = 0 \quad ; \quad N_{r\theta}|_{r=a} = 0 & \quad \text{Stretching BCs} \end{aligned} \quad (4.11)$$

where  $N_r$  is the in-plane radial force per unit length and  $N_{r\theta}$  is the in-plane shear force per unit length in the plate. In Equation (4.11), the first two boundary conditions are used to solve the governing equations of von Karman non-linear plate theory [4] corresponding to bending deformation and the last two boundary conditions are used to solve the governing equations corresponding to stretching deformation. The in-plane forces ( $N_r, N_{r\theta}$ ) in the plate and the corresponding stretching boundary conditions were neglected in the small deflection formulation presented earlier in Section 4.2.1.1.

As mentioned earlier, the clamped boundary conditions at the edges of the circular plate correspond to the adhesion ahead of the crack tip in the blister. The bending boundary conditions in Equation (4.11) constrain the out-of-plane deflection ( $w$ ) and slope ( $\frac{dw}{dr}$ ) at the crack tip. However, since the blister is bonded only at the bottom layer, in-plane strains due to elastic stretching deformation may arise at the crack tip through the thickness of the blister. Thus, stretching boundary conditions in Equation (4.11) represents free in-plane radial and shear deflections at the crack tip; hence the term loosely clamped edges.

Using Equation (4.10), we get:

$$\frac{dw_0}{da} = \frac{Pa}{\pi \left( 8D + \frac{191}{432}Ehw_0^2 \right)} \quad (4.12)$$

Using Equation (4.12) in Equations (4.6) and (4.7), the expression for  $G_c$  for large deflections is given as:

$$G_c = \frac{1}{2\pi a} \frac{dU_E}{da} \Big|_{w_0} = \left( \frac{P}{4\pi a} \right) \frac{dw_0}{da} = \frac{P^2}{4\pi^2 \left( 8D + \frac{191}{432} Ehw_0^2 \right)} \quad (4.13)$$

Using Equation (4.10) and (4.13), the displacement-based expression for  $G_c$  is given as:

$$G_c = \frac{\left( 16Dw_0 + \frac{191}{648} Ehw_0^3 \right)^2}{4a^4 \left( 8D + \frac{191}{432} Ehw_0^2 \right)} \quad (4.14)$$

#### 4.2.1.3 Thick plate - large deflections

The thin plate approximations become unreliable in the case of plates of considerable thickness, hence a thick plate formulation is used for the following radius to thickness ratios:  $0.2 < \frac{a}{h} < 10$ . Thin plate theories cannot be applied for analyzing thick plates due to the following reasons:

- i. Lack of ideal fixity at the edges of thick plates
- ii. Additional deflection in the thicker plates resulting from shear stresses

For thick plates ( $0.2 < \frac{a}{h} < 10$ ) with clamped edges, a correction is applied to the values of maximum deflection  $w_0$  at the center of a clamped circular plate, given as:

$$w_0^{corrected} = \frac{w_0}{C} \quad (4.15)$$

where the correction factor  $C$  is defined using an empirical approximation as [2]:

$$C = 1 + 5.72 \left( \frac{h}{a} \right)^2 \quad (4.16)$$

The corrected maximum deflection  $w_0^{corrected}$  values are then used in analytical expressions obtained using thin plate formulations. Also, it should be noted that in the probe test experiments, the maximum deflection  $w_0$  was calculated using experimental data (See Equation (4.18)).

For large deflections ( $\frac{w_0}{h} > 0.5$ ), using the corresponding expression from thin plate – large deflection formulations (Equation (4.14)), the displacement-based expression for  $G_c$  for thick plate – large deflections is given as:

$$G_c = \frac{\left[ 16Dw_0^{corrected} + \frac{191}{648} Eh(w_0^{corrected})^3 \right]^2}{4a^4 \left[ 8D + \frac{191}{432} Eh(w_0^{corrected})^2 \right]} \quad (4.17)$$

## 4.2.2 Results and discussion

As mentioned earlier in Section 4.2, the debond in the probe test was semi-circular in shape with one edge free and the other edge clamped, however the closed-form solutions presented in Section 4.2.1 using different plate theory formulations were obtained from a shaft-loaded circular blister geometry with clamped edges. Also, the deflection profile or shape of a circular blister is different from the deflection profile of the debonded coating in the probe test. The gradient of the blister surface at the center of the blister ( $r = 0$ ) is zero; however the debonded coating surface has a finite gradient at the corresponding point ( $r = 0$ ). Thus, this approximation of the probe test geometry by a circular blister geometry is somewhat crude and may possibly introduce an error in the results presented in this section.

For the probe test geometry shown in Figure 4-3,  $\delta$  is the probe penetration distance,  $a$  is the debond radius along the probe direction,  $h$  is the thickness of the coating and  $w_0$  is the maximum vertical separation distance of the coating from the substrate at the point of intrusion. In the probe test experiments, the probe tip was inclined at an angle of  $25.0^\circ \pm 1.0$ . From the geometry, including the half cone angle of the probe ( $3^\circ$ );  $w_0$  can be related to  $\delta$  as:

$$w_0 = \delta \tan(25^\circ + 3^\circ) = \delta \tan(28^\circ) \quad (4.18)$$

Using the probe test experiments, measurements were obtained for 5 different debonds created on the specimen; for each debond the measurements were collected for different values of probe penetration distances. Figure 4-4 shows the debond radius ( $a$ )

recorded as a function of the probe penetration distance ( $\delta$ ) for the different debonds created on the coating/Si specimen using a probe angle of 25.0°.

Using Equation (4.18), the maximum deflection ( $w_0$ ) of the coating was calculated from the different probe penetration distance ( $\delta$ ) values. Figure 4-5 shows the normalized debond radius ( $\frac{a}{h}$ ) as a function of normalized coating deflection ( $\frac{w_0}{h}$ ). It was observed that all the data points lie in the region  $\frac{w_0}{h} > 0.5$  and  $\frac{a}{h} < 10$ . This showed that the deformations of the coatings lie in the domain of large deflection and thick plate theory.

Using Equation (4.9) for thin plate - small deflection theory, the interfacial fracture energy,  $G_c$  was calculated for different debond sizes. Figure 4-6 shows the  $G_c$  values as a function of debond radius for five different debonds.

Using Equation (4.14) for thin plate - large deflection theory, the interfacial fracture energy,  $G_c$  was calculated for different debond sizes. Figure 4-7 shows the  $G_c$  values as a function of debond radius for five different debonds.

For thick plate – large deflection theory, the  $w_0$  values were divided by the correction factor C as given in Equation (4.16). Then, using Equation (4.17) for large deflection theory, the interfacial fracture energy,  $G_c$  was calculated for different debond sizes. Figure 4-8 shows the  $G_c$  as a function of debond radius for five different debonds.

It was observed from Figure 4-6, Figure 4-7 and Figure 4-8 that the  $G_c$  values vary considerably for the five different debonds that were created on the same specimen. This variation in  $G_c$  values could be due to variability of the experimental test method like change in probe angle due to flexing of the probe shaft, difference in the probe incremental displacement, etc. Also, since the debonds were created at different locations in the specimen, small variations in the coating mechanical properties ( $E, \nu$ ) and coating thickness ( $h$ ) at the different debond locations could lead to variation in the calculated  $G_c$  values. As it can be seen from Equations (4.2), (4.9), (4.14) and (4.17),  $G_c$  is proportional to  $h^3$ , thus a small variation in coating thickness ( $h$ ) would introduce a

considerable error in the predicted  $G_c$  values. However, this local variation of the coating thickness ( $h$ ) was not measured experimentally, instead an average thickness ( $h$ ) value of 70  $\mu\text{m}$  was used for  $G_c$  calculations for the five different debonds. Also, the values used for the mechanical properties ( $E, \nu$ ) of the coating, as presented in Chapter 3, were obtained using testing of bulk model epoxy adhesive specimen. The in-situ (i.e. when applied to substrate) coating mechanical properties can be affected by the degree of cure, aging effects and environmental conditions (e.g. temperature and humidity). Local changes in these coating mechanical properties ( $E, \nu$ ) at different debond locations were not taken into account in the present work and could result in error in the predicted  $G_c$  values.

Finally, the  $G_c$  values for the five different debonds were averaged, for each of the plate theory formulation. Figure 4-9 shows a comparison of the  $G_c$  values calculated using the different plate theory formulations.

In thin plate theory, based on the Love-Kirchhoff approximation, the transverse normal and shear strain in the plate are neglected [1]. Thus for thin plate theory, this results in an over-estimation of  $G_c$  values while using displacement-based equations for  $G_c$ . Hence, as shown in Figure 4-9, the  $G_c$  values predicted using thin plate theories (small and large deflections), (Equations (4.9) and (4.14)), were higher compared with the  $G_c$  values predicted using thick plate theory (Equation (4.17)).

Also, the transverse strains in the coating are higher for smaller values of debond radii ( $a$ ) i.e. smaller debonds. Hence, the resulting error in the  $G_c$  values predicted using thin plate theories is much higher for smaller debond sizes since the higher transverse strains are not taken into account. Thus, as shown in Figure 4-6, Figure 4-7 and Figure 4-9, the  $G_c$  values predicted using thin plate theories (small and large deflections), were higher for smaller debond radii ( $a$ ).

Lastly, small deflection theory neglects the stretching deformation of the coating. As the debond grows in size, the in-plane stretching deformation of the coating increases, thus the  $G_c$  values are under-predicted for larger debond sizes. Hence, as shown in Figure

4-9, the  $G_c$  values predicted using thin plate – small deflection formation decreased with increasing debond radii ( $a$ ). The large deflection theory takes into account the in-plane stretching deformation and hence for higher debond sizes predicts higher  $G_c$  values compared with small deflection theory. Thus, as shown in Figure 4-9, the  $G_c$  values predicted using the thin plate – large deflection formulation (Equation (4.14)) and the thick plate – large deflection formulation ((4.17)), gradually increase for increasing debond sizes.

To summarize, the thick plate – large deflection formulation takes into account both the stretching deformation (due to large deflection) and transverse strains (due to thick plate) and thus predict lower  $G_c$  values (as shown in Figure 4-8 and Figure 4-9) compared with thin plate theories that show a gradual increase with increasing debond size.

It was mentioned earlier that the correction factor  $C$  given by Equation (4.16) was based on an empirical approximation without any theoretical foundation. Also, the analytical solution used in Equation (4.17) was obtained using a shaft – loaded circular blister approximation. However, as discussed in Chapter 6, compared with thin plate formulations, the  $G_c$  values predicted by the thick plate – large deflection formulation were the closest to  $G_c$  values obtained using finite element simulations (contact interaction analysis) in Chapter 5. Also, as shown earlier the deformation of the coating was in the domain of large deflection and thick plate theory. Therefore, it can be concluded that the  $G_c$  values predicted in Figure 4-8 and Figure 4-9 using thick plate – large deflection formulation were the best estimate for the interfacial fracture energy of the epoxy coating (70  $\mu\text{m}$ )/Si system used as the sample system in the present work. The  $G_c$  values increase with increasing debond sizes, which would indicate that the energy required to drive the crack increases as the debond grows in size and the crack front moves further away from the free edge of the coating.

### 4.3 Curvature Method

The curvature method provides an alternate method of estimating the interfacial fracture energy of an adhesive system by using the local curvature at the crack tip. This approach was first developed by Obreimoff [5] using elementary beam theory formulation and used to estimate the cohesive strength of freshly split mica foils. Goussev has extended this approach, using a linear plate bending formulation, to calculate the interfacial fracture energy for a blister test geometry [6] and a double cantilever beam geometry [7]. The pressurized blister test experiments were conducted by Goussev [6] using two commercial polymer films bonded to polymethylmethacrylate (PMMA) and polytetrafluoroethylene (PTFE) substrates and the blister profile was measured experimentally using a scanning capacitance microscope. Based on the approach developed in [5-7], the following analysis is presented.

#### 4.3.1 Theory

For a thin circular plate with radius  $a$  and thickness  $h$ , undergoing small elastic deflections, the circumferential bending moment in a polar coordinate system is given as [1]:

$$M_{rr} = D \left( \frac{d^2 z}{dr^2} + \frac{\nu}{r} \frac{dz}{dr} \right) \quad r \leq a \quad (4.19)$$

where  $z$  is the out-of-plane deflection of the plate and  $r$  is distance from the center of the plate,  $D$  is the flexural rigidity of the plate and  $\nu$  is the Poisson's ratio of the plate. For a homogenous material, the flexural rigidity is given as:

$$D = \frac{Eh^3}{12(1-\nu^2)} \quad (4.20)$$

where  $E$  is the elastic modulus of the plate. If the plate is assumed as clamped at the edges, the following boundary conditions apply:

$$z|_{r=a} = 0 \quad \& \quad \left. \frac{dz}{dr} \right|_{r=a} = 0 \quad (4.21)$$

Thus, near the edge of the plate ( $r \approx a$ ), using Equations (4.19) and (4.21), the circumferential bending moment can be written as:

$$M_{rr} = D \left( \frac{d^2 z}{dr^2} \right) \quad (4.22)$$

Let  $\tilde{r}$  be the distance from the edge of the plate defined as:

$$\tilde{r} = a - r \quad (4.23)$$

Thus, using Equation (4.23), Equation (4.22) for the circumferential bending moment in a clamped circular plate can be re-written in terms of  $\tilde{r}$  as:

$$M_{rr} = D \left( \frac{d^2 z}{d\tilde{r}^2} \right) \quad (4.24)$$

Now, consider the debonded layer of a thin adhesive coating of thickness  $h$  on a substrate having unit width as shown in Figure 4-10, where  $\tilde{r}$  is the distance measured from the crack tip. The coating is bonded ahead of the crack tip, hence at the crack tip ( $\tilde{r} = 0$ ), a clamped type boundary condition can be assumed, thus

$$z|_{\tilde{r}=0} = 0 \quad \& \quad \left. \frac{dz}{d\tilde{r}} \right|_{\tilde{r}=0} = 0 \quad (4.25)$$

It is assumed that the debonded coating can be modeled as a thin plate. Although it was shown in Section 4.2.2 that the deformation of the coating in the probe test was in the domain of thick plate formulation, closed-form analytical solutions cannot be obtained for thick plates. Hence, using thin plate theory for small deflections, the circumferential bending moment in the debonded region near the crack tip is given by Equation (4.24) as:

$$M_{rr} = D \left( \frac{d^2 z}{d\tilde{r}^2} \right) = D\kappa(\tilde{r}) \quad (4.26)$$

where  $D$  is the flexural rigidity of the coating.  $\kappa(\tilde{r})$  is defined as the curvature and at the crack tip ( $\tilde{r} = 0$ ) is given as (using Equation (4.25)):

$$\kappa(\tilde{r} = 0) = \frac{\left( \frac{d^2 z}{d\tilde{r}^2} \right)}{\left[ 1 + \left( \frac{dz}{d\tilde{r}} \right)^2 \right]^{3/2}} = \left( \frac{d^2 z}{d\tilde{r}^2} \right) \quad (4.27)$$

The displacement profile of the debonded adhesive layer can be approximated near the crack tip region using a Taylor series expansion at  $\tilde{r} = 0$  as [8]:

$$z(\tilde{r}) = z|_{\tilde{r}=0} + \tilde{r} \left. \frac{dz}{d\tilde{r}} \right|_{\tilde{r}=0} + \frac{1}{2} \tilde{r}^2 \left. \frac{d^2 z}{d\tilde{r}^2} \right|_{\tilde{r}=0} + O(\tilde{r}^3) \quad \tilde{r} \geq 0 \quad (4.28)$$

Using the clamped boundary conditions (Equation (4.25)), Equation (4.28) can be written as:

$$z \approx \frac{1}{2} \left( \left. \frac{d^2 z}{d\tilde{r}^2} \right|_{\tilde{r}=0} \right) \tilde{r}^2 = \frac{1}{2} \kappa(0) \tilde{r}^2 \quad \tilde{r} \geq 0 \quad (4.29)$$

where  $\kappa(0)$  is the curvature at the crack tip ( $\tilde{r} = 0$ ).

At the crack tip, the maximum bending moment,  $M_{rr}$  must be equal to the reaction moment, which is itself a direct physical characteristic of the adhesion between the two surfaces. For an infinitesimal crack increment,  $d\tilde{r}$  in the debonded coating having unit width (Figure 4-10), the incremental work done per unit incremental area ( $dA = 1 \cdot d\tilde{r}$ ) by the bending moment  $M_{rr}$  against adhesion is given as:

$$\delta W_{bending} = \frac{1}{dA} M_{rr} d\phi = D\kappa(0) \frac{d\phi}{d\tilde{r}} = D(\kappa(0))^2 \quad (4.30)$$

where  $\phi$  is the angle between the tangent at the point of application of moment  $M_{rr}$  and the  $\tilde{r}$ -axis and using Equation (4.29) is given as:

$$\phi = \frac{dz}{d\tilde{r}} = \kappa(0) \cdot \tilde{r} \quad \Rightarrow \quad d\phi = \kappa(0) d\tilde{r} \quad (4.31)$$

As discussed earlier in Section 4.2.1.2, since the coating is bonded only at the bottom layer, in-plane strains due to elastic stretching deformation may arise at the crack tip through the thickness of the coating. The incremental work done per unit incremental area due to elastic stretching at the crack tip is given as [1, 2]:

$$\delta W_{stretching} = \frac{Eh}{2(1-\nu^2)} (\varepsilon_{rr}(0))^2 = \frac{Eh}{2(1-\nu^2)} \left( \left. \frac{du}{d\tilde{r}} \right|_{\tilde{r}=0} \right)^2 \quad (4.32)$$

where  $\varepsilon_{rr}(0)$  is the in-plane radial strain in the coating mid-plane at the crack tip ( $\tilde{r} = 0$ ). For small strain theory [2],  $\varepsilon_{rr}(0)$  is defined in terms of radial displacement ( $u$ ) as:

$$\varepsilon_{rr}(0) = \left. \frac{du}{d\tilde{r}} \right|_{\tilde{r}=0} \quad (4.33)$$

The change in elastic energy stored per unit debonded area ( $A = 1.\tilde{r}$ ) by the debonded coating having unit width can be calculated using Equations (4.26) and (4.31) as:

$$\delta U_E = \frac{1}{A} \int_0^\phi M_{\tilde{r}\tilde{r}} d\phi = \frac{1}{\tilde{r}} \int_0^\phi D\kappa(0) d\phi = \frac{1}{\tilde{r}} \int_0^\phi \frac{D\phi}{\tilde{r}} d\phi = \frac{1}{\tilde{r}} \frac{D\phi^2}{2\tilde{r}} = \frac{1}{2} D(\kappa(0))^2 \quad (4.34)$$

Assuming no far field dissipation (inelastic deformation), the following energy balance condition can be written:

$$\delta W_{bending} + \delta W_{stretching} = \delta U_E + \delta S \quad (4.35)$$

where  $\delta S$  is the change in surface energy used to drive the interfacial crack by unit surface area. For a stationary crack,  $G_c = \delta S$ , the interfacial fracture energy is thus given as:

$$G_c = \frac{1}{2} \left[ D(\kappa(0))^2 + \frac{Eh}{1-\nu^2} (\varepsilon_{rr}(0))^2 \right] \quad (4.36)$$

As discussed in Chapter 3, the out-of-plane deflection ( $z$ ) of the debonded coating was measured using the WYKO<sup>®</sup> optical profiler. However, using this experimental technique the in-plane deflection ( $u$ ), and thereby the in-plane radial strain ( $\varepsilon_{rr}$ ) cannot be measured. Hence, in the present analysis the second term in Equation (4.36) corresponding to stretching deformation was ignored. It should be noted that ignoring the stretching component in Equation (4.36), would invariably lead to an under-estimation of interfacial fracture energy ( $G_c$ ) using the curvature method. The final expression used for calculating interfacial fracture energy ( $G_c$ ) was given as:

$$G_c = \frac{1}{2} D(\kappa(0))^2 = \frac{1}{2} D \left( \left. \frac{d^2 z}{d\tilde{r}^2} \right|_{\tilde{r}=0} \right)^2 \quad (4.37)$$

### 4.3.2 Implementation

The probe test experiments were conducted under a WYKO<sup>®</sup> optical profiler NT2000<sup>™</sup>, as described in Chapter 3. Using the WYKO<sup>®</sup> profiler, the three dimensional surface topography of the debonded adhesive coating was measured experimentally for different debond sizes. Each measurement dataset was comprised of (x, y, z) values for every point on the surface of the adhesive layer for a particular debond size. The measurements were obtained for five different debonds created on the specimen; for each debond the measurements were obtained for probe penetration distances of 100, 150, 200, 250 and 300 microns. A typical debond surface topography obtained is shown in Figure 4-11.

The experimental data was pre-processed using the WYKO<sup>®</sup> Vision32<sup>®</sup> (version 2.210) software. Firstly, a correction was applied to the data to remove linear tilt from the surface measurements. This term was removed since the WYKO<sup>®</sup> profiler system and the sample always have some inherent tilt. The data was then smoothed using a built-in median filter to remove noisy or spiky data points, and then cropped to select only the region around the crack front. Finally, the processed data was exported and saved in ASCII format so that it could be analyzed by a MATLAB<sup>®</sup> code.

A MATLAB<sup>®</sup> code (Appendix A) was developed to analyze the WYKO<sup>®</sup> measurement data and compute the interfacial fracture energy, using the approach outlined in Section 4.3.1. Using this code, the (x, y, z) data was read from the exported ASCII data file. The experimental data was in a uniform x – y grid format. The x – y points at which no z – value is measured were ignored, these points appeared in black in the surface topography image (Figure 4-12). The data points that form the crack front of the debond were located using the following condition:

At the crack front point:  $z > \text{threshold value} (\sim 2 \text{ micron})$

At the nearest neighboring point:  $z < \text{threshold value} (\sim 2 \text{ micron})$

Ideally, the threshold value should be zero, but due to noise in the experimentally measured z - data, the typical threshold value was taken as between 1.5 micron and 2 micron, depending on the noise amplitude in the particular dataset. The data points for the

---

<sup>®</sup> MATLAB is a registered trademark of The Mathworks, Inc.

experimental crack front were then transformed from the Cartesian ( $x - y$ ) coordinate system to a polar ( $r-\theta$ ) coordinate system and the following polynomial equation was fitted to the transformed crack front coordinates:

$$r(\theta) = c_9\theta^9 + c_8\theta^8 + \dots + c_1\theta + c_0 \quad (4.38)$$

where  $r$  and  $\theta$  are as shown in Figure 4-13 for a typical crack front. Equation (4.38) is a 9<sup>th</sup> order polynomial equation and was found to be a sufficiently good analytical fit to the experimentally measured crack front. Figure 4-14 shows a typical debond surface topography, the corresponding experimental crack front, and the polynomial fit (Equation (4.38)) applied to analytically define the crack front.

From the experimental dataset, the data points along radial directions of the crack front ( $-45^\circ \leq \theta \leq 45^\circ$ ) were isolated (Figure 4-13). As discussed in Chapter 3, a cropped image of the debond surface topography around the center of the crack front was obtained for large size debonds (Figure 4-12). Due to this reason, only the portion of the crack front lying in the range  $-45^\circ \leq \theta \leq 45^\circ$  was considered. The data points ( $x_0, y_0$ ) which lie along a particular value of  $\theta$  satisfy the following condition:

$$\left| \frac{Ax_0 + By_0 + C}{\sqrt{A^2 + B^2}} \right| < 2 \text{ micron} \quad (4.39)$$

where  $Ax + By + C = 0$  is the equation of the line from the center along the  $\theta$  - direction. The points isolated using this condition lie in a narrow band (of width 4 microns) in the  $\theta$ - direction, shown as the dotted region in Figure 4-13.

Also, 50% of the debond area was cropped in order to neglect data points far away from the crack front region. The un-cropped region is shown as a shaded region in Figure 4-13. The data points along  $\theta$ -direction were transformed from the Cartesian ( $x-y-z$ ) coordinate system to a polar ( $\tilde{r}-z$ ) coordinate system, where  $\tilde{r}$  is the radial distance of the data point from the crack front along the  $\theta$ -direction. Thus, the displacement profiles of the debonded coating near the crack front along different  $\theta$ -directions were obtained in terms of  $z$  vs.  $\tilde{r}$  (Figure 4-13).

Using a Taylor series expansion, the displacement profile of the coating can be approximated near the crack front region as:

$$z(\tilde{r}) = \tilde{r} \frac{dz}{d\tilde{r}} \Big|_{\tilde{r} \approx 0} + \frac{1}{2} \tilde{r}^2 \frac{d^2z}{d\tilde{r}^2} \Big|_{\tilde{r} \approx 0} = \tilde{r}\theta + \frac{1}{2} \kappa \tilde{r}^2 \quad \tilde{r} \geq 0 \quad (4.40)$$

where  $\kappa$  is the curvature of the coating near the crack tip and  $\theta$  is the slope of the coating near the crack tip. Equation (4.40) assumes that the displacement  $z = 0$  at  $\tilde{r} = 0$ , however the slope  $\theta$  may not be zero. This was assumed since there might be an error in the numerically located crack tip and the actual crack tip due noise in the experimental data. Thus, the  $z$  vs.  $\tilde{r}$  displacement profile may be offset by a small distance from the actual tip. Taking this factor into account, Equation (4.40) was fitted to the  $z$  vs.  $\tilde{r}$  displacement profile dataset, to evaluate the curvature at the crack tip,  $\kappa(0)$ . Figure 4-15 shows a typical  $z$  vs.  $\tilde{r}$  displacement profile and polynomial fit (Equation (4.40)) applied to analytically define the profile. Finally, using Equation (4.37) the interfacial fracture energy ( $G_c$ ) was calculated for this dataset.

### 4.3.3 Results and discussion

The interfacial fracture energies,  $G_c$  along the crack front for  $-45^\circ \leq \theta \leq 45^\circ$  are shown for debonds #1, #2, #3, #4, #5 in Figure 4-16, Figure 4-17, Figure 4-18, Figure 4-19 and Figure 4-20, respectively. The values are shown for different debond sizes, with probe penetration distances ( $\delta$ ) of 100, 150, 200, 250 and 300 microns. It was observed that for probe penetration distances of 100 and 150 micron, the  $G_c$  values are approximately constant along the crack front. However, for higher values of  $\delta = 200, 250, 300$  micron,  $G_c$  values obtained along the crack front were quite erratic. This was because, as noted in Chapter 3, with increasing debond size (i.e. increasing  $\delta$  values), the overall surface gradient of the debond increases, thus increasing the noise and bad data points in the experimental surface topography data due to limits of the WYKO<sup>®</sup> optical profiler. Also, as discussed earlier in Section 4.2.2, the stretching deformation of the coating increases with increase in debond size. Thus, the error in the predicted  $G_c$  values increases for higher  $\delta$  values since the work done by the stretching deformation was ignored. In addition to stretching deformation, the curvature method was based on thin plate theory, hence the transverse strains in the coating were also neglected. However, it is believed that the transverse strains near the crack front region may be negligible and

hence thin plate theory can be adequately used to analyze the deformations near the debond crack front region.

Figure 4-21 shows the  $G_c$  values averaged around the center of the crack front ( $-5^\circ \leq \theta \leq 5^\circ$ ) as a function of probe penetration distance ( $\delta$ ). It was observed that  $G_c$  values increase with increasing probe penetration distance ( $\delta$ ) i.e. increasing debond size. This would indicate that the energy required to drive the crack increases as the debond grows in size and the crack front moves further away from the free edge of the coating. However, as mentioned earlier in Section 4.3.1, the work done by stretching deformation was ignored, hence the  $G_c$  values obtained using Equation (4.37) were under-estimated.

#### 4.4 Summary

Two analytical techniques were used to calculate the interfacial fracture energies ( $G_c$ ) for the debonded coating/Si substrate specimen using experimental data from the probe test. The first approach used a shaft loaded blister approximation for the probe test geometry and using the overall size of the semi-circular debond in terms of debond radius ( $a$ ) obtained using the optical microscope, different plate theory formulations were used to obtain  $G_c$  values. It was shown that deformation of the coating was in the domain of large deflection and thick plate theory and thus the  $G_c$  values predicted using thick plate – large deflection formulation were the best estimate for the interfacial fracture energy ( $G_c$ ). Also, since thin plate – small deflection formulation ignores the stretching deformation in the coating, therefore under-predicts  $G_c$  for higher debond sizes compared with thin plate – large deflection formulation. Also, thin plate theory neglects the transverse strain in the coating and therefore over-predicts  $G_c$  compared with thick plate theory.

The second approach used the surface profile data of the debonded coating obtained around the crack front obtained using the WKYO<sup>®</sup> optical profiler; and by numerically estimating the curvature at the crack tip from the experimental, the  $G_c$  values were calculated. The  $G_c$  values predicted using this approach were under-estimated since

the work done by stretching deformation was ignored. Also, the results were influenced due to noise in the experimental data, however the overall trends showed an increase in  $G_c$  values with increasing debond size.

Although the  $G_c$  values predicted using the two approaches vary considerably from each other, yet both approaches show an increase in  $G_c$  values with increasing debond size. Thus, the energy required to drive the crack increases as the debond grows in size and the crack front moves further away from the free edge of the coating.

## 4.5 Figures

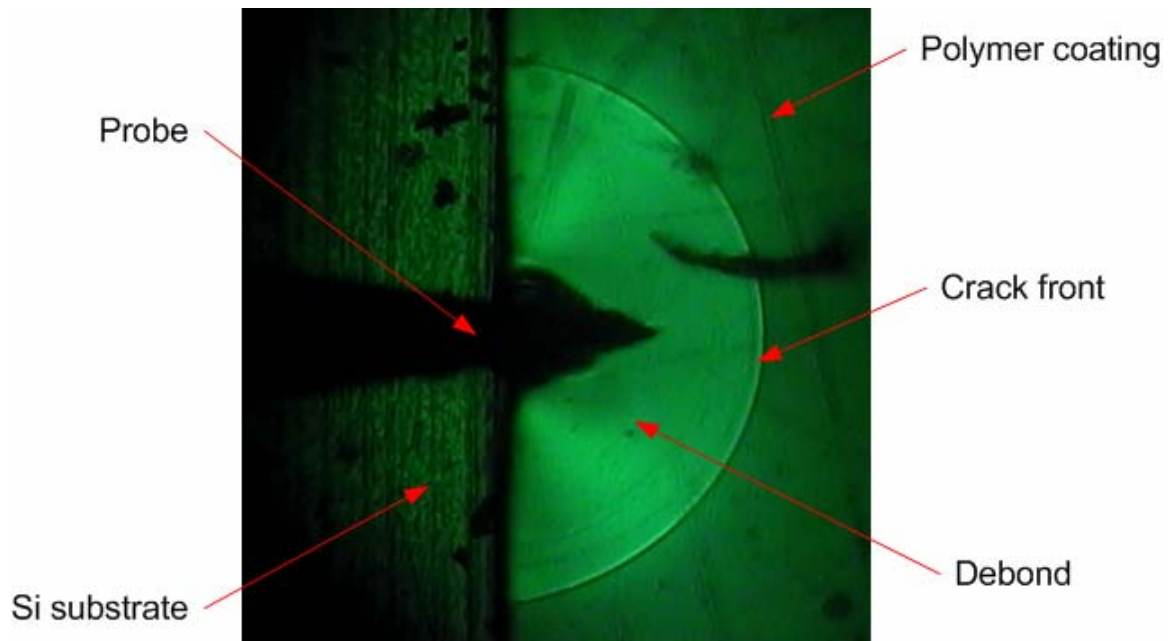


**Figure 4-1 A typical debonding event in the coating for the epoxy coating (70 $\mu\text{m}$ )/Si substrate specimen and using a probe angle of 25° (Scale: 20X)**

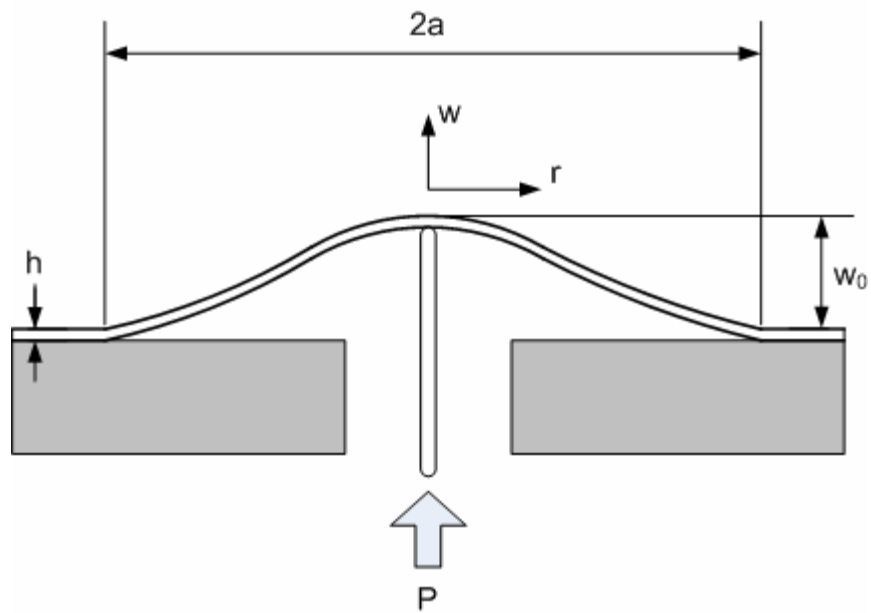


**Figure 4-2 A schematic of a shaft-loaded circular blister configuration**

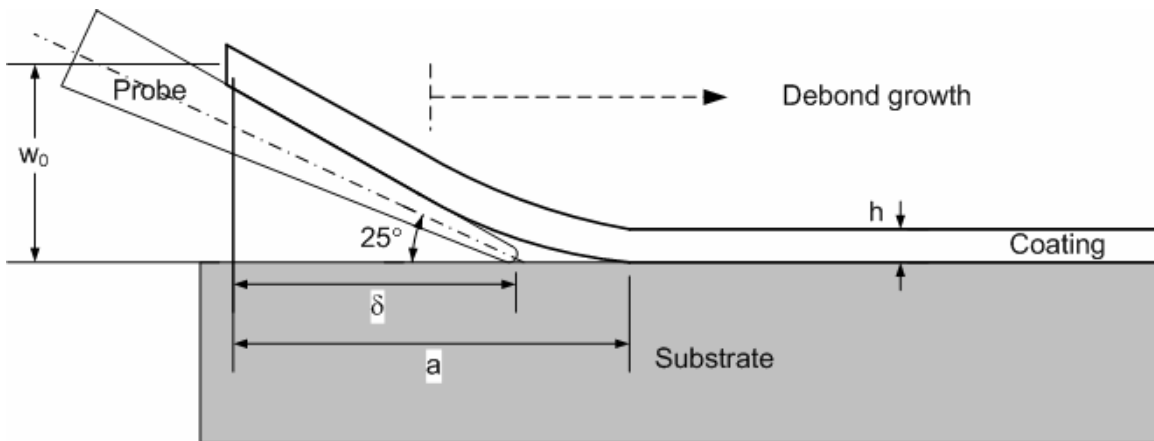


**Figure 4-3 A schematic of the probe test geometry parameters**

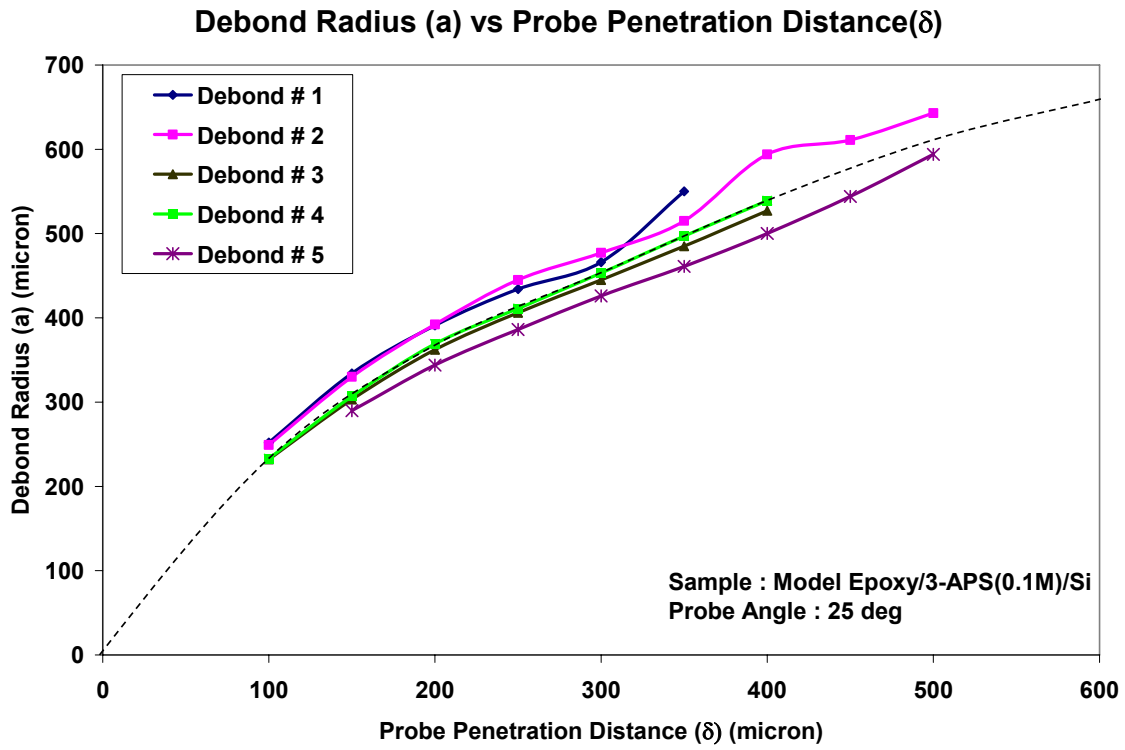


**Figure 4-4 Plots of debond radius (a) along the probe direction as a function of probe penetration distance ( $\delta$ ) for the epoxy coating (70 $\mu$ m)/Si substrate specimen using a probe angle of 25°**

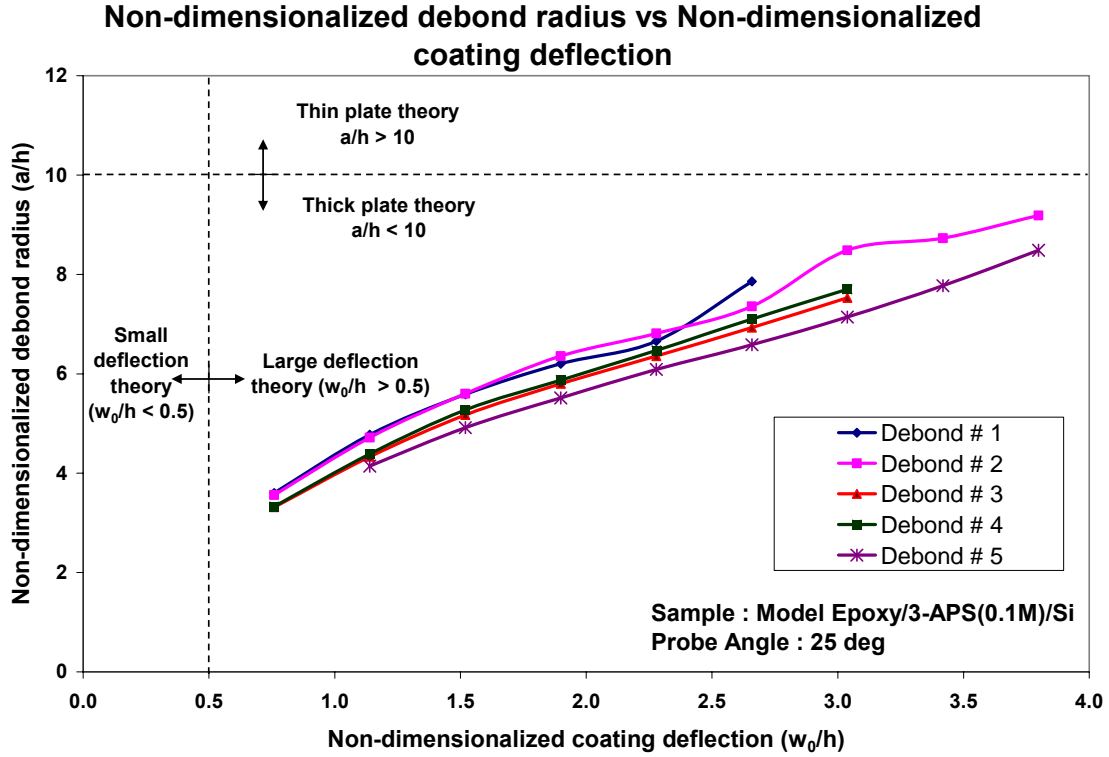


**Figure 4-5** Plots of non-dimensionalized debond radius ( $a/h$ ) as a function of non-dimensionalized coating deflection ( $w_0/h$ ) for the epoxy coating ( $70\mu\text{m}$ )/Si substrate specimen and using a probe angle of  $25^\circ$ ;  $h$  is the coating thickness.

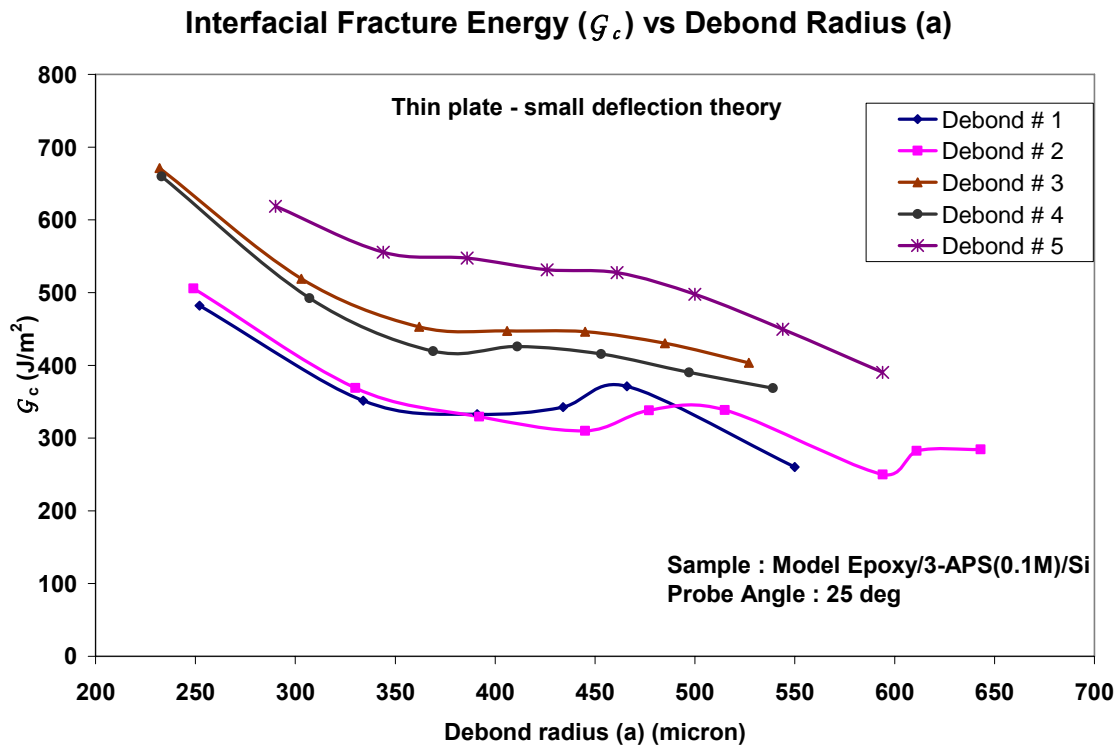


**Figure 4-6 Plots of interfacial fracture energy ( $G_c$ ) vs. probe penetration distance ( $\delta$ ) calculated using thin plate – small deflection theory. The debonds were created using the probe test technique in an epoxy coating(70  $\mu\text{m}$ )/Si substrate specimen and using a probe angle of 25°.**

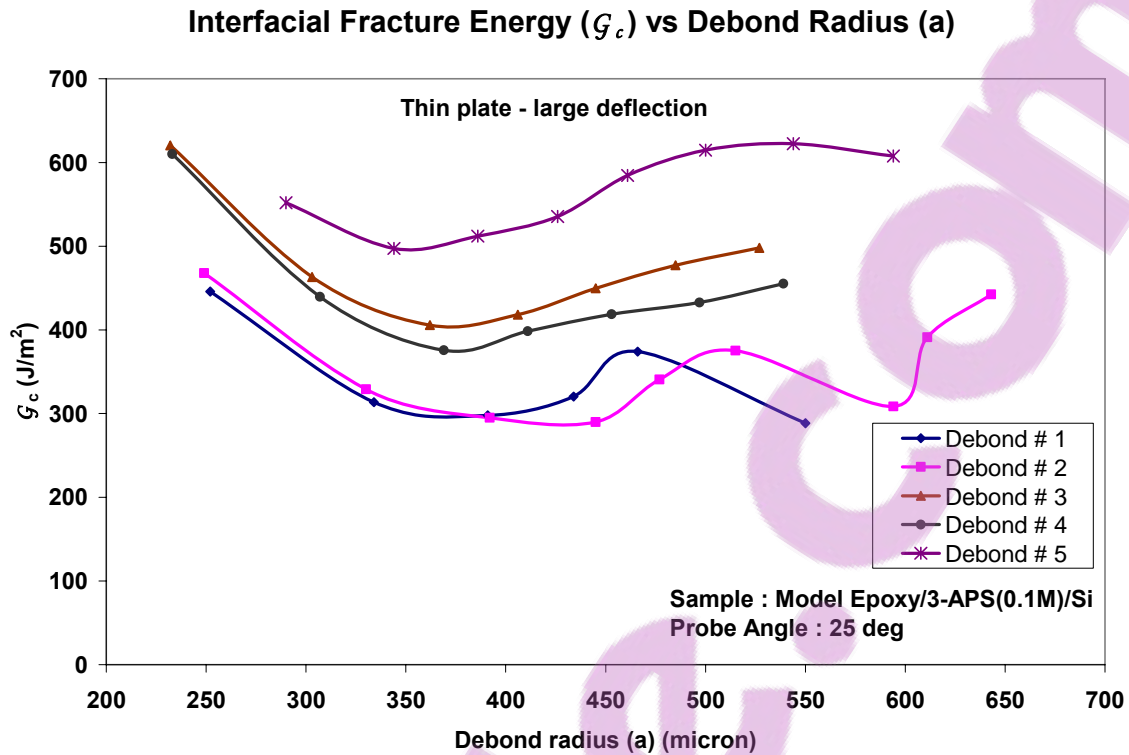


**Figure 4-7 Plots of interfacial fracture energy ( $G_c$ ) vs. probe penetration distance ( $\delta$ ) calculated using thin plate – large deflection theory. The debonds were created using the probe test technique in an epoxy coating(70  $\mu\text{m}$ )/Si substrate specimen and using a probe angle of 25°.**

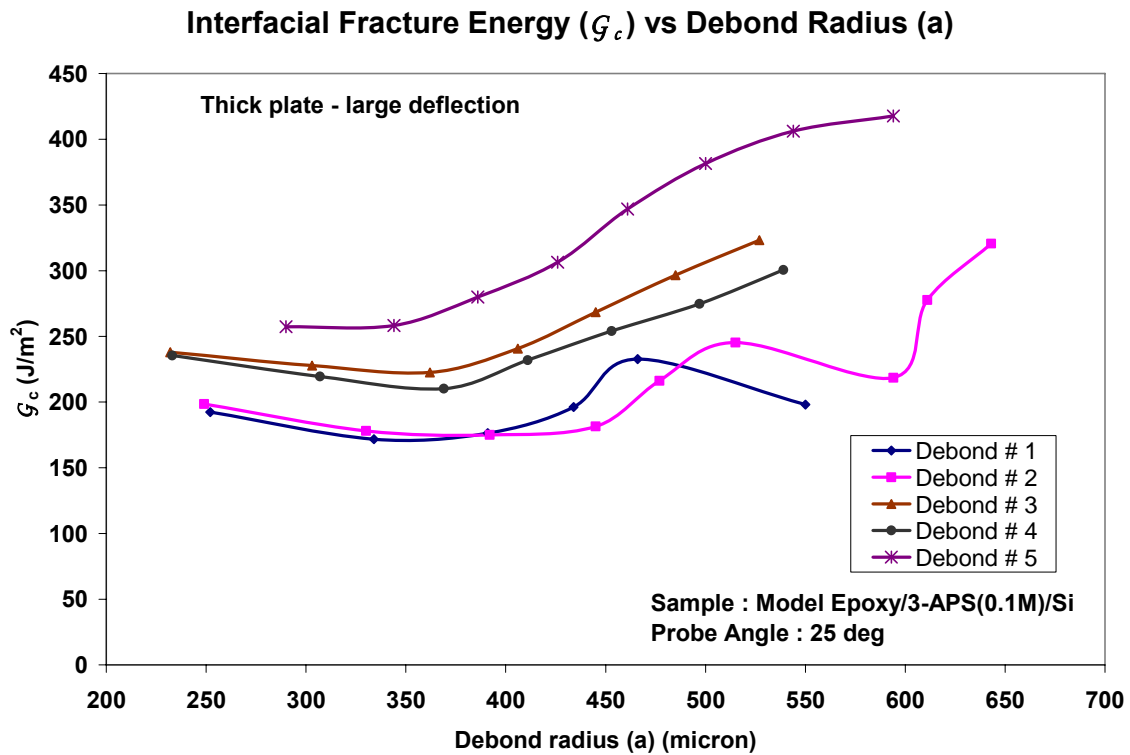


**Figure 4-8 Plots of interfacial fracture energy ( $G_c$ ) vs. probe penetration distance ( $\delta$ ) calculated using thick plate – large deflection theory. The debonds were created using the probe test technique in an epoxy coating(70  $\mu\text{m}$ )/Si substrate specimen and using a probe angle of 25°.**

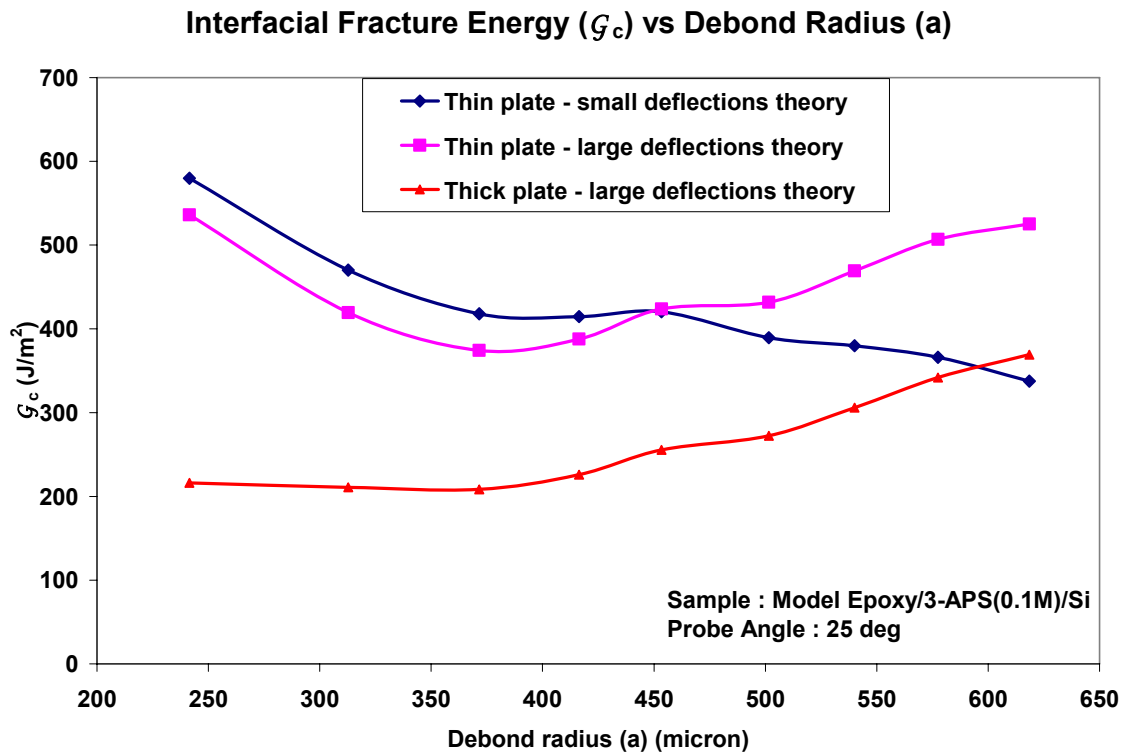


**Figure 4-9 Comparison of interfacial fracture energy ( $G_c$ ) calculated using different plate theory formulations. The debonds were created using the probe test technique in an epoxy coating(70  $\mu\text{m}$ )/Si substrate specimen and using a probe angle of 25°**

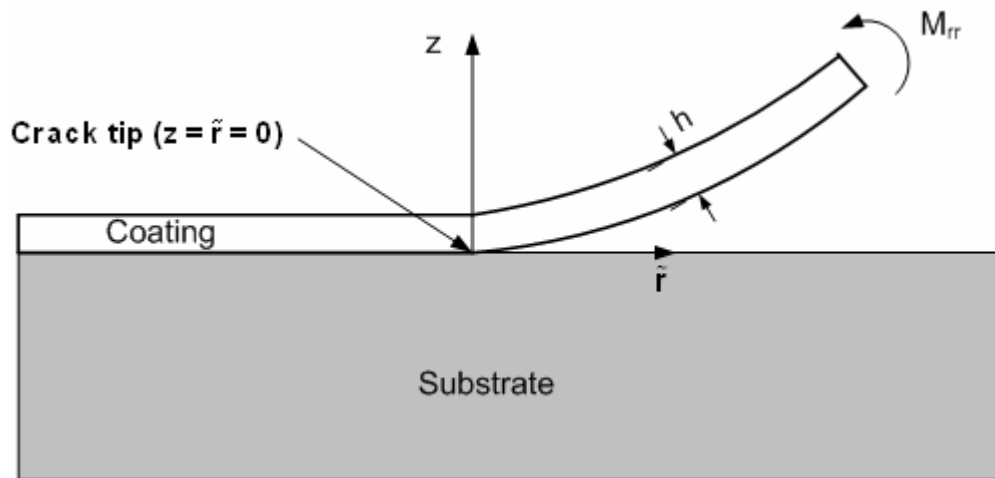


**Figure 4-10** A schematic representation of the debonded layer of a thin adhesive coating on a substrate

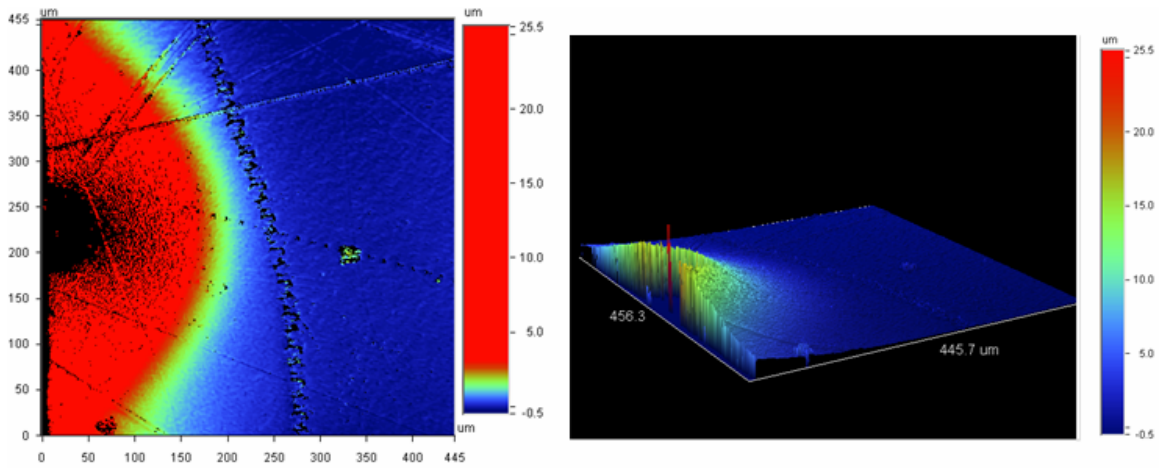


**Figure 4-11** An image of the debond surface topography obtained using WYKO<sup>®</sup> optical profiler for the adhesive coating (70 $\mu\text{m}$ )/Si substrate specimen and a probing angle of 25 $^\circ$

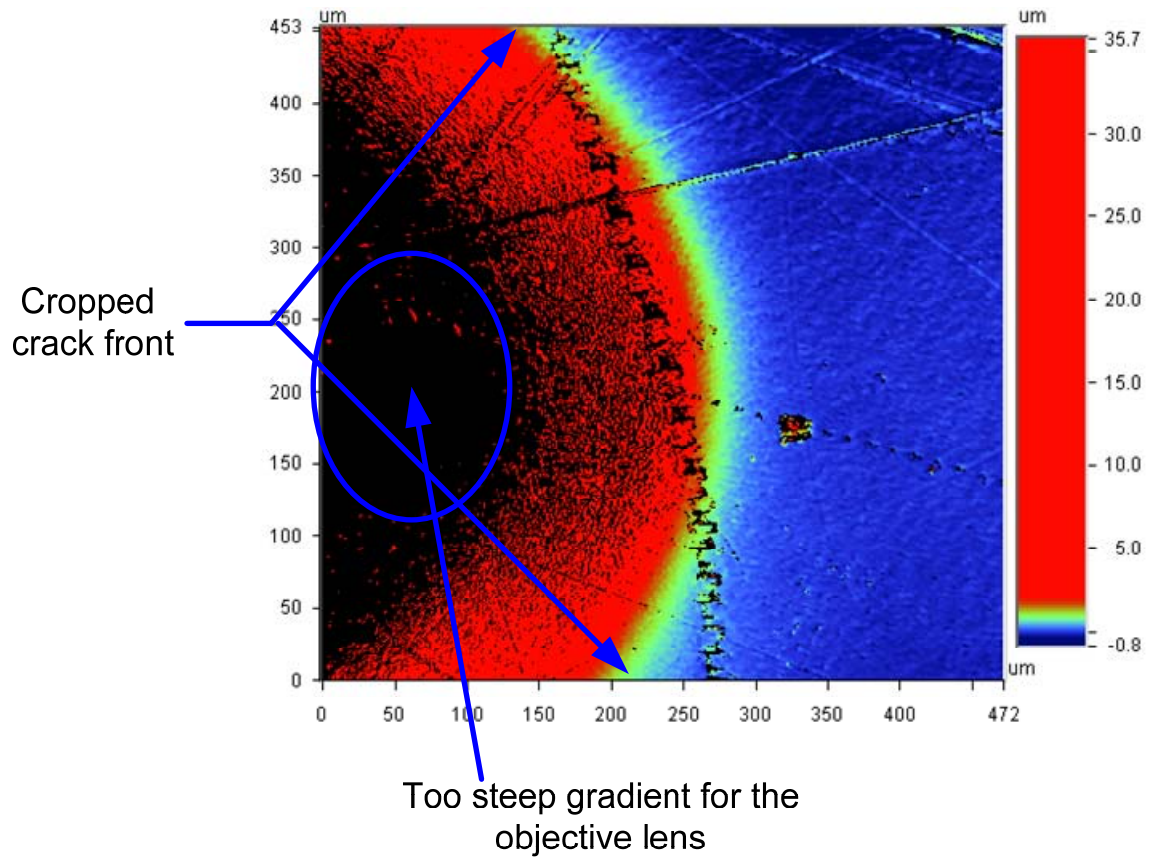


**Figure 4-12** A surface topography image obtained using the WYKO<sup>®</sup> profiler for a debond of larger size than the field of view of the objective lens; bad data points are present in regions of steep gradient and a cropped image of the debond is obtained.

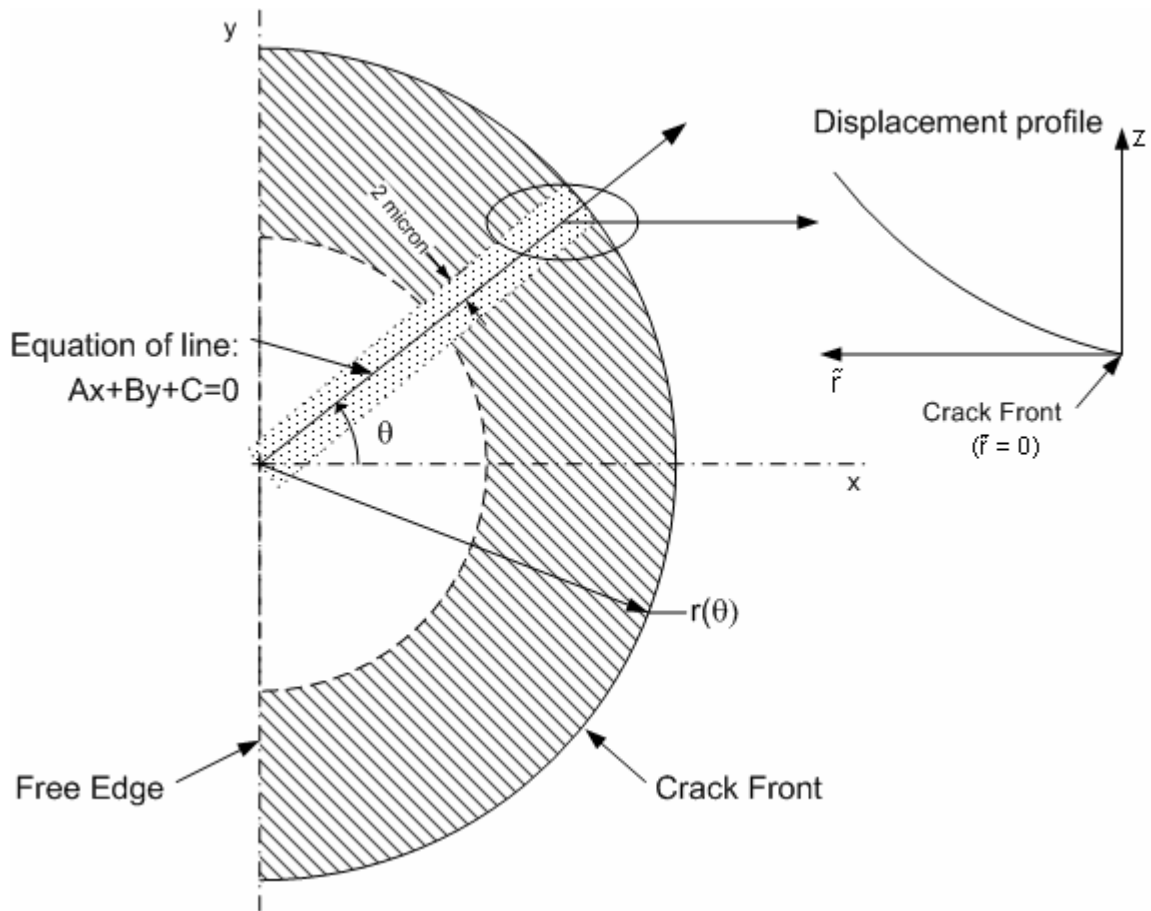


**Figure 4-13 An illustration of the displacement profile along a radial direction of the crack front in a typical debond; 50 % of the debond area away from the crack front region is cropped (the un-cropped region is shown as shaded region).**

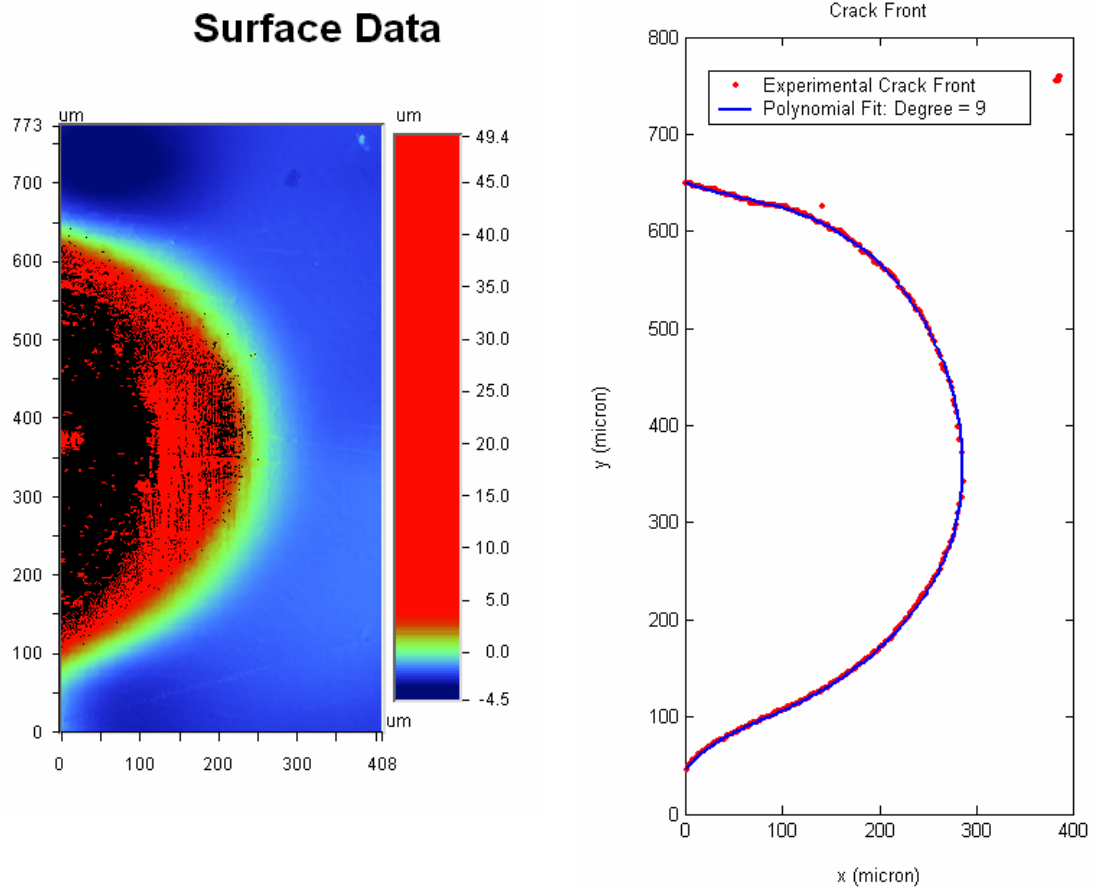


**Figure 4-14 A comparative illustration of the experimental crack front image and the applied analytical polynomial fit, for a debond created using the probe test technique in an epoxy coating(70  $\mu\text{m}$ )/Si substrate specimen and using a probe angle of 25°**

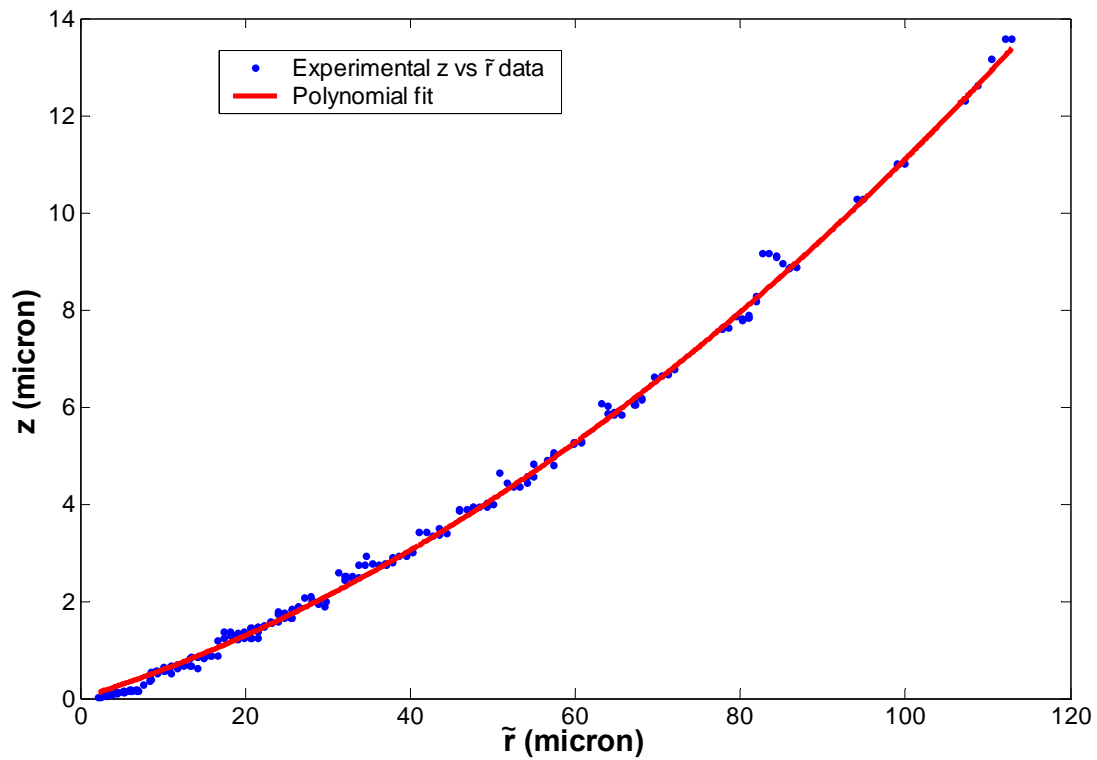


**Figure 4-15** A typical  $z$  vs  $\tilde{r}$  displacement profile for a debond created using the probe test technique in an adhesive coating(70  $\mu\text{m}$ )/Si substrate specimen and a probing angle of 25°

### Interfacial Fracture Energy ( $G_c$ ) along Crack Front

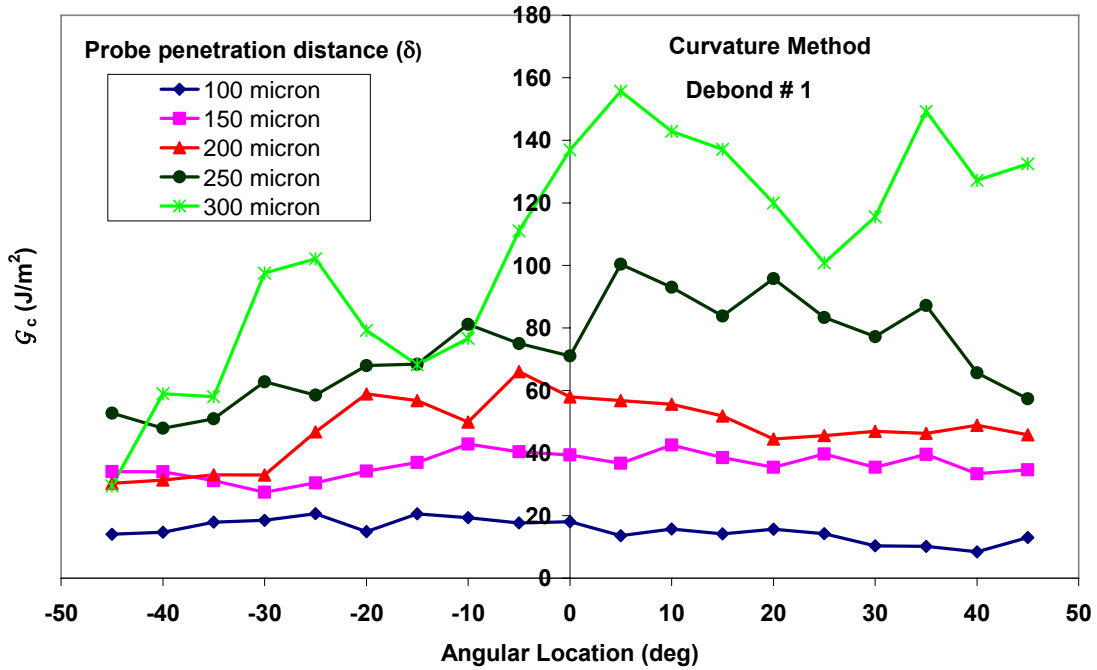


Figure 4-16 Plots of interfacial fracture energy,  $G_c$  along the crack front ( $-45^\circ \leq \theta \leq 45^\circ$ ) of debond # 1 calculated using curvature method. The debond was created using the probe test technique in an epoxy coating( $70 \mu\text{m}$ )/Si substrate specimen and using a probe angle of  $25^\circ$ .

### Interfacial Fracture Energy ( $G_c$ ) along Crack Front

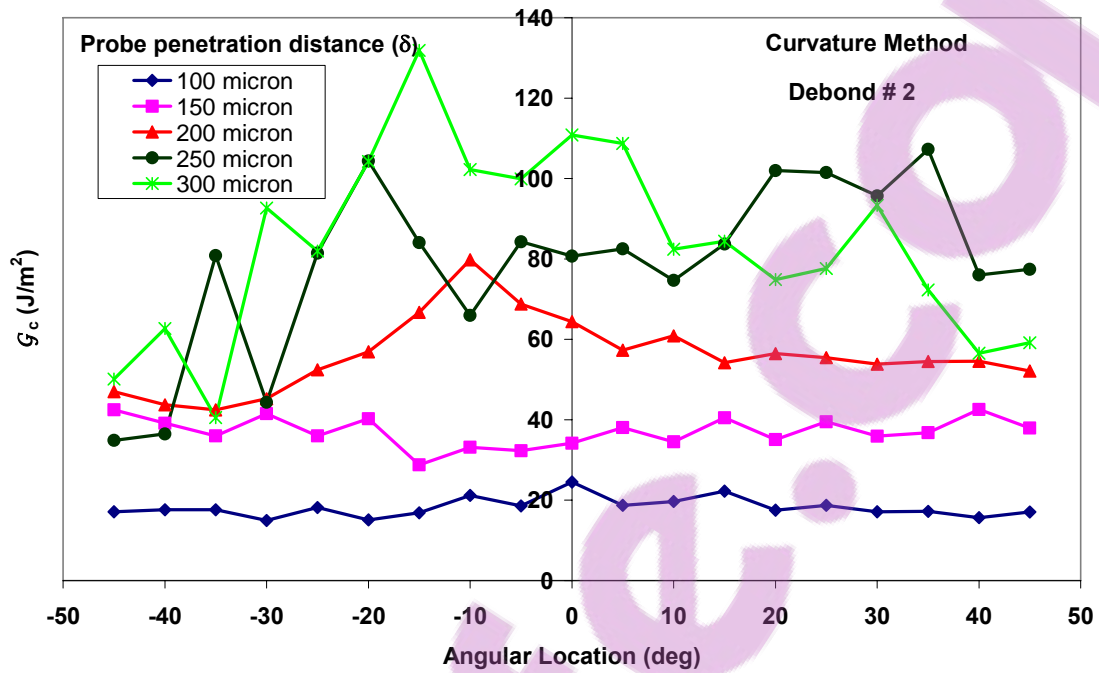
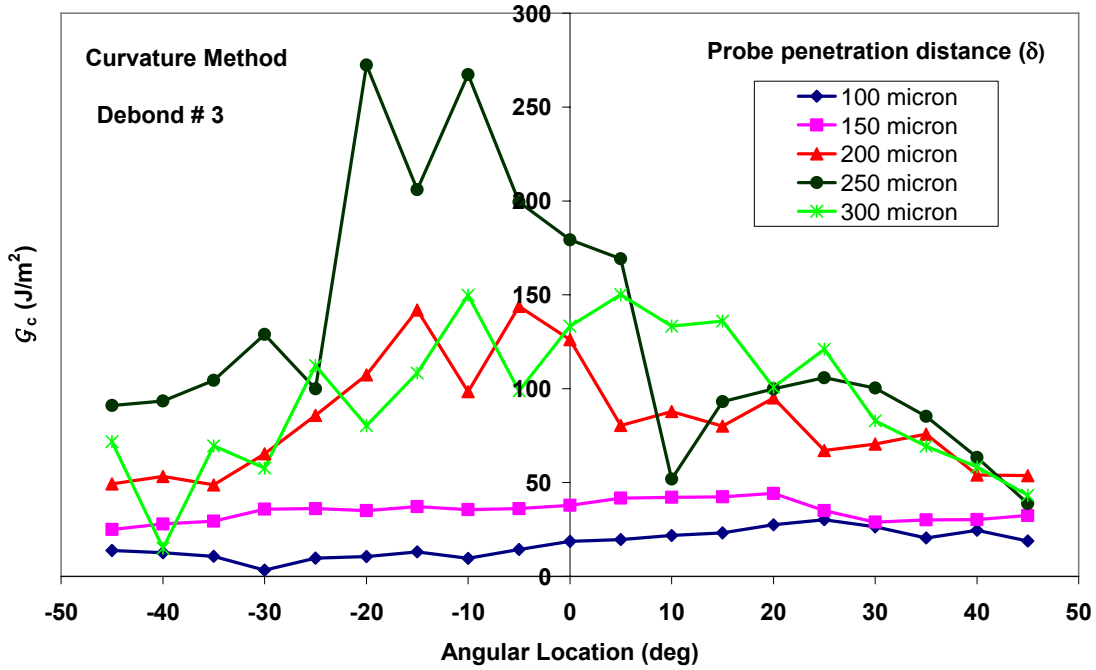


Figure 4-17 Plots of interfacial fracture energy,  $G_c$  along the crack front ( $-45^\circ \leq \theta \leq 45^\circ$ ) of debond # 2 calculated using curvature method. The debond was created using the probe test technique in an epoxy coating(70  $\mu\text{m}$ )/Si substrate specimen and using a probe angle of  $25^\circ$ .

### Interfacial Fracture Energy ( $G_c$ ) along Crack Front



**Figure 4-18** Plots of interfacial fracture energy,  $G_c$  along the crack front ( $-45^\circ \leq \theta \leq 45^\circ$ ) of debond # 3 calculated using curvature method. The debond was created using the probe test technique in an epoxy coating(70  $\mu\text{m}$ )/Si substrate specimen and using a probe angle of  $25^\circ$ .

### Interfacial Fracture Energy ( $G_c$ ) along Crack Front

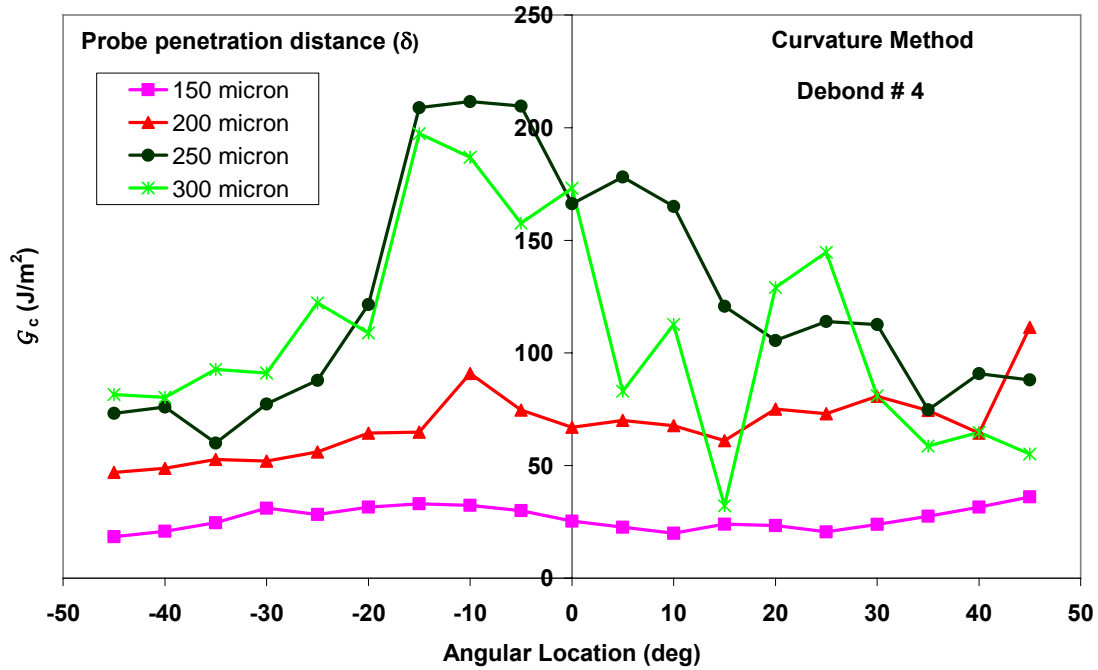


Figure 4-19 Plots of interfacial fracture energy,  $G_c$  along the crack front ( $-45^\circ \leq \theta \leq 45^\circ$ ) of debond # 4 calculated using curvature method. The debond was created using the probe test technique in an epoxy coating(70  $\mu\text{m}$ )/Si substrate specimen and using a probe angle of  $25^\circ$ .

### Interfacial Fracture Energy ( $G_c$ ) along Crack Front

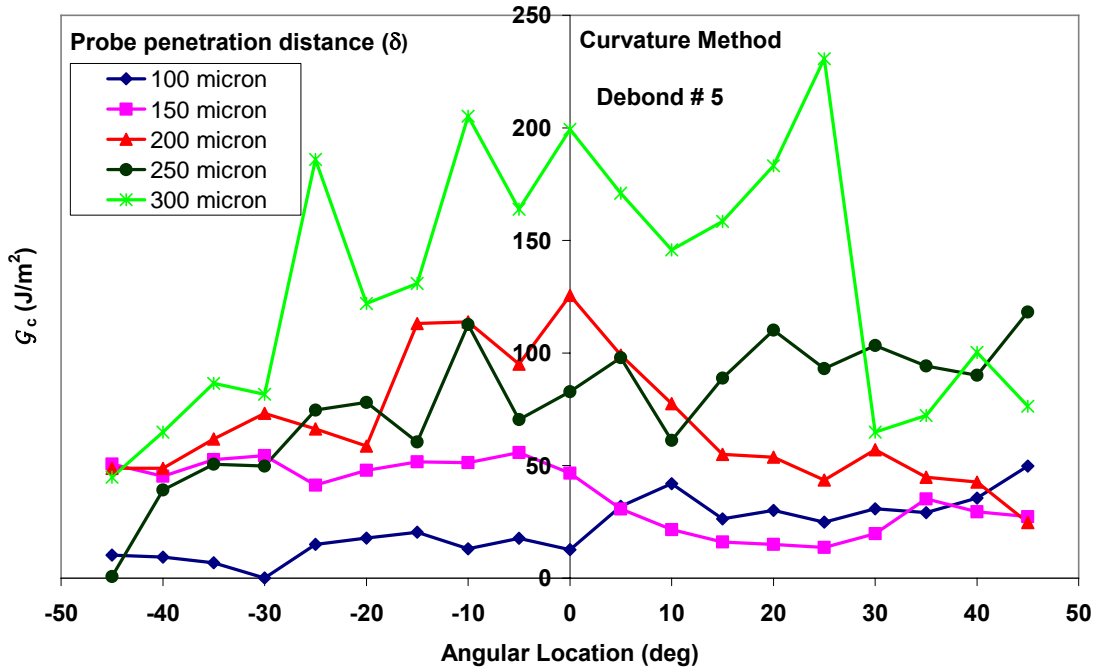


Figure 4-20 Plots of interfacial fracture energy,  $G_c$  along the crack front ( $-45^\circ \leq \theta \leq 45^\circ$ ) of debond # 5 calculated using curvature method. The debond was created using the probe test technique in an epoxy coating( $70 \mu\text{m}$ )/Si substrate specimen and using a probe angle of  $25^\circ$ .

Interfacial fracture energy ( $\mathcal{G}_c$ ) vs. Probe penetration distance

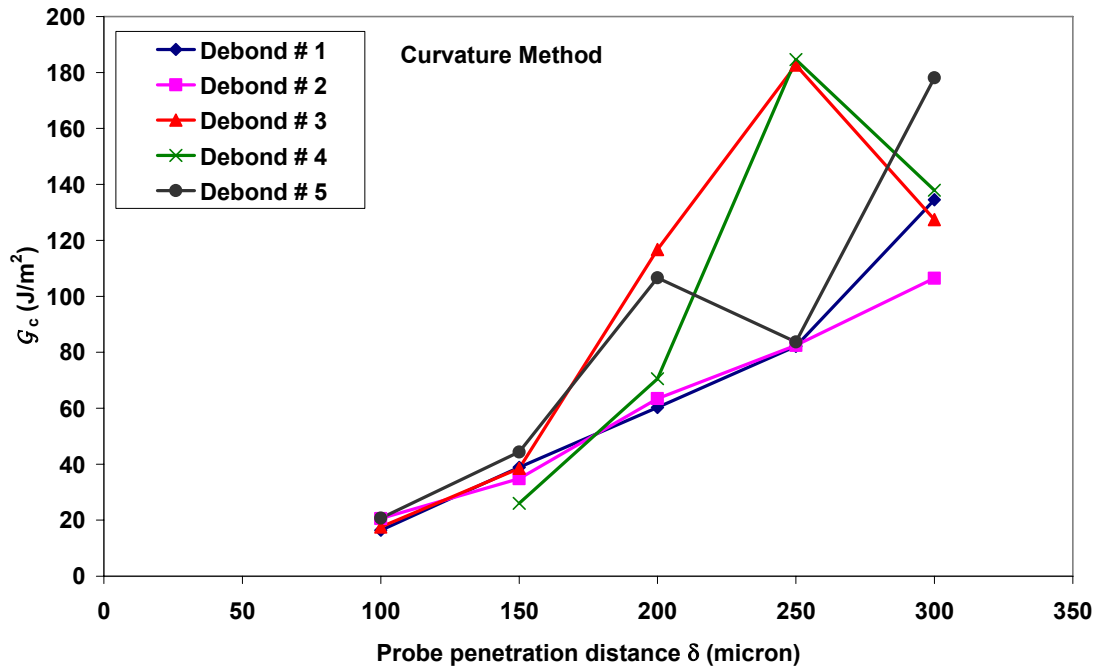


Figure 4-21 Plots of interfacial fracture energy,  $\mathcal{G}_c$  averaged near the center of the crack front ( $-5^\circ \leq \theta \leq 5^\circ$ ) vs. probe penetration distance ( $\delta$ ) calculated using curvature method. The debonds were created using the probe test technique in an epoxy coating(70  $\mu\text{m}$ )/Si substrate specimen and using a probe angle of  $25^\circ$ .

## 4.6 References

1. Timoshenko, S. and S. Woinowsky-Krieger, *Theory of plates and shells*. 2d ed. Engineering societies monographs. 1959, New York,: McGraw-Hill.
2. Boresi, A.P. and R.J. Schmidt, *Advanced mechanics of materials*. 6th ed. 2003, New York: John Wiley & Sons. xiii, 681.
3. Briscoe, B.J. and S.S. Panesar, *The Application of the Blister Test to an Elastomeric Adhesive*. Proceedings of the Royal Society of London Series a-Mathematical Physical and Engineering Sciences, 1991. **433**(1887): p. 23-43.
4. Chia, C.-Y., *Nonlinear analysis of plates*. 1st ed. 1980, New York: McGraw-Hill International Book Co. xiv, 422.
5. Obreimoff, J.W., *The Splitting Strength of Mica*. Proceedings of the Royal Society of London. Series A, Containing Papers of a Mathematical and Physical Character, 1930. **127**(805): p. 290-297.
6. Goussev, O.A., K. Zeman, and U.W. Suter, *Local bending moment as a measure of adhesion: The blister test*. Journal of Adhesion, 1996. **56**(1-4): p. 45-57.
7. Goussev, O.A., P. Richner, and U.W. Suter, *Local bending moment as a measure of adhesion: The cantilever beam test*. Journal of Adhesion, 1999. **69**(1-2): p. 1-12.
8. O'Neil, P.V., *Advanced engineering mathematics*. 5th ed. 2003, Pacific Grove, CA: Thomson Brooks/Cole. xiii, 1236, 82, 9.

## Chapter 5 Numerical Methods

### 5.1 Introduction

This chapter presents finite element techniques used to model the debonded profile of the coating in the probe test method. The test method has been described in detail in Chapter 3. The finite element simulations were conducted using ABAQUS<sup>1</sup>, a commercial finite element analysis software package. The interfacial fracture energy,  $G_c$  (or critical strain energy release rate), was used to provide a quantitative measure of adhesion in the epoxy coating/Si substrate system. The interfacial fracture energy ( $G_c$ ) was calculated at the crack tip of the debond using J – Integral evaluation in ABAQUS/Standard. A discussion of J – integral evaluation in ABAQUS/Standard has been provided in Chapter 2. The following two approaches were used to model the debonded coating:

- i. Displacement field-based finite element model: This approach involved a hybrid numerical – experimental approach applying the experimentally measured z – displacements of the debonded coating directly to the ABAQUS model as boundary conditions.
- ii. Contact interaction analysis: This approach used contact interaction analysis in ABAQUS/Standard to compute the deformed shape of the coating. The contact interaction was defined between the probe tip and the coating; thus the coating was deformed as the probe tip was displaced to create the simulated debond.

### 5.2 Displacement field-based finite element model

#### 5.2.1 Introduction

Using the WYKO<sup>®</sup> NT2000<sup>™</sup> optical profiler, the profile of the debonded coating around the crack front region in the probe test geometry was measured experimentally for different debond sizes, as described in Chapter 3. The measurement dataset provided the z-displacement for each point (x,y) on the surface of debonded

---

<sup>1</sup> ABAQUS and ABAQUS/Standard are registered trademarks of ABAQUS, Inc.

coating. In this method, a three – dimensional finite element model of the coating was constructed using the material parameters ( $E, \nu, h$ ) shown in Table 5-1. The experimentally measured  $z$  – displacements were applied as boundary conditions in the finite element model to accurately simulate the profile of the debonded layer. Thus, this method involved a hybrid numerical – experimental approach. The analysis was conducted using finite element simulations in ABAQUS/Standard.

## 5.2.2 Implementation

The experimental data was pre-processed using the WYKO<sup>®</sup> Vision32<sup>®</sup> (version 2.210) software. Firstly, a correction was applied to the data to remove linear tilt from the surface measurements. This term was removed since the WYKO<sup>®</sup> profiler system and the sample always have some inherent tilt. The data was then smoothed using a built-in median filter to remove noisy or spiky data points and then cropped to select only the region around the crack front. Finally, the processed data was exported and saved in ASCII format so that it could be analyzed using MATLAB<sup>®</sup> software. Two MATLAB<sup>®</sup> codes were developed to analyze the WYKO<sup>®</sup> measurement data and generate an ABAQUS script for finite element simulations, respectively.

Using the first MATLAB<sup>®</sup> code (Appendix B), the ( $x, y, z$ ) data was read from the exported ASCII data file. The experimental data was in a uniformly spaced  $x - y$  grid format. The  $x - y$  points at which no  $z$  – value is measured were ignored, these points appeared in black in the surface topography image (Figure 5-1). The data points that form the crack front of the debond were located using the following condition:

At the point:  $z > \text{threshold value} (\sim 2 \text{ micron})$

At the nearest neighboring point:  $z < \text{threshold value} (\sim 2 \text{ micron})$

Ideally, the threshold value should be zero, but due to noise in the experimentally measured  $z$  - data, the typical threshold value was taken as between 1.5 micron and 2 micron, depending on the noise amplitude in the particular dataset. The data points for the experimental crack front were then transformed from the Cartesian ( $x - y$ ) coordinate

---

<sup>®</sup> MATLAB is a registered trademark of The Mathworks, Inc.

system to a polar ( $r$ - $\theta$ ) coordinate system and the following polynomial equation was fitted to the transformed crack front coordinates:

$$r(\theta) = c_9\theta^9 + c_8\theta^8 + \dots + c_1\theta + c_0 \quad (5.1)$$

where  $r$  and  $\theta$  are as shown in Figure 5-2 for a typical crack front. Equation (5.1) is a 9<sup>th</sup> order polynomial equation and was found to be a sufficiently good fit to the experimentally measured crack front. Figure 5-3 shows a typical debond surface topography, the corresponding experimental crack front and the polynomial fit (Equation (5.1)) applied to analytically define the crack front.

Using the second MATLAB<sup>®</sup> code (Appendix C), an ABAQUS/Standard script was generated to create the model of the debonded profile of the coating. The material parameters ( $E, \nu, h$ ) of the coating are shown in Table 5-1. The shape of the crack front and the  $z$  – displacements of the coating vary for different measurements. Hence, this second MATLAB<sup>®</sup> code was developed to automate the process of defining the ABAQUS model depending on the experimentally measured parameters. A typical ABAQUS script generated using the second MATLAB<sup>®</sup> code is given in Appendix D.

Based on the size of the crack front, a mesh was defined using C3D27 element type in ABAQUS/Standard. The C3D27 element is a second-order, iso-parametric, 27-node, three-dimensional continuum element, as shown in Figure 5-4. The mesh was defined in a radial pattern ahead and behind of the crack front, as shown in Figure 5-5. In order to improve the accuracy of the stress field near the crack front region, the nodes were concentrated more towards the crack front region than far away from it. This was achieved by defining a bias parameter,  $b < 1$ , which is the ratio of adjacent distances between nodes along each line of nodes generated ahead or behind the crack front. The bias parameter,  $b$  was applied at every second interval along the line in order to position the mid-side nodes correctly for use with the second-order element C3D27. Thus, the mid-side nodes lied in the middle of the interval between the corner nodes of the element. For example, as shown in Figure 5-6, for 4 rows of elements behind the crack front, the bias intervals along the line from the crack front node are:

$$L/2b_i^3, 3L/2b_i^3, L/b_i^2, L/b_i^2, L/b_i, L/b_i, L, L.$$

And for 3 rows of elements ahead of the crack, the bias intervals along the line from the crack front node are:

$$L/2b_o^3, 3L/2b_o^3, L/b_o^2, L/b_o^2, L/b_o, L/b_o.$$

The values for bias parameters used were  $b_i = 0.8$  for the nodes behind the crack front,  $b_o = 0.6$  for the nodes ahead the crack front and  $b_n = 0.6$  for the row of nodes normal to the crack front plane.

For a sharp crack, the stress field becomes singular at the crack tip. Assuming small strain analysis, for a linear elastic material, the stress field at the crack tip has a square root singularity given as [1]:

$$\sigma \propto \frac{1}{\sqrt{r}} \quad (5.2)$$

where  $r$  is distance from the crack tip. A more detailed discussion on the stress distribution around a crack tip has been provided in Chapter 2. To obtain a square root singularity at the crack front, quarter-point spacing was used for the nodes next to the crack front. This was accomplished by moving the mid-side nodes of the elements closest to the crack front to  $1/4$  of the distance between the edge nodes [2]. Hence, as shown in Figure 5-6, the first interval from the crack front is  $L/2b_i^3$  and  $L/2b_o^3$  behind and ahead of the crack front, respectively. Quarter-point spacing was used for elements just behind and ahead of the crack front and normal to the crack front plane. The quarter-point spacing approach created a singular stress field based on Equation (5.2) around the crack tip and thus accurately evaluated the  $J$  – integral at the crack front [2].

### 5.2.2.1 Behind the crack front

The experimentally measured  $z$ -displacements were assigned to the corresponding nodes in the wake of the crack front as displacement boundary conditions. The displacement boundary conditions were specified only for nodes on the edges of an element, and not for any of the mid-side nodes, which were left unconstrained. This allowed a uniform strain field to develop within an element. As stated earlier, the experimental data was in a uniformly spaced  $x$ - $y$  grid format. As shown in Figure 5-5, a radial-type mesh was used, thus the location of the nodes did not correspond to experimental  $x$ - $y$  data points at which  $z$ -displacements were measured. A weighted

average technique was thus used to calculate the z-displacement ( $u_z$ ) at the nodal points. For every experimental data-point, the closest nodal position was located. This was accomplished by using the 'dsearchn' function [3] in MATLAB<sup>®</sup>. This function uses a Delaunay triangulation approach [4] to locate the nearest neighboring points from a dataset. If  $p_1, p_2, p_3, \dots, p_n$  are the experimental data-points closest to the nodal position  $n_1$ , the z-displacement ( $u_z$ ) at the node  $n_1$  was calculated as:

$$u_z(n_1) = \frac{z(p_1)d_1 + z(p_2)d_2 + z(p_3)d_3 + \dots + z(p_n)d_n}{d_1 + d_2 + d_3 + \dots + d_n} \quad (5.3)$$

where  $z(p_n)$  is the experimental z-displacements at data-point  $n$  and  $d_n$  is the distance in the x-y plane between the data-point  $p_n$  and nodal position  $n_1$ .

Also, any node for which the z-displacement ( $u_z$ ) was not specified was thus left unconstrained and therefore free to move. Since the finite element model was displacement-based, the same  $u_z$  values were used for nodes through the thickness of the coating to achieve deflection of all the nodes through the thickness of the coating. Thus, this condition assumed that:

$$u_z = u_z(x, y) \quad (5.4)$$

where  $u_x, u_y, u_z$  are the nodal displacements in the x, y, z directions.

From small displacement theory [5], the assumption stated in Equation (5.4) implied that the out-of-plane normal strain component ( $\varepsilon_{zz}$ ) was taken as zero, thus:

$$\varepsilon_{zz} = \frac{\partial u_z}{\partial z} = 0 \quad (5.5)$$

It should be noted that the two out-of-plane shear components ( $\varepsilon_{xz}, \varepsilon_{yz}$ ) as defined in Equation (5.6) were not necessarily zero. Hence, Equation (5.4) assumed a pure bending deformation of the coating.

$$\begin{aligned} \varepsilon_{xz} &= \frac{1}{2} \left( \frac{\partial u_z}{\partial x} + \frac{\partial u_x}{\partial z} \right) \\ \varepsilon_{yz} &= \frac{1}{2} \left( \frac{\partial u_z}{\partial y} + \frac{\partial u_y}{\partial z} \right) \end{aligned} \quad (5.6)$$

The J-integral was evaluated successively for contours over five rings of elements. A strongly varying non-monotonic strain field within this region led to an error in the contour integral definition, commonly known as domain dependence or contour dependence [2]. Thus, in order to improve accuracy of the J – integral evaluation at the crack front, the z-displacements for any nodal position close to the crack front region were ignored. This ensured that a monotonically varying strain field developed near the crack region. The typical width of this band of nodes just behind the crack front, where the z-displacement are ignored, was taken as 10 elements.

### 5.2.2.2 Ahead of the crack front

For the nodes at the crack front and ahead of the crack front on the bottom layer of the coating, a PINNED type boundary condition was used to constrain all displacements to represent the intact adhesion ahead of the crack front. Thus, for nodes lying on the bonded surface of the coating, at and ahead of the crack front,

$$u_x = u_y = u_z = 0 \quad (5.7)$$

where  $u_x, u_y, u_z$  are the nodal displacements in the x, y, z directions.

Using the approach outlined in this section, finite element simulations were conducted using the experimental measurements from four different debonds created on the specimen; for each debond the measurements were collected for probe penetration distances of 100, 150, 200, 250 and 300 microns. A typical deformed profile of the coating obtained using the finite element simulations is shown in Figure 5-7. The J – integral was evaluated at the crack front, using the \*CONTOUR INTEGRAL function in ABAQUS/Standard. The values were evaluated successively over five contours; each contour consisting of a ring of elements completely surrounding the crack tip. The values converged over successive contours, thus only the last (i.e. the 5<sup>th</sup>) contour integral value was used as the interfacial fracture energy ( $G_c$ ).

### 5.2.3 Results and discussion

The interfacial fracture energy ( $G_c$ ) along the crack front for  $-45^\circ \leq \theta \leq 45^\circ$  are shown for debonds #1, #2, #3, #4 in Figure 5-8, Figure 5-9, Figure 5-10 and Figure 5-11 respectively. The values are shown for different debond sizes, with probe penetration

distances ( $\delta$ ) of 100, 150, 200, 250 and 300 microns. These results were obtained using 6,912 elements in the finite element mesh for the coating model.

Figure 5-12 and Figure 5-13 show the results obtained for Debond #1 -  $\delta = 200$  micron, and Debond #1 -  $\delta = 250$  micron, respectively using refined meshes. The  $G_c$  values along the crack front using the coarse mesh of 6,912 elements are nearly the same as those using a more refined mesh. Thus, in order to reduce the computational time in running the finite element simulations, the mesh with 6912 elements was used.

Finally, Figure 5-14 shows the  $G_c$  values averaged around the center of the crack front ( $-5^\circ \leq \theta \leq 5^\circ$ ) as a function of probe penetration distance ( $\delta$ ).

The  $G_c$  values obtained along the crack front using this hybrid numerical – experimental approach were quite erratic. This could be explained by a number of reasons. Firstly, as noted in Chapter 3, with increasing debond size (i.e. increasing  $\delta$  values), the overall surface gradient of the debond increases, thus increasing the noise and bad data points in the experimental surface topography data due to limits of the WYKO<sup>®</sup> optical profiler. Also, any in-plane stretching deformation around the crack front of the debonded coating was not measured using the WYKO<sup>®</sup> optical profiler and therefore may not have been taken into account in the finite element simulation. In conclusion, the error in the  $G_c$  values obtained using this approach is expected to be large and the results shown are not considered to be realistic.

## 5.3 Contact interaction analysis

### 5.3.1 Introduction

As described in Chapter 3, the probe test experiments were also performed on a Nikon UM-2 Measurescope microscope with a digital measuring stage. A typical debonding event as a result of penetration of the probe tip along the coating/Si interface is shown in Figure 5-15. The debond was created using a 1 $\mu$ m tip radius tungsten probe and a probe angle of  $25.0^\circ \pm 1.0$  was used. A semi-circular crack front was observed at the interface of the coating/Si substrate specimen as the probe slid underneath the coating. The size of the debond in terms of the radius of the debond along the probe direction ( $a$ ) was recorded for successive values of probe penetration distances ( $\delta$ ). Figure 5-16 shows the debond radius ( $a$ ) as a function of the probe penetration distance ( $\delta$ ). The debond radius ( $a$ ) values shown in Figure 5-16 were averaged for a particular value of probe penetration distance ( $\delta$ ) over five different debonds created on the coating/Si specimen. The complete  $a$  vs.  $\delta$  data is shown in Figure 3-8 of Chapter 3.

In this method, the penetration of the probe underneath the coating and the subsequent debonding of the coating were simulated in a three-dimensional finite element analysis using surface – based contact interaction simulation between the coating and the conical probe in ABAQUS.

### 5.3.2 An overview of contact interaction analysis in ABAQUS/Standard

ABAQUS/Standard provides a surface-based finite-sliding formulation for modeling the contact interaction between a deformable body and an arbitrarily shaped rigid body that may move during the history being modeled. The contact is defined between two bodies in terms of two surfaces that may interact; these surfaces are called a contact pair (slave/master surface). The order in which the two surfaces are specified is critical because of the manner in which surface interactions are discretized. For each node on the slave surface, ABAQUS/Standard attempts to find the closest point on the master surface of the contact pair, where the master surface's normal passes through the node on the slave surface. The interaction is then discretized between the point on the master

surface and the slave node. Slave surfaces are always attached to deformable bodies or deformable bodies defined as rigid. Analytical and rigid-element-based surfaces are always the master surface in the contact pair. Both surfaces in a contact pair cannot be rigid surfaces with the exception of deformable surfaces defined as rigid.

ABAQUS/Standard defines the contact conditions between two bodies using a strict master-slave algorithm: nodes on one surface (the slave) cannot penetrate the segments that make up the other surface (the master). The algorithm places no restrictions on the master surface, thus it can penetrate the slave surface between slave nodes. A consequence of this strict master-slave formulation is that the slave and master surfaces must be correctly selected to achieve the best possible contact simulation. Thus, in order to achieve better contact, the slave surface should be the more finely meshed surface.

The finite-sliding formulation permits separation and sliding of finite amplitude and arbitrary rotation of the surfaces that may arise. The finite-sliding rigid contact capability is implemented by means of a family of contact elements that ABAQUS automatically generates based on the data associated with the user-specified contact pairs. At each integration point these elements construct a measure of overclosure (penetration of the point on the surface of the deforming body (slave surface) into the rigid surface (master surface)) and measures of relative shear sliding. These kinematic measures are then used, together with appropriate Lagrange multiplier techniques, to introduce surface interaction model based on contact pressure and friction.

The interaction between contacting surfaces consists of two components: one normal to the surfaces and one tangential to the surfaces. The normal component consists of the contact pressure that is transmitted between the surfaces. In a “hard” contact relationship, the contact pressure is zero when the clearance between the surfaces is greater than zero (i.e. the surfaces are not in contact); the contact pressure is transmitted only when the clearance between the surfaces becomes zero. Also, the hard contact model minimizes the penetration of slave nodes into the master surface. In a “softened” contact relationship, the contact pressure is a linear or exponential function of the clearance between the surfaces. The softened contact model is often used to model a very soft, thin layer on one or both surfaces.

The tangential component consists of the relative motion (sliding) of the surfaces and possibly, frictional shear stresses. The classical Coulomb friction law is a common friction model used to describe the interaction of contacting surfaces. The model characterizes the frictional behavior between the surfaces using a coefficient of friction, which can be defined in terms of slip rate, contact pressure, and average surface temperature at the contact point. Another friction model is based on a shear stress limit, which is the maximum value of shear stress that can be carried by the interface before the surfaces begin to slide. In ABAQUS/Standard, the discontinuity between the two states - sticking or slipping - can result in convergence problems during the simulation. Hence, friction should be included in the ABAQUS/Standard simulations only when it has a significant influence on the response of the model.

Each surface contact interaction (normal or tangential) can refer to a contact property that specifies a model for the interaction between the contacting surfaces. Several contact interaction models are available in ABAQUS in addition to the ones already mentioned earlier, which are based on the contact pressure and frictional shear forces between the surfaces in contact.

### **5.3.3 Implementation**

Three – dimensional finite element models of the coating and the conical probe were created in ABAQUS/CAE. The coating was modeled as a deformable body using the material parameters ( $E, \nu, h$ ) shown in Table 5-1. The probe was modeled as an analytical rigid body, using the geometric profile shown in Figure 5-17. This assumption was based on the fact that the tungsten probe used in the probe test experiment was almost a rigid body with an infinite stiffness compared to the deformable coating.

A contact interaction was defined between the outer surface of the conical probe and the bottom surface of the coating. Since the probe was modeled as an analytical rigid body and the coating as a deformable body, the probe outer surface is defined as the master surface and the coating bottom surface as the slave surface in the contact pair. In order to minimize the penetration of nodes on the coating surface into the probe surface, the normal component of the contact interaction model was defined as a hard contact relationship. In the probe test experiments, the conical probe is made of tungsten and has

a very smooth surface. A coefficient of friction of approximately 0.099 has been reported in literature [6] for a PTFE/epoxy coating measured using a stainless steel sphere at 28°C. Also, including a friction model (non-zero coefficient of friction) led to convergence difficulties in the contact simulation. Thus, the effect of friction between the probe and coating was considered to be negligible on the overall response of the finite element model by assuming the frictional shear stresses in the coating as negligible. Hence, an assumption was made in the FEA model that the sliding motion of the probe with the coating surface was frictionless. The tangential component of the contact interaction model was thus defined as frictionless by setting the coefficient of friction ( $\mu_T$ ) to zero.

A crack front was defined on the bottom surface of the coating using the experimentally measured debond radius ( $a$ ), as shown in Figure 5-2. The different values of  $a$  used along with the corresponding values of probe penetration distances ( $\delta$ ) are shown in Figure 5-16. The part of the bottom surface of the coating, ahead of the crack front, was rigidly bonded to an invisible substrate to represent the intact adhesion ahead of the crack front, using the PINNED type boundary condition to constrain any displacements. Thus, for nodes lying in the bonded region of the coating, at and ahead of the crack front,

$$u_x = u_y = u_z = 0 \quad (5.8)$$

where  $u_x$ ,  $u_y$ ,  $u_z$  are the nodal displacements in the x-y-z directions. The part of the bottom surface behind the crack front which has debonded was unconstrained and therefore free to deform.

For J – integral evaluation around the crack front region, where bending stresses are significant, second-order iso-parametric continuum elements (C3D20 or C3D27) were recommended to be used [2]. These elements capture the stress concentrations more effectively and are better for modeling geometric features than first-order elements. However, they are not suitable for contact simulations. As shown in Figure 5-18, a constant pressure applied to the face of a second-order element, which does not have a mid-face node, produces forces at the corner nodes acting in the opposite sense of the pressure. ABAQUS/Standard bases important decisions in the contact algorithm on the forces acting on the surface nodes; the ambiguous nature of the nodal forces in second-

order elements can thus cause ABAQUS/Standard to make a wrong decision. In ABAQUS/Standard, the modified second-order tetrahedral elements (C3D10M) are designed to be used in complex contact simulations since they can accurately calculate the contact pressures.

Hence, the coating was meshed using the C3D10M elements in the region where the probe came into contact with the coating. The remaining part was mesh using the C3D20 element type, which is a second-order, iso-parametric, 20-node, three-dimensional continuum element. A typical mesh for the coating is shown in Figure 5-19.

The debond was created in the coating by applying a displacement to the probe, using the probe penetration distance ( $\delta$ ) values from Figure 5-16 corresponding to the experimentally measured debond radius ( $a$ ) value used. Thus, in the finite element simulation, the size of the debond was based on experimental data; however the deformed shape of the coating was computed using surface-based contact interaction between the conical probe surface and the debonded surface of the coating. A typical debonded shape of the coating obtained using finite element contact interaction simulation is shown in Figure 5-20.

Finally, the J – integral was evaluated at the crack front, using the \*CONTOUR INTEGRAL function in ABAQUS/Standard. The values were evaluated successively over five contours; each contour is a ring of elements completely surrounding the crack tip. The values converged over successive contours, thus only the last (i.e. the 5<sup>th</sup>) contour integral value was used as the interfacial fracture energy,  $G_c$ .

#### **5.3.4 Effect of residual stress**

As discussed in Chapter 2, residual stresses arise in coatings due to many different factors like thermal mismatch between the coating and the substrate as the coating is cured or thermally processed, moisture absorption, chemical reactions such as polymer crosslinking. In this study, the effect of residual stress on the interfacial fracture energy ( $G_c$ ) of the epoxy coating/Si system was studied by including a thermal mismatch between the coating and substrate in the finite element model. For a thin, isotropic coating, the residual stress generated in the coating as the coating/substrate system is cooled from temperature  $T_2$  to  $T_1$  is given as [1]:

$$\sigma_r = \int_{T_2}^{T_1} \frac{E}{1-\nu} (\alpha_{coating} - \alpha_{substrate}) dT \quad (5.9)$$

where  $E$  is the elastic modulus and  $\nu$  is the Poisson's ratio of the coating. The ability of the coating to carry stresses is significantly reduced when the coating is heated above its glass transition temperature ( $T_g$ ), hence  $T_2$  can be replaced with  $T_g$  in Equation (5.9). Since the experiments were conducted at ambient conditions,  $T_1$  was taken as the room temperature and the value used was 25 °C.

In the finite element model, the net coefficient of thermal expansion ( $\alpha_{coating} - \alpha_{substrate}$ ) was applied to the coating and the temperature of the coating was varied from the glass transition temperature ( $T_g$ ) of the coating to room temperature ( $T_{amb}$ ) to generate residual stresses in the coating. The bottom surface of the coating was constrained using the PINNED type boundary condition to represent adhesion to an invisible substrate. The values used for these quantities ( $(\alpha_{coating} - \alpha_{substrate}), T_g$ ) are shown in Table 5-1.

### 5.3.5 Results and discussion

The interfacial fracture energy ( $G_c$ ) along the crack front for  $-90^\circ \leq \theta \leq 90^\circ$  are shown for different debond sizes, with probe penetration distances ( $\delta$ ) of 100, 150, 200, 250, 300, 350, 400, 450 and 500 microns, in Figure 5-21. It was observed that the  $G_c$  values sharply increased towards the ends of the crack front ( $\theta \sim \pm 90^\circ$ ) compared to the center of the crack front ( $\theta \sim 0^\circ$ ). The sharp increase in  $G_c$  towards the ends of the crack front may be due to higher stretching deformation at the ends of the crack front compared to center of the crack front where the deformation is believed to be bending dominant. Also, for higher probe penetration distances ( $\delta$ ), the  $G_c$  values increase around the center of the crack front ( $\theta \sim 0^\circ$ ). This increase in  $G_c$  may be due to increasing stretching deformation of the coating, particularly around the center of the crack front, with increasing debond size.

Figure 5-22 shows the  $G_c$  values averaged around the center of the crack front ( $-5^\circ \leq \theta \leq 5^\circ$ ) as a function of probe penetration distance ( $\delta$ ). The  $G_c$  values showed an increase with increase in probe penetration distance ( $\delta$ ) i.e. increasing debond size.

The effect of residual stresses on the interfacial fracture energy ( $G_c$ ) is shown in Figure 5-23 and Figure 5-24 for probe penetration distances ( $\delta$ ) of 200 and 250 microns respectively. These plots show the  $G_c$  values along the crack front ( $-90^\circ \leq \theta \leq 90^\circ$ ) for  $\delta=200, 250$  microns with and without the presence of residual stress ( $\sigma_r$ ) in the finite element model. The results show that  $G_c$  values towards the ends of the crack front ( $\theta \sim \pm 90^\circ$ ), i.e. near the free edge of the coating, show a dramatic increase in the presence of residual stress. Except near the free edge of the coating, the  $G_c$  values are nearly the same along the crack front with and without the presence of residual stress. Thus, it can be concluded that residual stress has a significant impact on the interfacial fracture energy near the region of the crack front which lie closer to the free edge of the coating.

## 5.4 Summary

Using finite element simulations, the interfacial fracture energies ( $G_c$ ) were calculated for the debonded coating/Si substrate specimen using experimental data from the probe test method. Two different modeling techniques were used for the finite element simulations corresponding to the surface profile data of the debonded coating obtained around the crack front obtained using the WKYO® optical profiler; and the overall size of the semi-circular debond in terms of debond radius ( $a$ ) obtained using the optical microscope. The results showed that  $G_c$  increases with increase in debond size. The finite element results obtained using the surface profile data of the debonded coating were significantly affected due to noise in the experimental data. The effect of residual stress on  $G_c$  was investigated in the finite element contact interaction analysis; the results showed that the presence of residual stress increased  $G_c$  near the region of the crack front which lied closer to the free edge of the coating.

## 5.5 Tables

Property	Value
Elastic modulus ( $E$ )	2.7 GPa
Poisson's ratio ( $\nu$ )	0.32
Coating thickness ( $h$ )	70 micron
Net coefficient of thermal expansion ( $\alpha_{coating} - \alpha_{substrate}$ )	$70 \times 10^{-6} / ^\circ\text{C}$
Glass transition temperature ( $T_g$ )	110 $^\circ\text{C}$

**Table 5-1 Material properties of the coating**

## 5.6 Figures

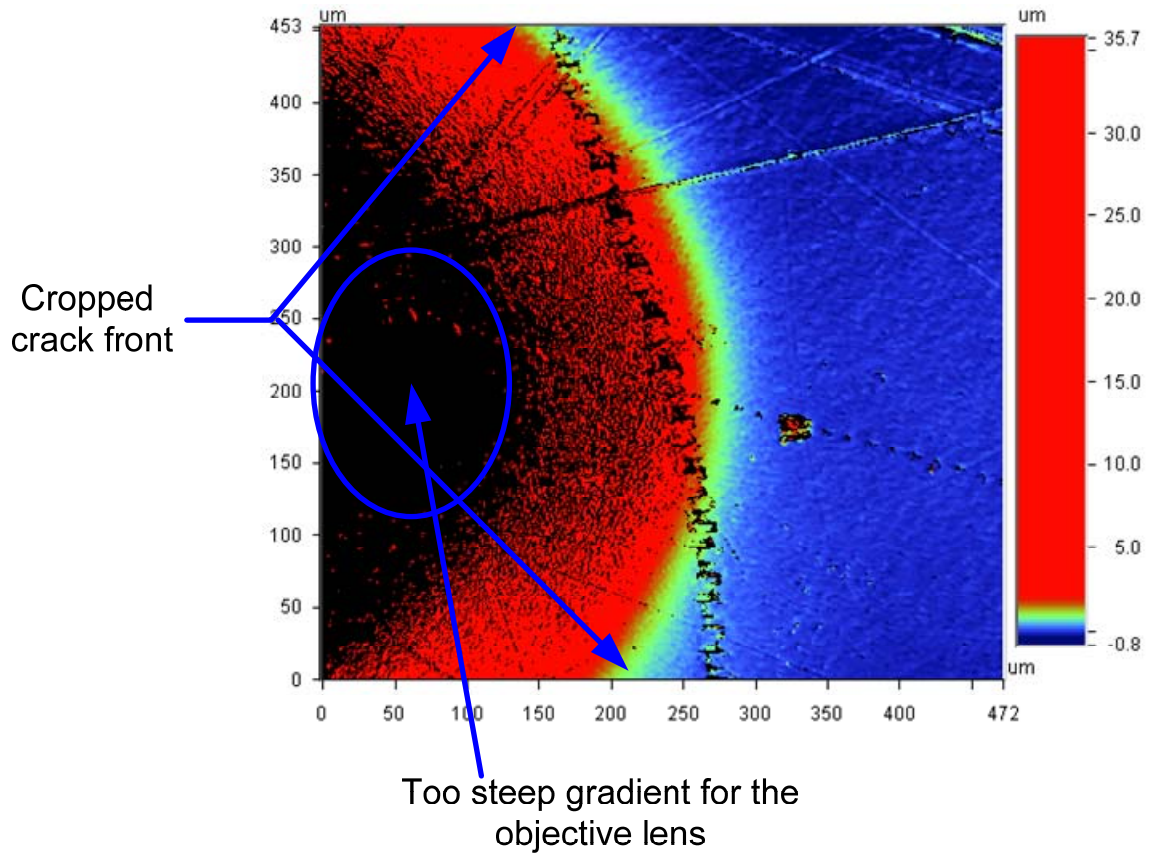


**Figure 5-1** A surface topography image obtained using the WYKO® profiler for a debond of larger size than the field of view of the objective lens; bad data points are present in regions of steep gradient and a cropped image of the debond is obtained.

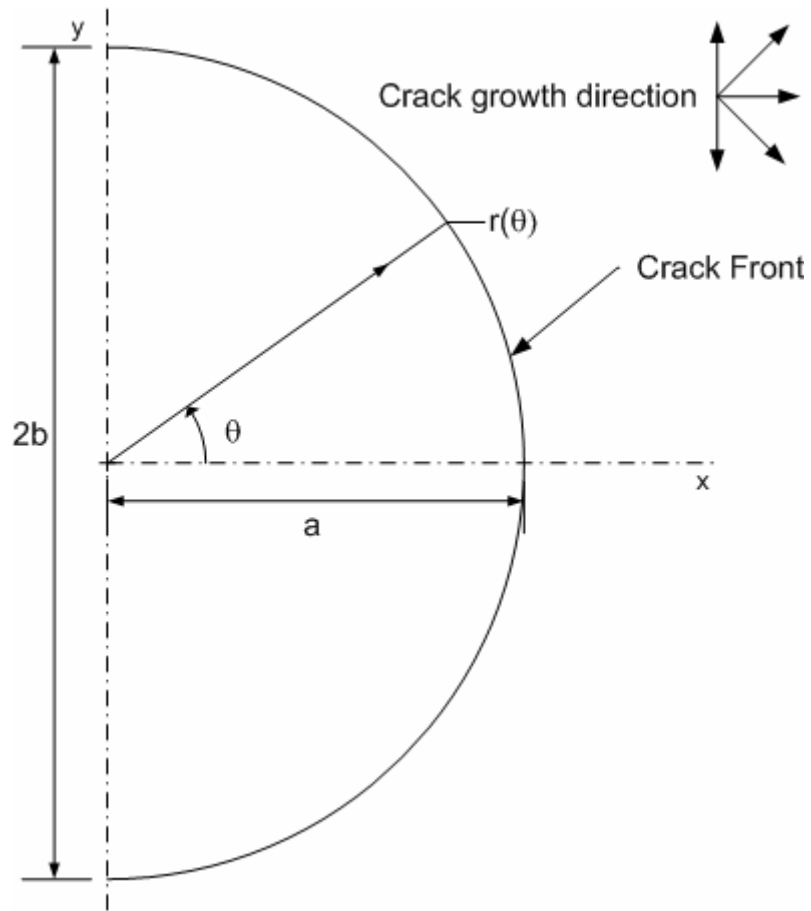


**Figure 5-2 A schematic illustration of a typical crack front profile**

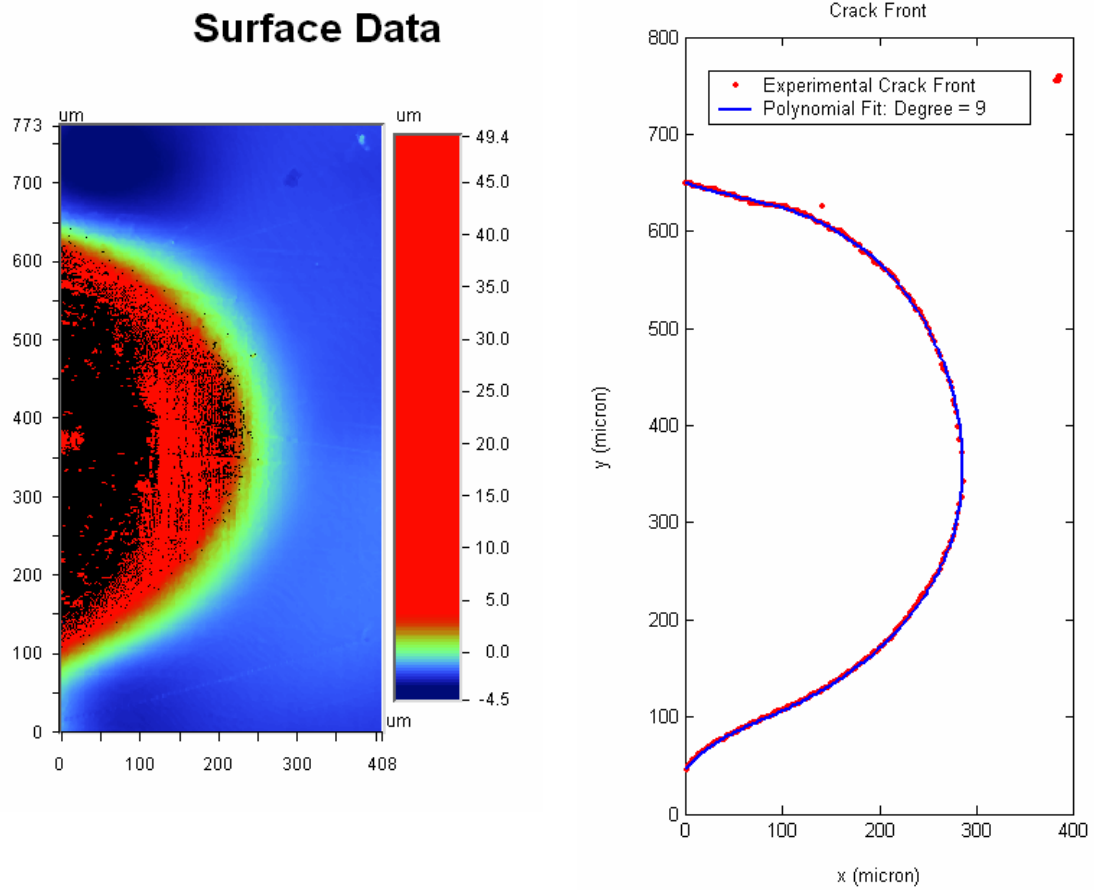
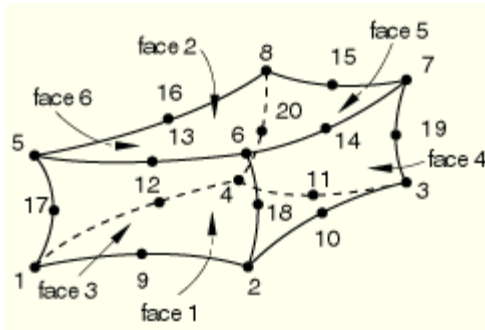


**Figure 5-3 A comparative illustration of the experimental crack front image and the applied analytical polynomial fit, for a debond created using the probe test technique in an epoxy coating(70  $\mu\text{m}$ )/Si substrate specimen and using a probe angle of 25°**

20 – node element  
(C3D20)



27 – node element  
(C3D27)

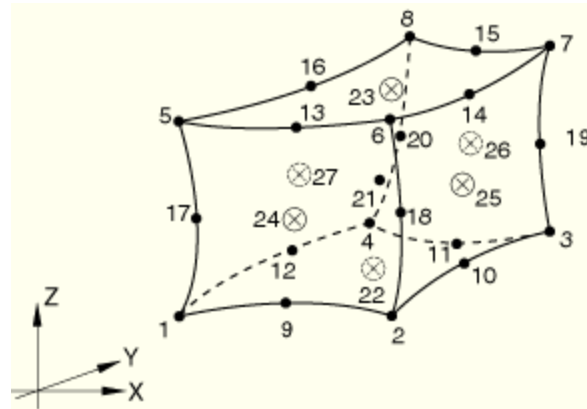


**Figure 5-4 An illustration of the second – order, iso - parametric three – dimensional continuum elements available in ABAQUS**

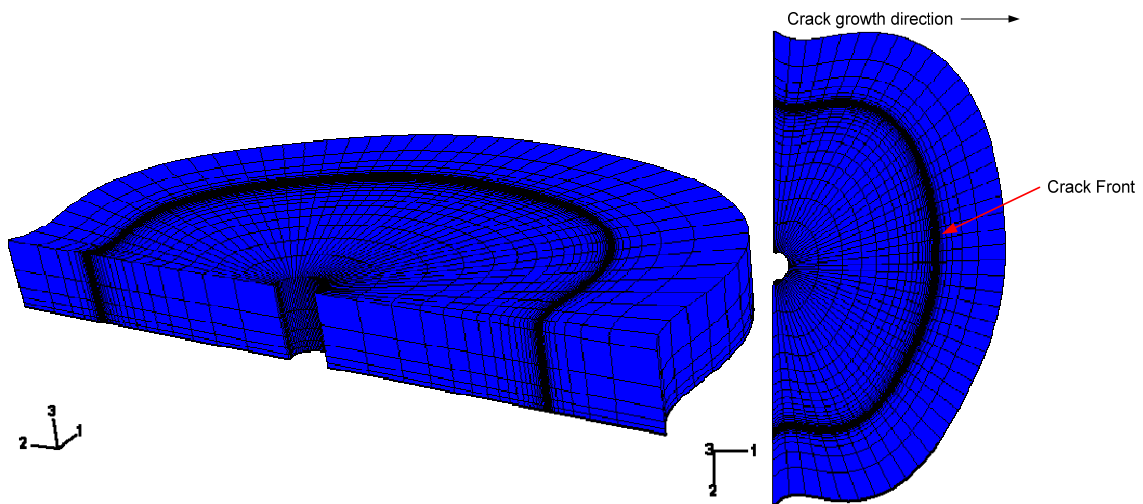


**Figure 5-5 An illustration of the radial-type finite element mesh for the coating used in the displacement-field based FEA model**

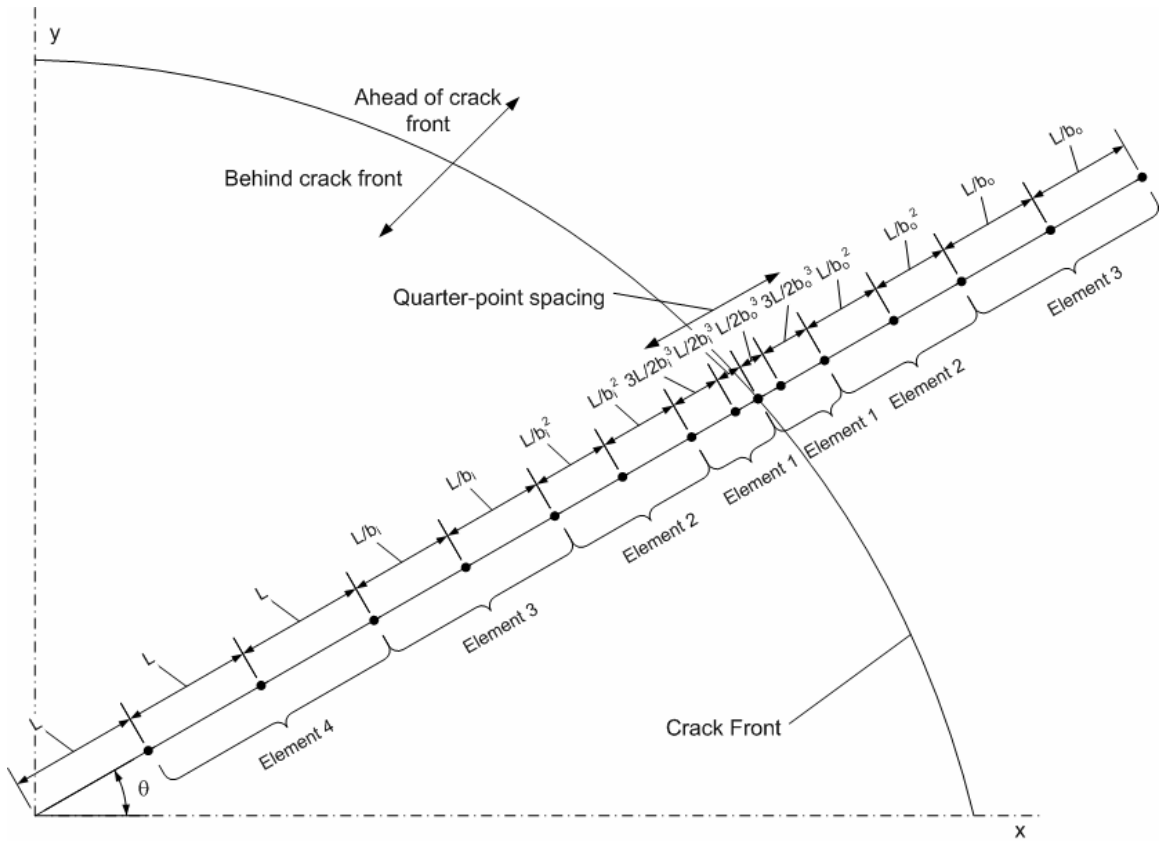


**Figure 5-6 A schematic illustration of the concentrated node spacing towards the crack front, also note the quarter-point spacing at the crack front**

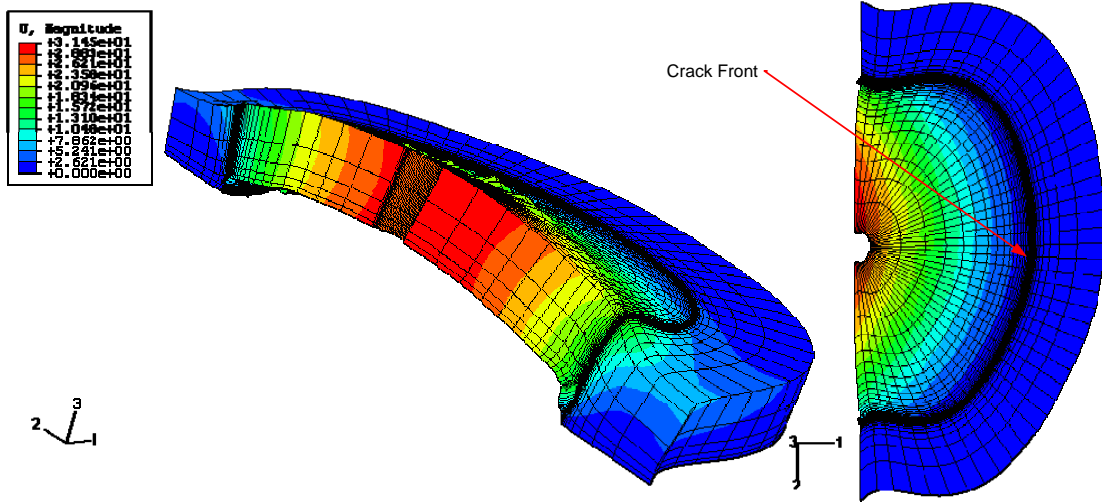


**Figure 5-7** A contour plot of the displacement magnitude ( $u$ ) of the debonded coating obtained using displacement-field based finite element simulation. The thickness of the coating is  $70\ \mu\text{m}$  and the probe angle is  $25^\circ$ .

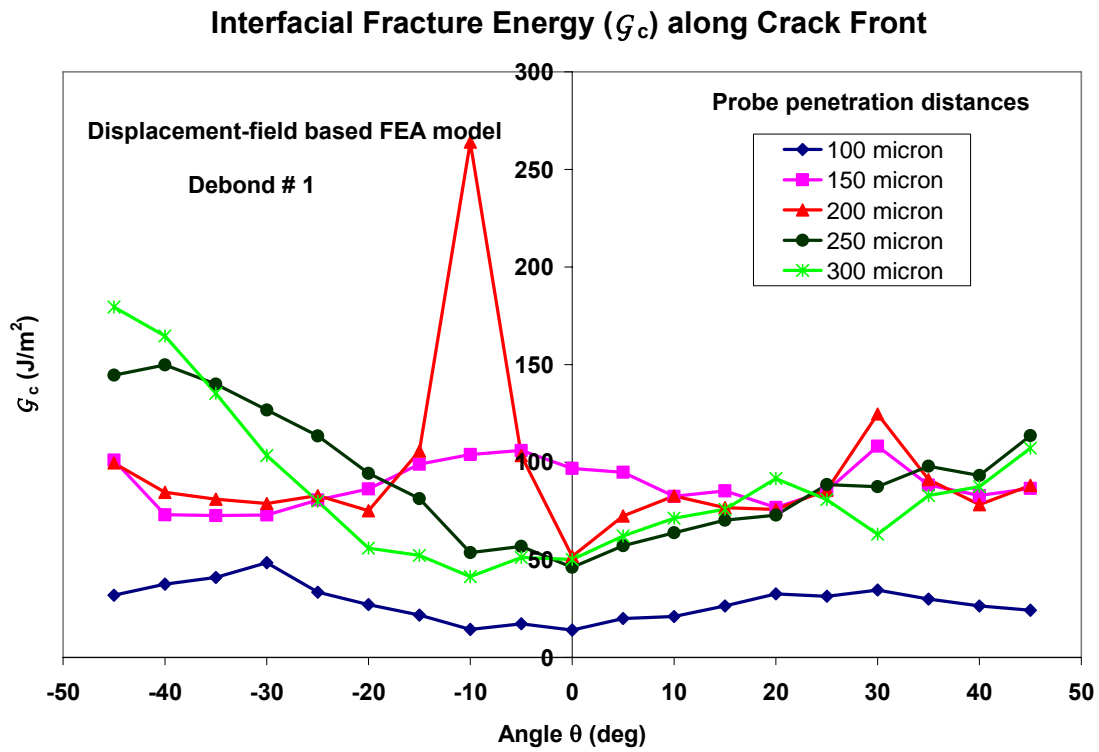


Figure 5-8 Plots of interfacial fracture energy,  $G_c$  along the crack front ( $-45^\circ \leq \theta \leq 45^\circ$ ) of Debond # 1 obtained from displacement-field based FEA model. The debond was created using the probe test technique in an epoxy coating(70  $\mu\text{m}$ )/Si substrate specimen and a probe angle of  $25^\circ$ .

### Interfacial Fracture Energy ( $G_c$ ) along Crack Front

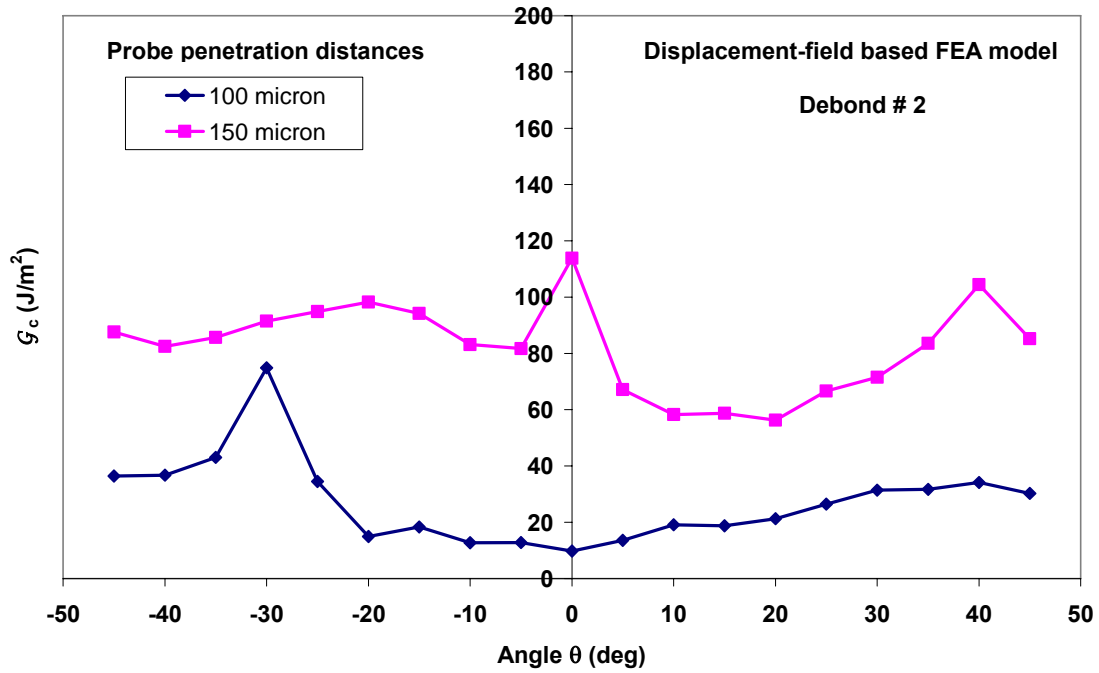
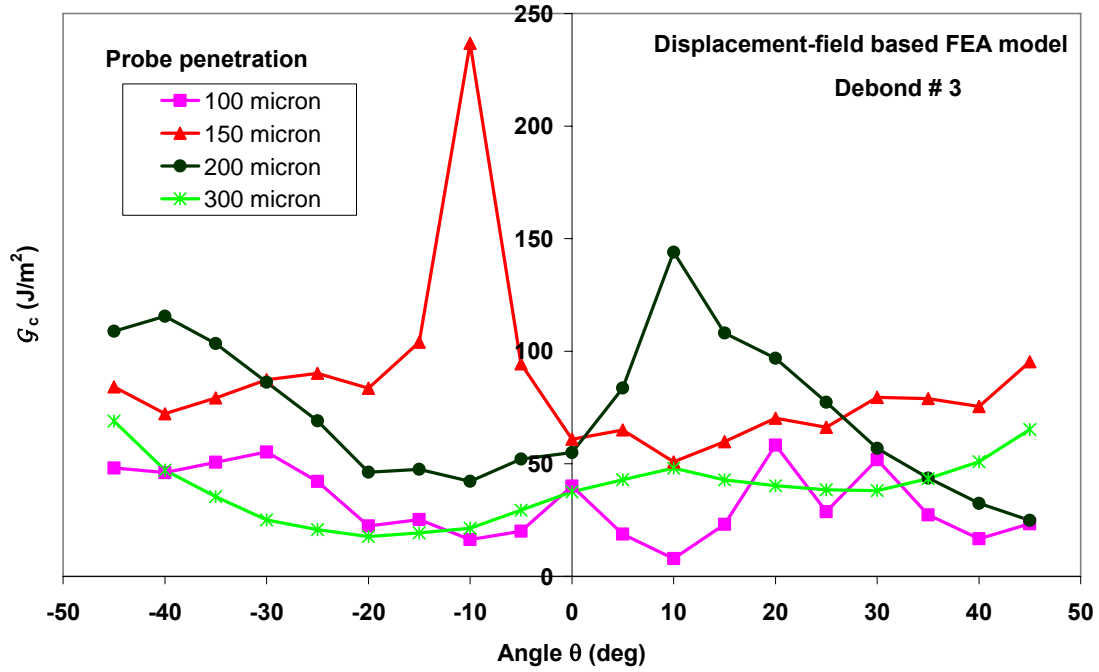


Figure 5-9 Plots of interfacial fracture energy,  $G_c$  along the crack front ( $-45^\circ \leq \theta \leq 45^\circ$ ) of Debond # 2 obtained from displacement-field based FEA model. The debond was created using the probe test technique in an epoxy coating(70  $\mu\text{m}$ )/Si substrate specimen and a probe angle of  $25^\circ$ .

### Interfacial Fracture Energy ( $G_c$ ) along Crack Front



**Figure 5-10** Plots of interfacial fracture energy,  $G_c$  along the crack front ( $-45^\circ \leq \theta \leq 45^\circ$ ) of Debond # 3 obtained from displacement-field based FEA model. The debond was created using the probe test technique in an epoxy coating(70  $\mu\text{m}$ )/Si substrate specimen and a probe angle of  $25^\circ$

### Interfacial Fracture Energy ( $G_c$ ) along Crack Front

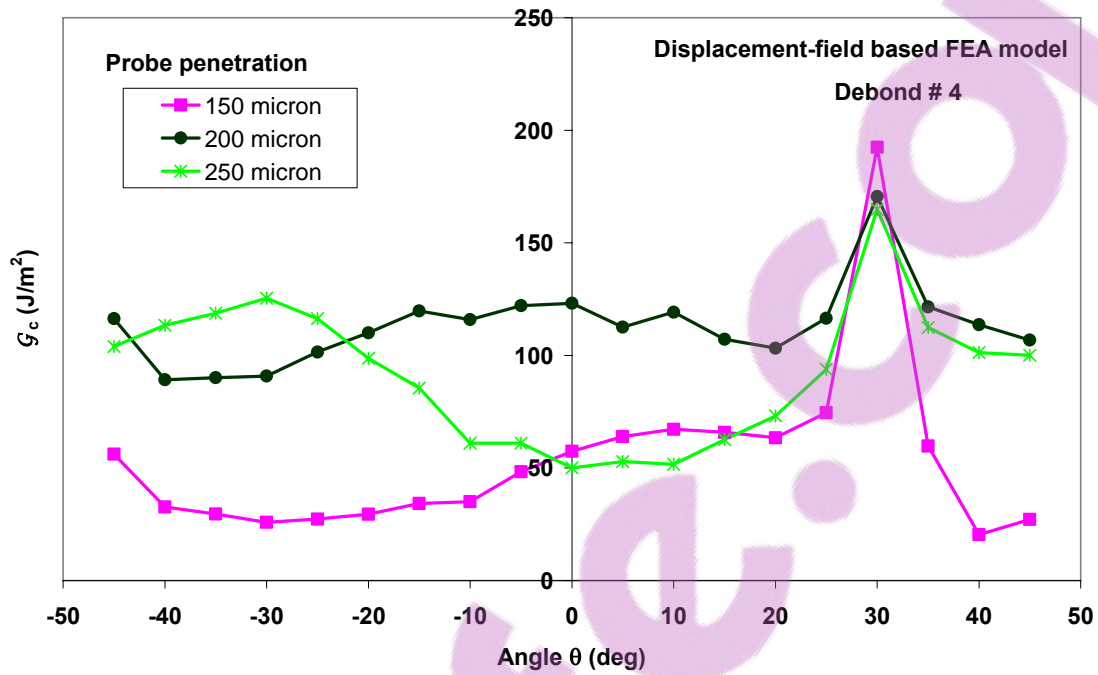


Figure 5-11 Plots of interfacial fracture energy,  $G_c$  along the crack front ( $-45^\circ \leq \theta \leq 45^\circ$ ) of Debond # 4 obtained from displacement-field based FEA model. The debond was created using the probe test technique in an epoxy coating(70  $\mu\text{m}$ )/Si substrate specimen and a probe angle of  $25^\circ$

Effect of mesh refinement on  $G_c$  values evaluated along crack front

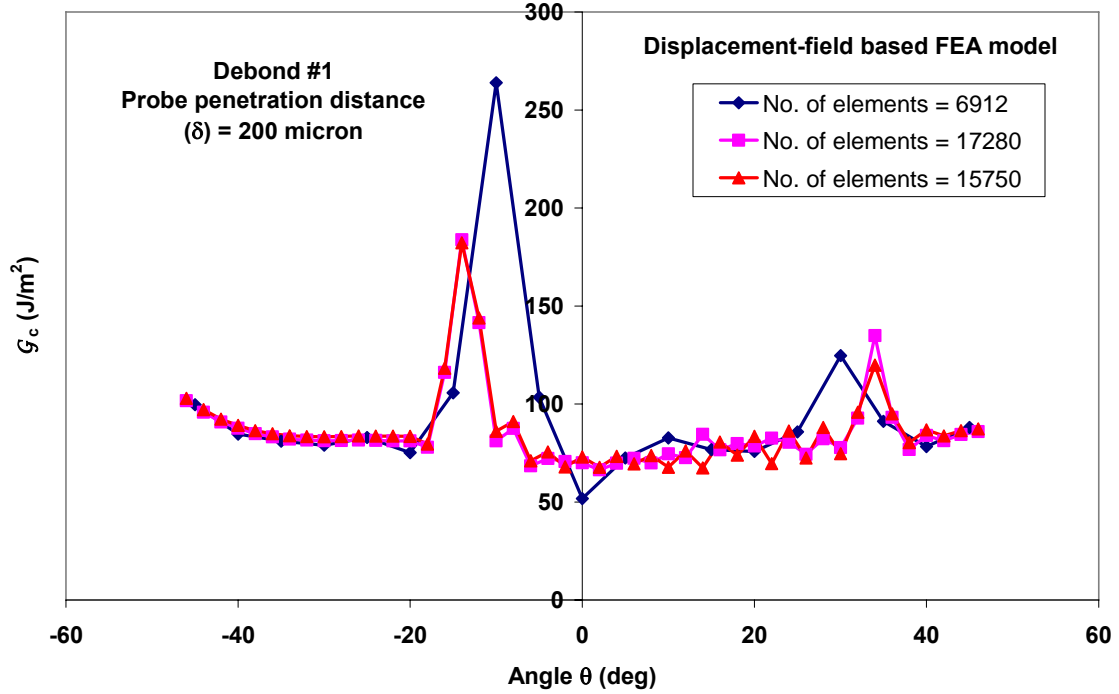


Figure 5-12 Plots of interfacial fracture energy,  $G_c$  along the crack front ( $-45^\circ \leq \theta \leq 45^\circ$ ) for Debond #1 -  $\delta = 200$  micron, obtained using displacement-field based FEA model, showing the effect of mesh refinement on  $G_c$  values. The debond was created using the probe test technique in an epoxy coating(70  $\mu\text{m}$ )/Si substrate specimen and a probe angle of  $25^\circ$ .

Effect of mesh refinement on  $G_c$  values evaluated along crack front

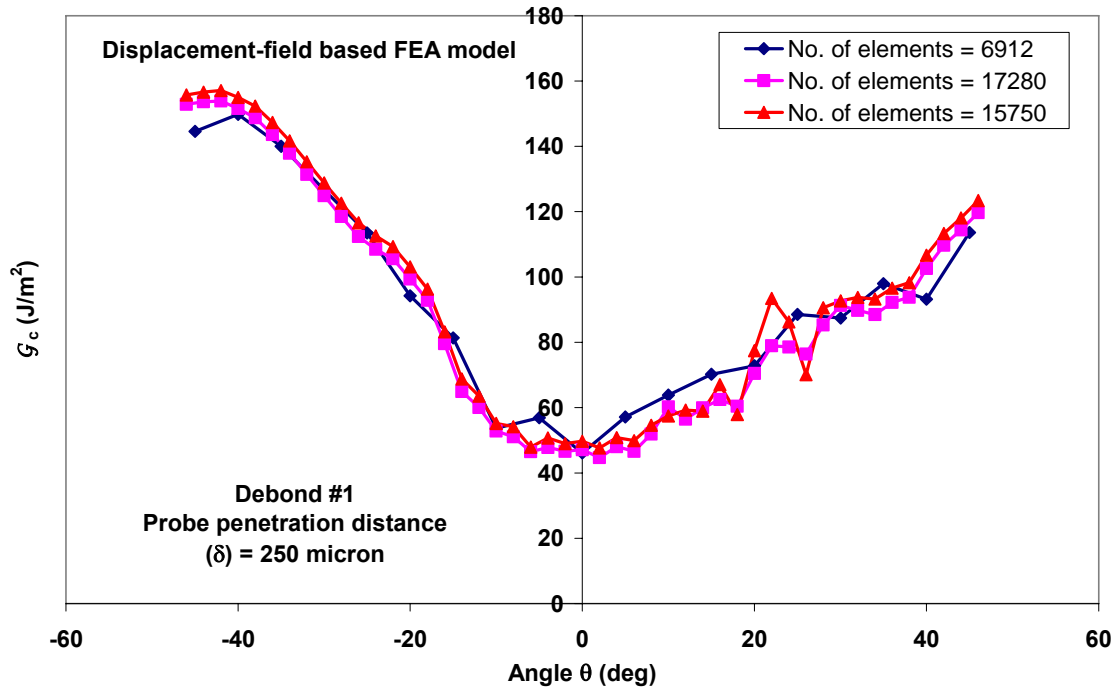
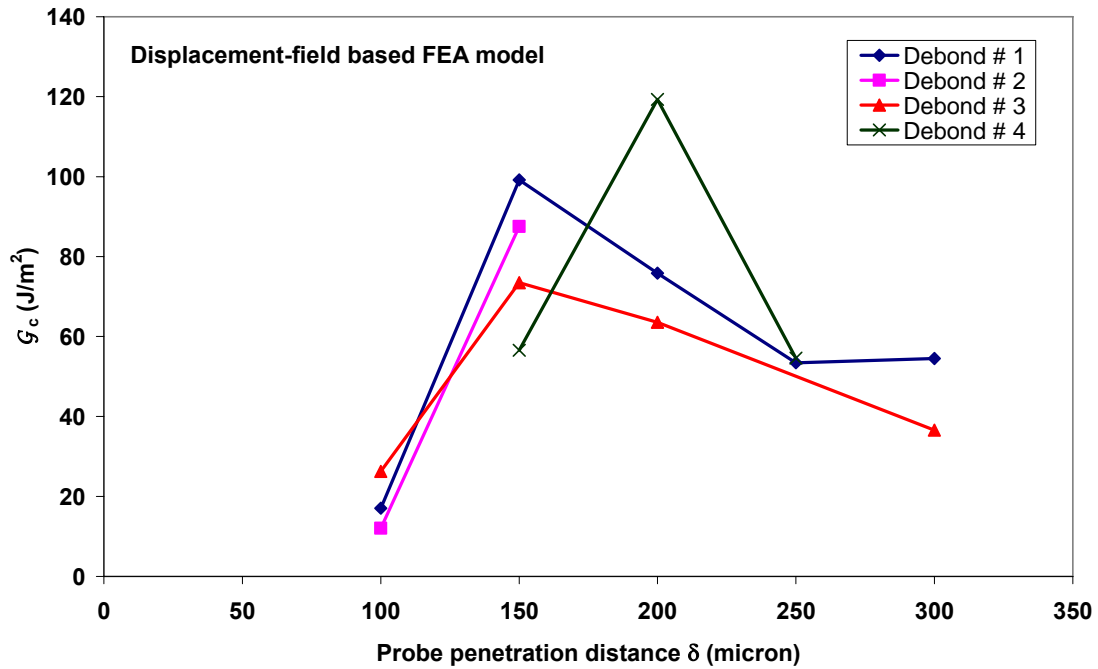
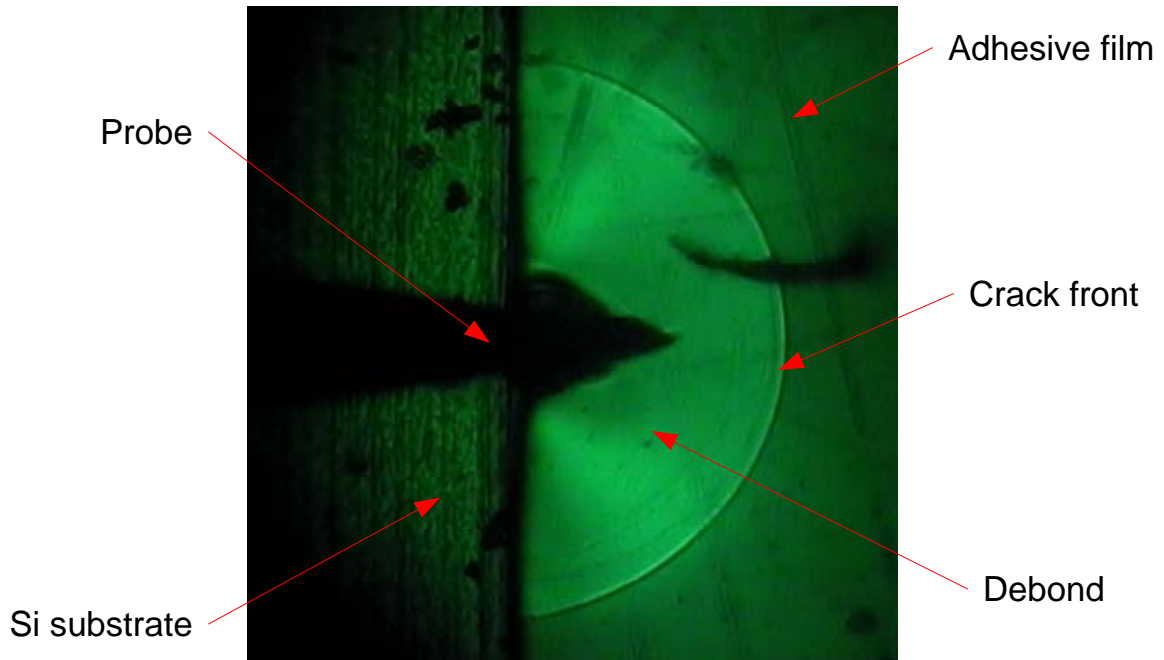


Figure 5-13 Plots of interfacial fracture energy,  $G_c$  along the crack front ( $-45^\circ \leq \theta \leq 45^\circ$ ) for Debond #1 -  $\delta = 250$  micron, obtained using displacement-field based FEA model, showing the effect of mesh refinement on  $G_c$  values. The debond was created using the probe test technique in an epoxy coating(70  $\mu\text{m}$ )/Si substrate specimen and a probe angle of  $25^\circ$ .

### Interfacial fracture energy ( $\mathcal{G}_c$ ) vs. Probe penetration distance



**Figure 5-14** Plots of interfacial fracture energy,  $\mathcal{G}_c$  averaged near the center of the crack front ( $-5^\circ \leq \theta \leq 5^\circ$ ) vs. probe penetration distance ( $\delta$ ) obtained using displacement-field based FEA model. The debonds were created using the probe test technique in an epoxy coating(70  $\mu\text{m}$ )/Si substrate specimen and using a probe angle of  $25^\circ$



**Figure 5-15** A typical debonding event in the coating for the coating (70 $\mu\text{m}$ )/Si substrate specimen using a probe angle of 25 $^\circ$

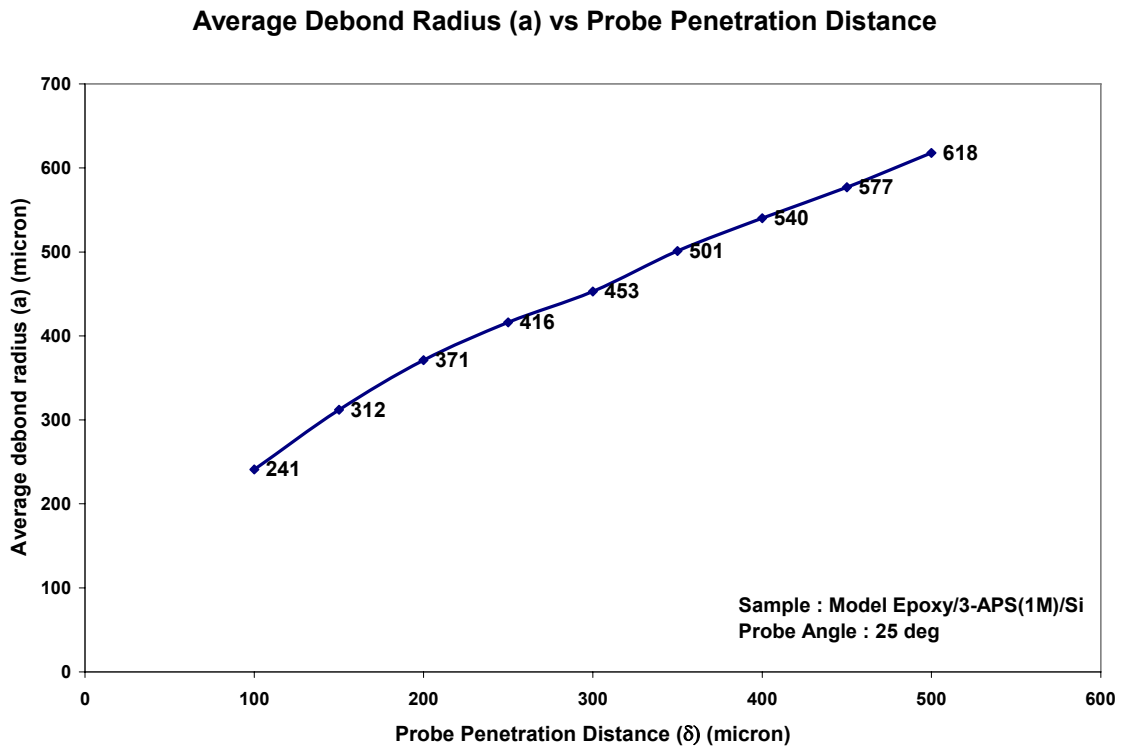


**Figure 5-16 Plot of average debond radius (a) along the probe direction over 5 different debonds as a function of probe penetration distance ( $\delta$ ) for the coating (70 $\mu$ m)/Si substrate specimen and using a probe angle of 25°**

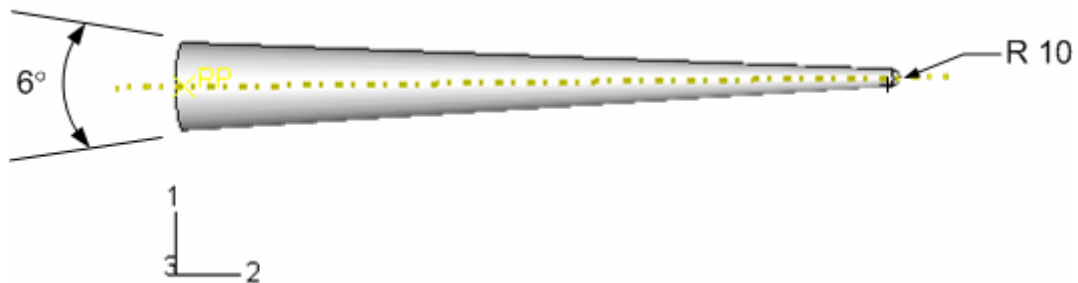


**Figure 5-17 A schematic of the geometric profile of the probe**

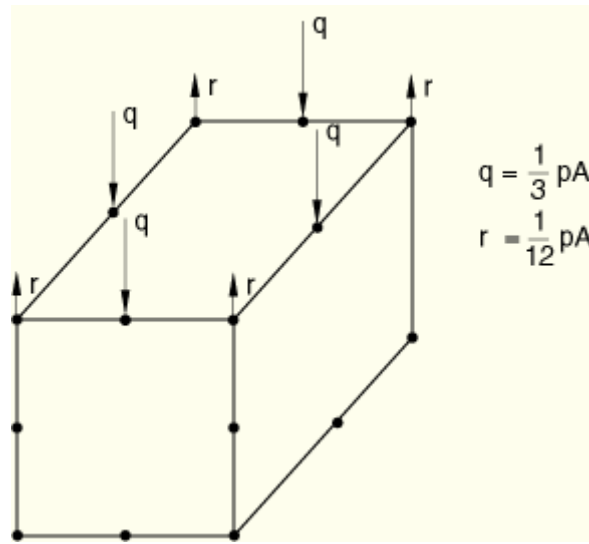


**Figure 5-18 Equivalent nodal loads produced by a constant pressure on the second-order element face in contact simulations**

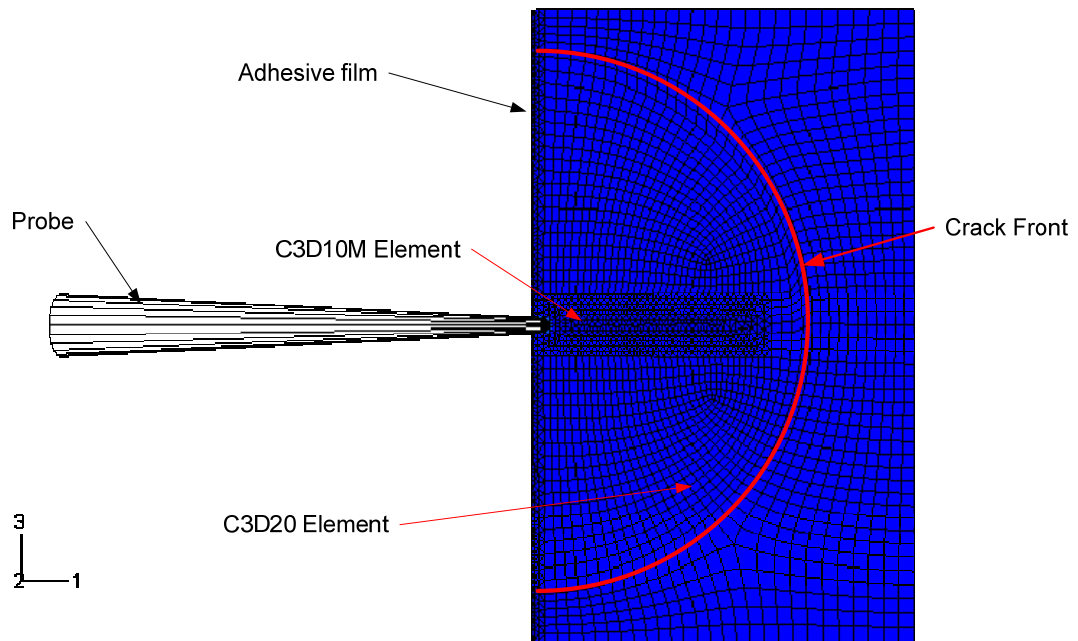


**Figure 5-19 A schematic of the finite element mesh used for contact interaction simulation**

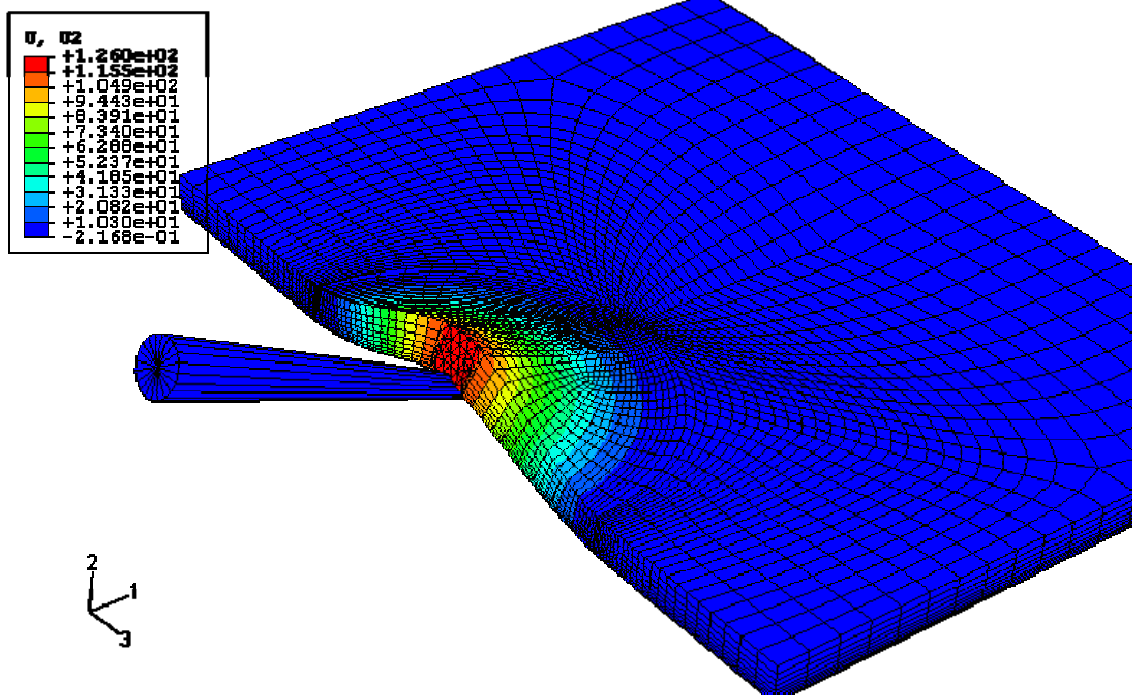


**Figure 5-20** A contour plot of the out-of-plane displacement ( $u_2$ ) of the debonded coating obtained using finite element contact interaction simulation. The thickness of the coating is 70  $\mu\text{m}$  and the probe angle is 25°.

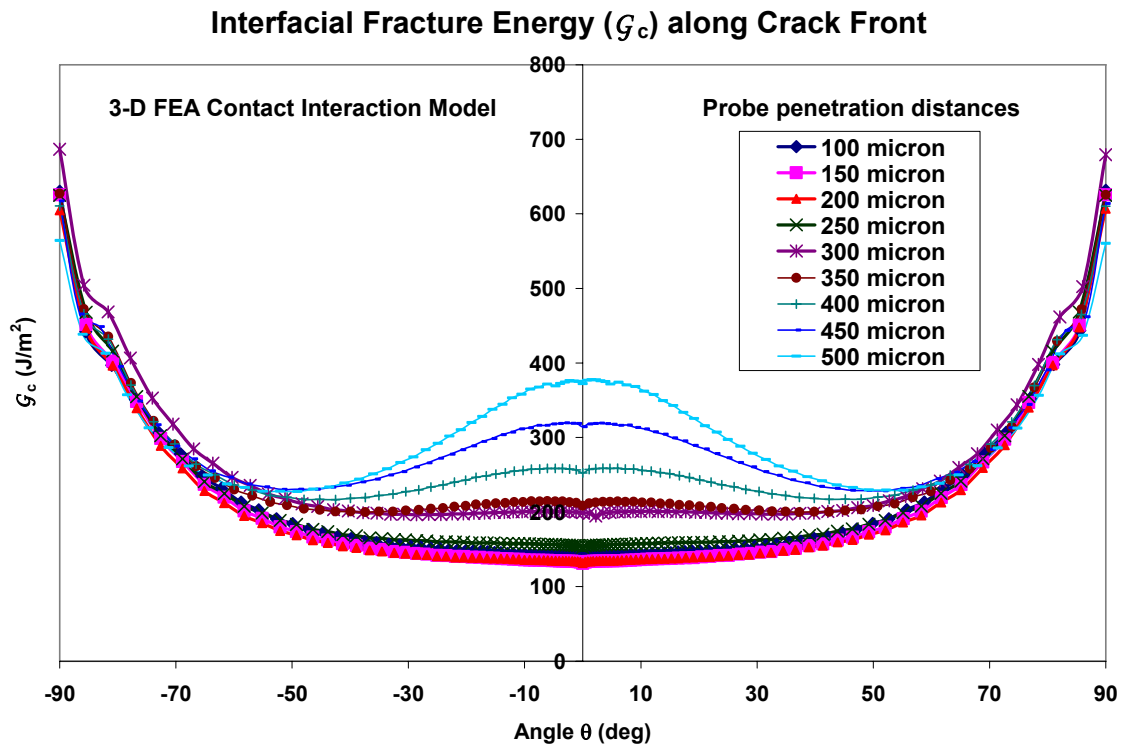


**Figure 5-21** Plots of interfacial fracture energy,  $G_c$  along the crack front ( $-90^\circ \leq \theta \leq 90^\circ$ ) calculated using finite element contact interaction method. The debond was created using the probe test technique in an epoxy coating(70  $\mu\text{m}$ )/Si substrate specimen and a probe angle of  $25^\circ$ .

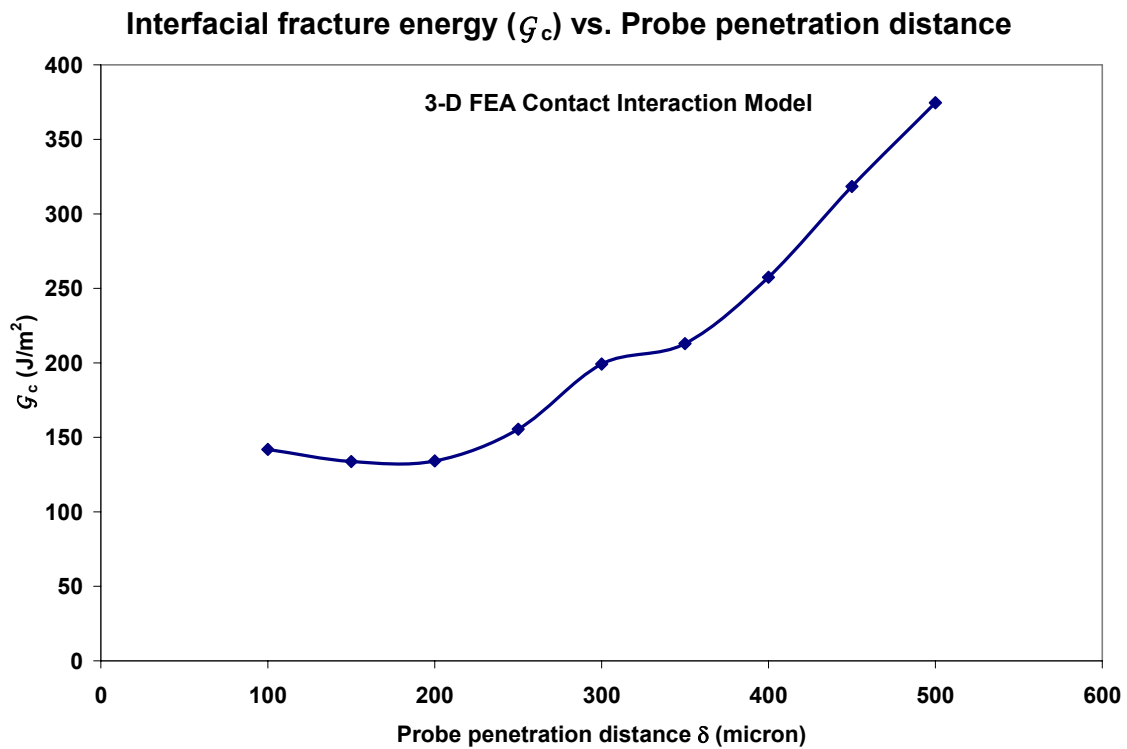


**Figure 5-22** Plot of interfacial fracture energy,  $G_c$  averaged near the center of the crack front ( $-5^\circ \leq \theta \leq 5^\circ$ ) vs. probe penetration distance ( $\delta$ ), calculated using finite element contact interaction method. The debonds were created using the probe test technique in an epoxy coating ( $70 \mu\text{m}$ )/Si substrate specimen and a probe angle of  $25^\circ$

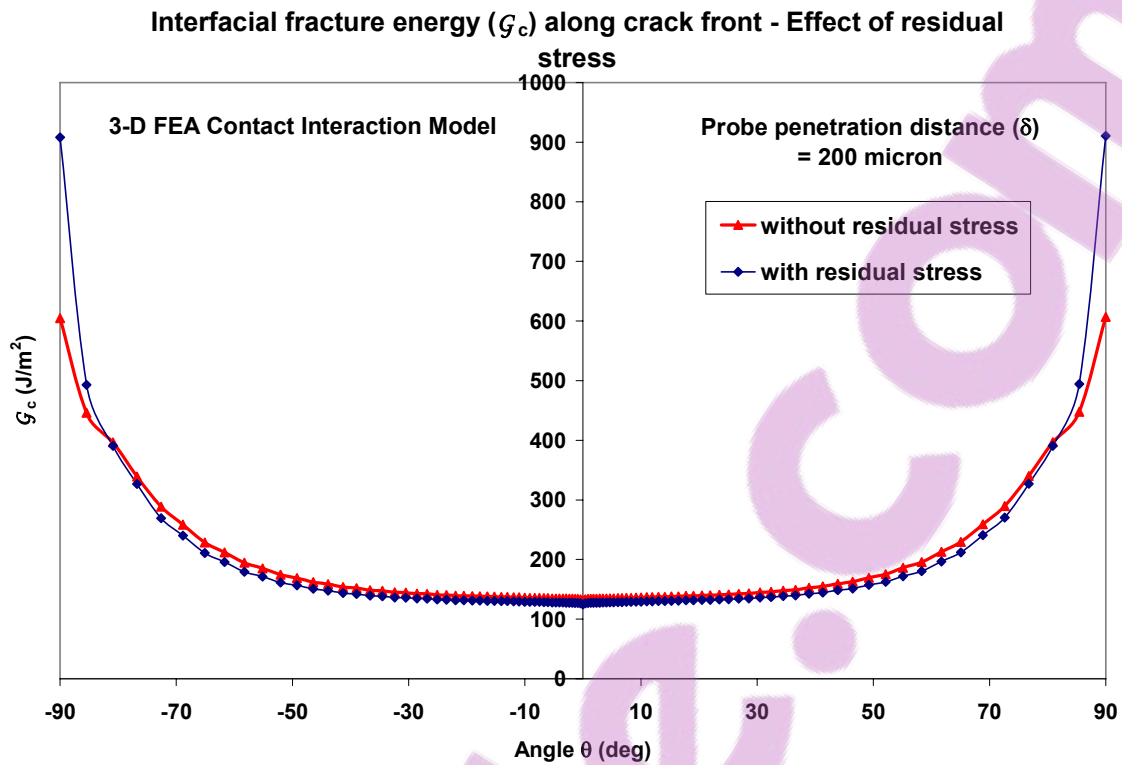


**Figure 5-23** Plots of interfacial fracture energy,  $G_c$  along the crack front ( $-90^\circ \leq \theta \leq 90^\circ$ ) for  $\delta = 200$  micron calculated with and without the presence of residual stress in the finite element contact interaction model. The debond was created using the probe test technique in an epoxy coating ( $70 \mu\text{m}$ )/Si substrate specimen and a probe angle of  $25^\circ$

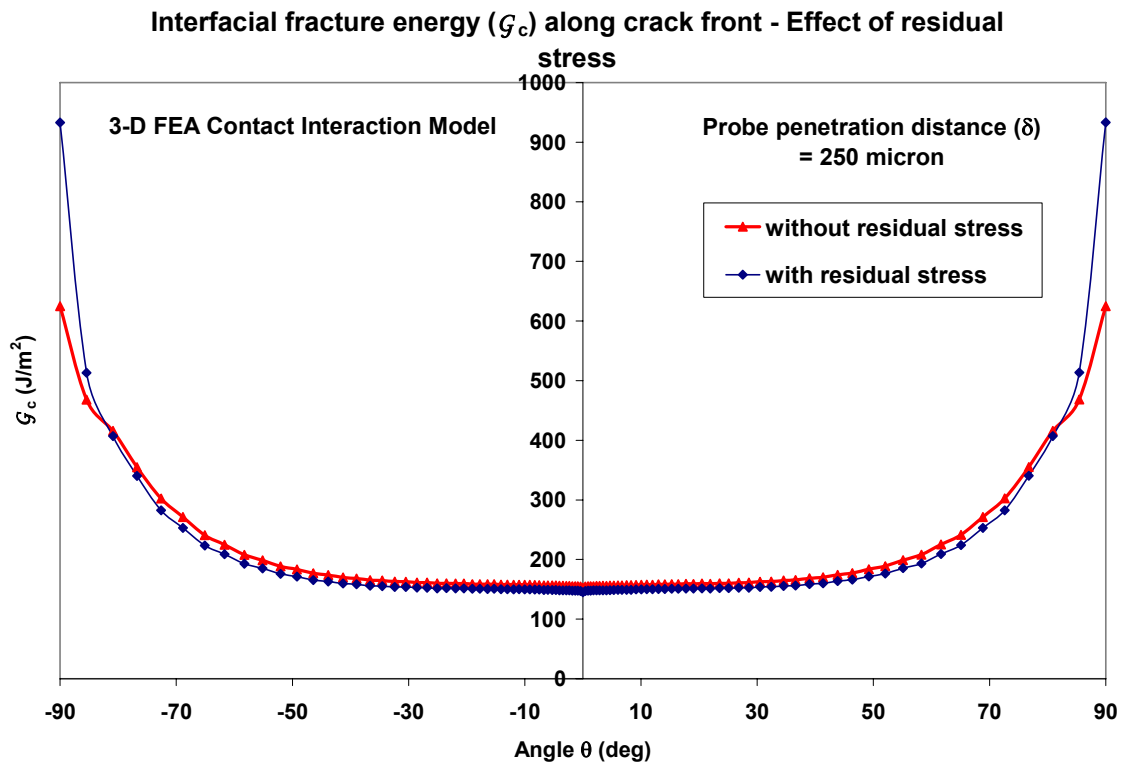


**Figure 5-24** Plots of interfacial fracture energy,  $G_c$  along the crack front ( $-90^\circ \leq \theta \leq 90^\circ$ ) for  $\delta = 250$  micron calculated with and without the presence of residual stress in the finite element contact interaction model. The debond was created using the probe test technique in an epoxy coating ( $70 \mu\text{m}$ )/Si substrate specimen and a probe angle of  $25^\circ$

## 5.7 References

1. Dillard, D.A. and A.V. Pocius, *The mechanics of adhesion*. Adhesion science and engineering, ed. A.V. Pocius. Vol. 1. 2002, Amsterdam ; Boston: Elsevier.
2. ABAQUS Inc, *ABAQUS Version 6.5 Documentation*. 2004, ABAQUS, Inc: Providence, RI, USA.
3. The MathWorks Inc, *MATLAB Version 6.5 Release 13 Documentation*. 2002, The MathWorks, Inc: USA.
4. Barber, C.B., D.P. Dobkin, and H. Huhdanpaa, *The Quickhull algorithm for convex hulls*. Acm Transactions on Mathematical Software, 1996. **22**(4): p. 469-483.
5. Boresi, A.P. and R.J. Schmidt, *Advanced mechanics of materials*. 6th ed. 2003, New York: John Wiley & Sons. xiii, 681.
6. McCook, N.L., et al., *Cryogenic friction behavior of PTFE based solid lubricant composites*. Tribology Letters, 2005. **20**(2): p. 109-113.

## Chapter 6 Summary

### 6.1 Overview

This chapter presents a comparison of the present work with some of the previous studies conducted in this area by other researchers and a summary for the present work. The works of Dingying Xu [1] and Kristopher Mount [2] are acknowledged for comparison with the present work.

### 6.2 Comparison with Xu's work

The probe test experiments were used by Xu [1] to quantitatively determine adhesion under critical debonding for epoxy/Si bonded specimens with different silane coupling agent treatments. Figure 6-1 and Figure 6-2 show the plot of debond radius ( $a$ ) as a function of probe penetration distance ( $\delta$ ) as obtained from Xu's work and the present work respectively. Figure 6-3 and Figure 6-4 show the plot of debond radius ( $a$ ) as a function of coating deflection ( $w_0$ ) as obtained from Xu's work and the present work respectively. It can be observed from Figure 6-1, Figure 6-2, Figure 6-3 and Figure 6-4 that the experimentally measured data ( $a, \delta, w_0$ ) for the debond geometry in the present work is quite consistent with the corresponding data from Xu's work.

Figure 6-5 and Figure 6-6 show the plot of debond area ( $A$ ) as a function of probe penetration distance ( $\delta$ ) as obtained from Xu's work and the present work respectively. In Figure 6-5 from Xu's work, the values shown for the debond area have been incorrectly increased by a factor of 10, this can be verified by calculating the debond area using the corresponding debond radii data from Xu's work shown in Figure 6-1 and Figure 6-3. After taking into account the correction in Figure 6-5, the debond area data obtained in the present work (Figure 6-6) appears consistent with the debond area data for front side coated Si substrate from Xu's work (Figure 6-5) and in both cases, the debond area ( $A$ ) increases linearly with probe penetration distance ( $\delta$ ). As shown in Figure 6-6 from the present work, the debond aspect ratio ( $\gamma$ ) values lie in the range

$0.95 \leq \gamma \leq 1.15$ , hence in the present work the shape of the debond was approximated as semi-circular. However, in Figure 6-1 from Xu, the debond aspect ratio ( $\gamma$ ) values lie in the range  $0.77 \leq \gamma \leq 0.95$ , thus the shape of the debond in Xu's experiments becomes semi-elliptical with increasing probe penetration distance ( $\delta$ ) i.e. larger debond sizes. The difference in the shape of the debond in the present work and Xu's work may be due to the difference in the silane coupling agent treatment, residual stresses between the test specimens; and test technique between two operators.

Figure 6-7 shows the interfacial fracture energies calculated by Xu using Equation (6.1), given as:

$$G_c = 8D \frac{w_0^2}{a^4} \quad (6.1)$$

where  $w_0$  is the debond height and  $a$  is the debond radius. It was shown in the present study that Equation (6.1) is based on a thin plate – small deflection formation of plate theory. The corresponding plot using the thin plate – small deflection formulation obtained from the present work is shown in Figure 6-8 and the  $G_c$  values shown in Figure 6-8 are consistent with the corresponding values from Xu's work (Figure 6-7).

### 6.3 Comparison with Mount's work

Mount [2] used an out-of-plane edge-loaded thin film model shown in Figure 6-9 to obtain strain energy release rates ( $G_{tot}$ ) using finite element analysis. In Mount's work, the coating in the probe test was assumed as a thin plate and since the thin plates are much stiffer in-plane than out-of-plane, the out-of-plane displacement was considered dominant by Mount in the probe test, thereby ignoring any in-plane displacement of the coating. Thus, the finite element model shown in Figure 6-9 was used by Mount as representative of the probe test geometry. In the present work, it was shown in Chapter 4 that the deformation of the coating in the probe test, lie in the domain of thick plate – large deflection theory and thus, stretching (in-plane) deformation, particularly at the crack front, would play a significant role. It should also be noted that in Mount's work,  $G_{tot}$  was the applied strain energy release rate for different debond sizes under an applied constant displacement.  $G_{tot}$  was defined for a multi-mode loaded specimen as the sum of

Mode I, Mode II and Mode III energy release rates. In contrast, in the present work  $G_c$  was the critical strain energy release rate (or interfacial fracture energy) calculated using experimental data for an arrested crack under different applied displacements.

Figure 6-10 shows a plot of  $\log$  of  $G_{tot}$  along the crack front for different debond radii and no residual stress from Mount's work. In Mount's finite element model, the free edge is located at  $0^\circ$  and the center of the crack front is located at  $90^\circ$  whereas in the finite element model used in the present work, the center of the crack front is at located  $0^\circ$  and free edge is located at  $90^\circ$ . Thus, it can be seen that the  $G_{tot}$  values are nearly constant near the center of the crack front and sharply increase near the free edge. These results are consistent with the corresponding results for lower probe penetration distances ( $\delta$ ) shown in Figure 6-12 from the present work, which show that  $G_c$  values are nearly constant near the center of the crack front ( $0^\circ$ ) and sharply increase near the free edge ( $90^\circ$ ).

Also, Figure 6-11 shows a plot of  $\log$  of  $G_{tot}$  along the crack front for different debond radii in the presence of residual stress from Mount's work. Comparing Figure 6-10 and Figure 6-11, the results from Mount's work show that the fracture energy increases in the presence of residual stress at the free edge of the coating. These results are consistent with Figure 6-13 from the present work, which also shows an increase in  $G_c$  near the free edge of the coating in the presence of residual stress.

## 6.4 Summary

In the present work, the probe test for measuring adhesion of thin films and coatings was implemented experimentally under an optical microscope and an optical profiler. A thin film adhesive (epoxy polymer) coated silicon substrate specimen was used as a sample system to conduct probe test experiments. A semi-circular crack front was observed at the interface of the coating/Si substrate specimen as the probe slid underneath the coating. Using an optical microscope, the debond radius was recorded as a function of probe penetration distance. The experimental data showed that the crack growth was stable and linearly dependent on the applied load. Using the WYKO<sup>®</sup> optical

profiler, the vertical displacement profile of the debond around the crack front region was measured for different debond sizes. Using the optical microscope or the WYKO<sup>®</sup> optical profiler, the probe test technique can be used with both transparent as well as opaque coatings. A major limitation with the WYKO<sup>®</sup> profiler technique was the large quantity of noise in the surface topography data obtained from the optical profiler, thus creating difficulties in the quantitative analysis of the data to obtain an accurate estimation of interfacial fracture energy ( $G_c$ ).

Two analytical techniques were used to calculate the interfacial fracture energies ( $G_c$ ) for the debonded coating/Si substrate specimen using experimental data from the probe test. The first approach used a shaft loaded blister approximation for the probe test geometry and using the overall size of the semi-circular debond in terms of debond radius ( $a$ ) obtained using the optical microscope, different plate theory formulations were used to obtain  $G_c$  values. The second approach used the surface profile data of the debonded coating obtained around the crack front obtained using the WKYO<sup>®</sup> optical profiler; and by numerically estimating the curvature at the crack tip from the experimental, the  $G_c$  values were calculated. Two different modeling techniques were used for the finite element simulations corresponding to the surface profile data of the debonded coating obtained around the crack front obtained using the WKYO<sup>®</sup> optical profiler; and the overall size of the semi-circular debond in terms of debond radius ( $a$ ) obtained using the optical microscope.

Table 6-1 shows a summary of the different experimental data used with the corresponding analytical/numerical techniques for analyzing the probe test geometry. Figure 6-14 shows a comparative plot of interfacial fracture energy ( $G_c$ ) as a function of probe penetration distance ( $\delta$ ) obtained using all the different analytical and finite element based techniques. As mentioned earlier in Chapter 4,  $G_c$  values predicted using thin plate theories were over-estimated since thin plate theory neglects the transverse strains in the coating. The  $G_c$  values obtained using curvature method were under-estimated since the work done near the crack front by stretching (in-plane) deformation was ignored. The contribution by stretching deformation was ignored in the calculation of

$G_c$  values using curvature method due to inability to experimentally measure the in-plane deflection in the coating. Finally, the  $G_c$  values predicted using thick plate – large deflection formulation and the FEA contact interaction model converge with increasing probe penetration distance ( $\delta$ ).

#### **6.4.1 Probe bending**

In the present work, the bending of the probe in contact with the coating and substrate was not taken into account. As shown in Figure 3-5, the tungsten probe used in the probe test experiment was assumed as a rigid body with an infinite stiffness compared to the deformable coating. A preliminary calculation based on an analytical beam bending model was performed using the loading and boundary conditions on the probe shown in Figure 6-15; where  $P$  is the reaction load on the probe due to the contact with the coating. The calculations were based on an approximate estimate of load  $P$  from the thick plate-large deflection shaft-loaded blister model; however based on these calculations, it is believed that the probe would undergo elastic bending. This would result in the probe tip flattening on the substrate surface, thereby decreasing the effective probe angle at the crack tip of the debond from  $28.0^\circ$  to approximately  $6.0^\circ$  which is the cone angle of the probe. The effect of probe bending was not taken into account in any of the analytical and finite element based techniques used in the present work to analyze the probe test geometry and calculate the interfacial fracture energies ( $G_c$ ) for the debonded coating/Si substrate specimen. Further work is needed to accurately estimate the contact load between the probe and the coating; calculate the net bending of the probe and the effect of probe bending on the calculated interfacial fracture energies ( $G_c$ ) for the debonded coating/Si substrate specimen in the probe test experiment.

## 6.5 Tables

Experimental data	Analytical methods				Numerical methods	
	Thin plate-small deflection theory	Thin plate-large deflection theory	Thick plate-large deflection theory	Curvature method	Displacement field-based FEA model	FEA contact interaction model
Coating material parameters $E, \nu, h$  $\alpha_{coating}, T_g$	✓	✓	✓	✓	✓	✓ (Residual stress model only)
Optical microscopy data $a, \delta$	✓	✓	✓			✓
WYKO optical profiler data $z(x, y) \rightarrow \left( \frac{d^2 z}{dr^2} \right)$  $z(x, y)$				✓	✓	

**Table 6-1** A matrix summarizing the different experimental data used with the corresponding analytical/numerical techniques for analyzing the probe test geometry

## 6.6 Figures

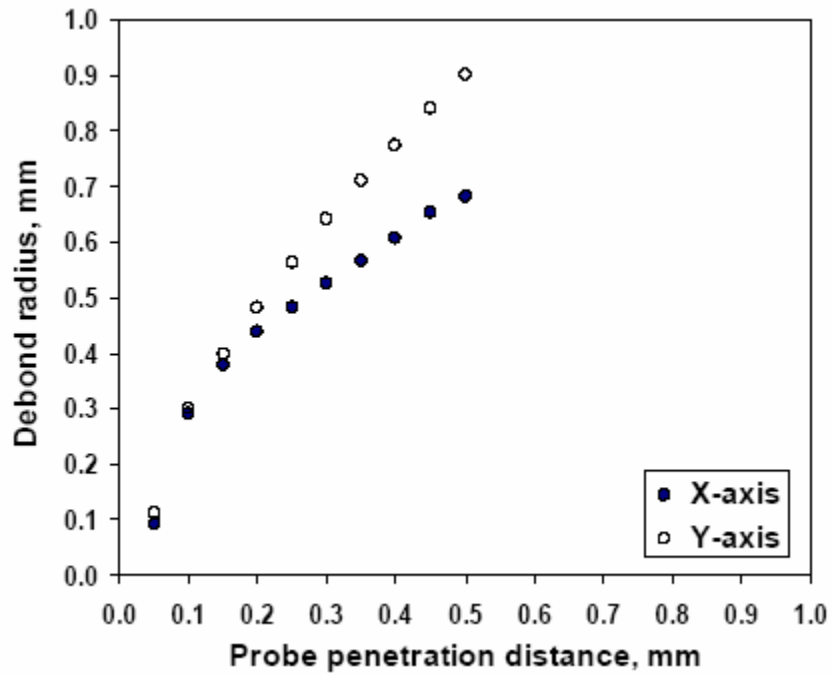


**Figure 6-1 Debond radii along (x-axis) and perpendicular (y-axis) to probe direction versus probe penetration distance measured for a debond in model epoxy/Si bonded specimen under dry conditions. Coating thickness is 75  $\mu\text{m}$ .**

(Reprinted from [1], with permission from author)

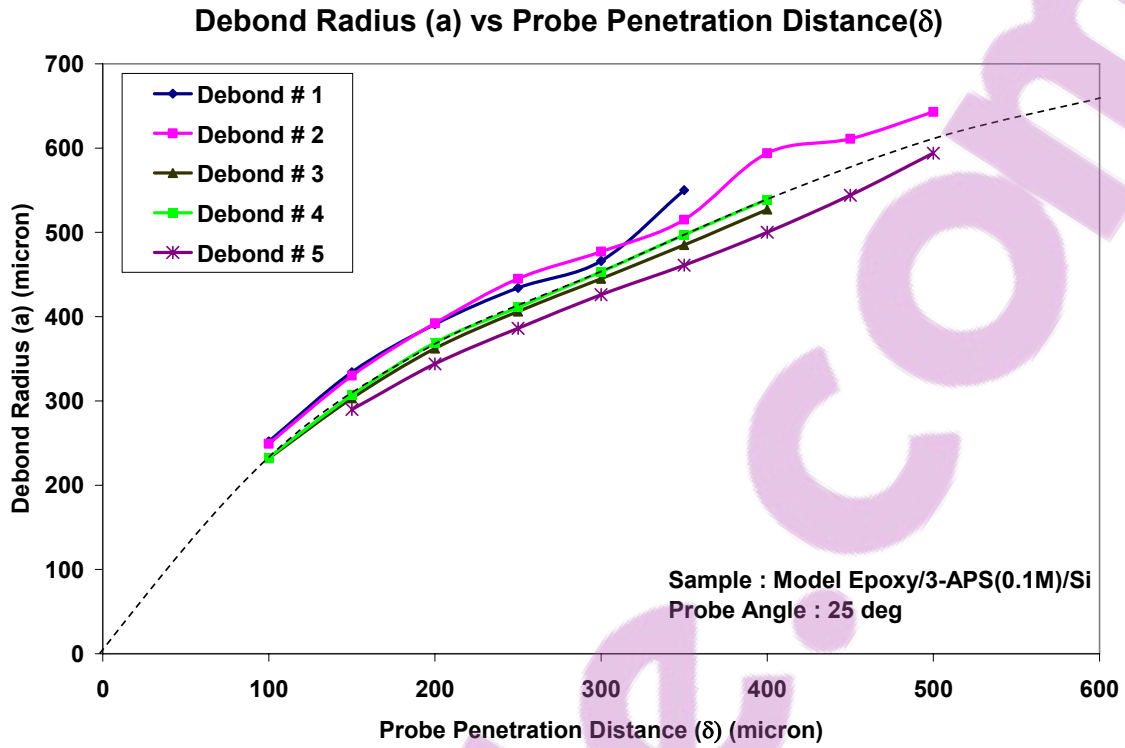


**Figure 6-2 Plots of debond radius (a) along the probe direction (x-axis) as a function of probe penetration distance ( $\delta$ ) for the coating (70 $\mu$ m)/Si substrate specimen and using a probe angle of 25°**

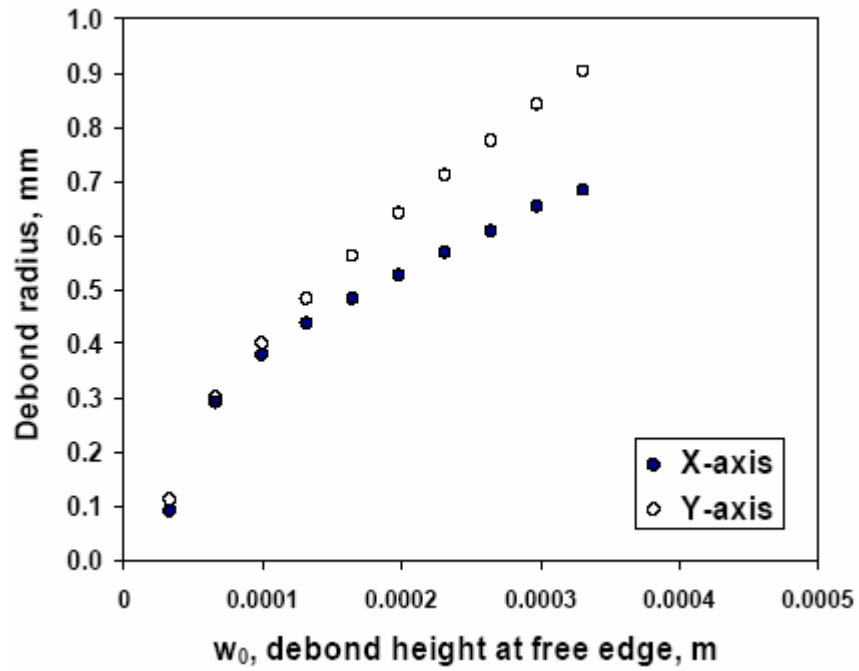


**Figure 6-3 Debond radii along (x-axis) and perpendicular (y-axis) to probe direction versus  $w_0$ , the debond height at the free edge of the coating measured for a debond in model epoxy/ Si bonded specimen under dry conditions. Coating thickness is 75 $\mu$ m.**

**(Reprinted from [1], with permission from author)**

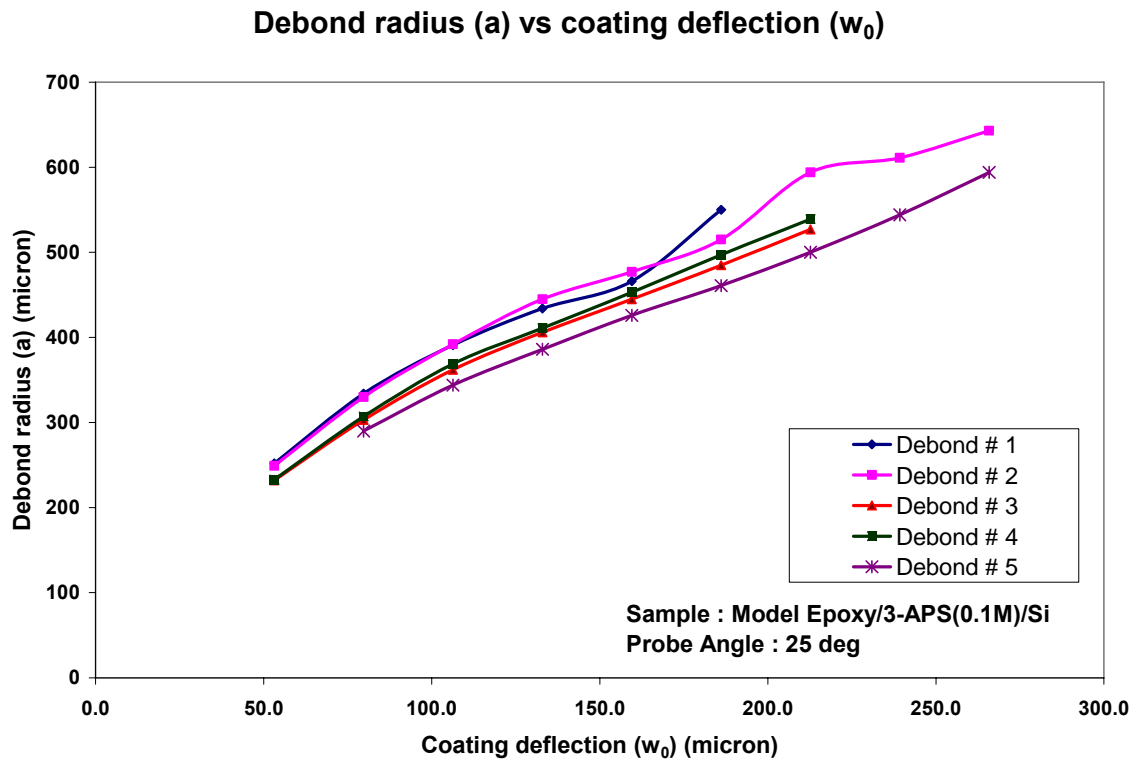


**Figure 6-4 Plots of debond radius (a) as a function of coating deflection ( $w_0$ ) for the epoxy coating (70 $\mu$ m)/Si substrate specimen and using a probe angle of 25°; h is the coating thickness**

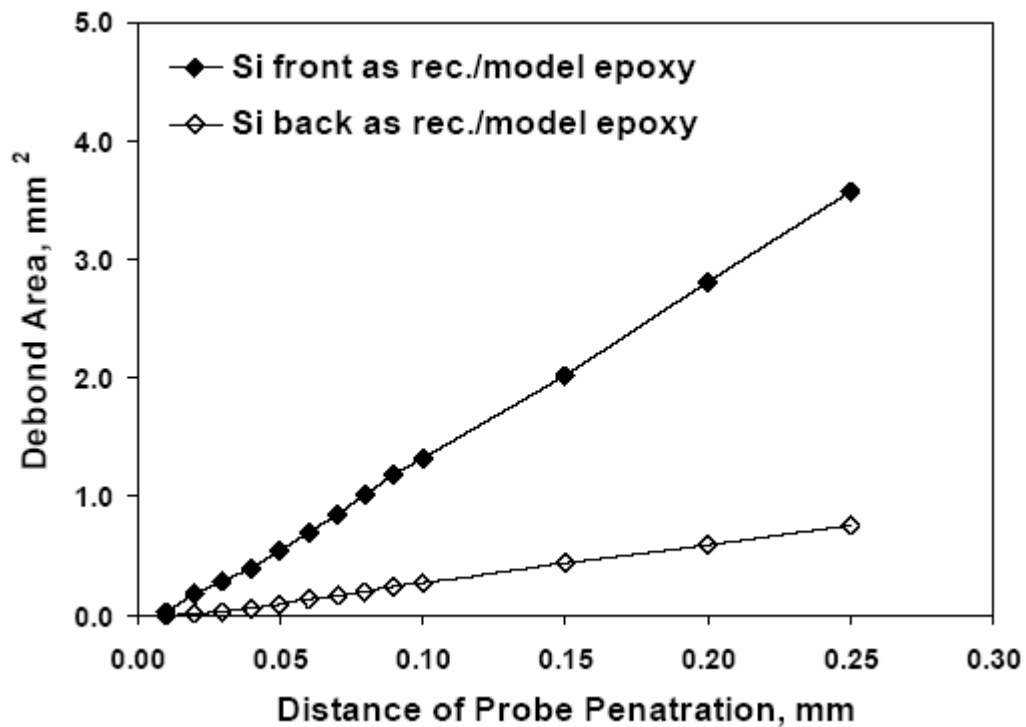


**Figure 6-5 Debond area as a function of probe penetration distance for a model epoxy coated as-received Si front side and back side specimens tested under dry conditions**

**(Reprinted from [1], with permission from author)**

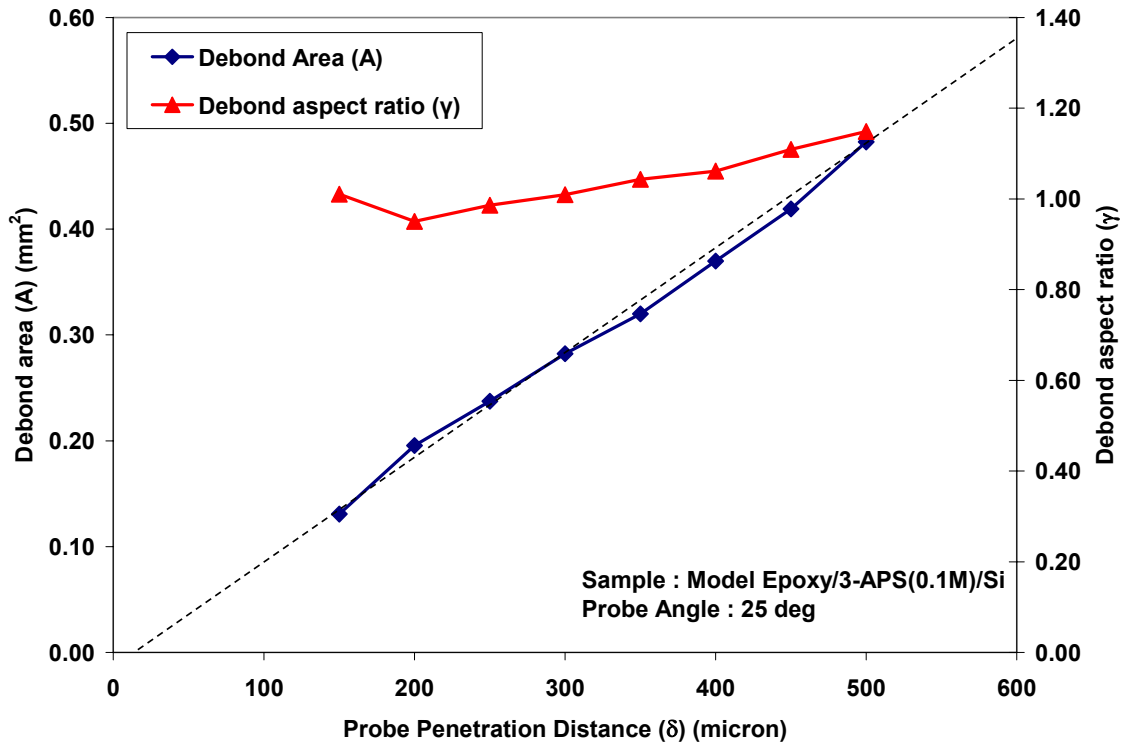


**Figure 6-6 Plots of debond area (A) and debond aspect ratio ( $\gamma$ ) as a function of probe penetration distance ( $\delta$ ) for the coating (70 $\mu\text{m}$ )/Si substrate specimen using a probe angle of 25°**

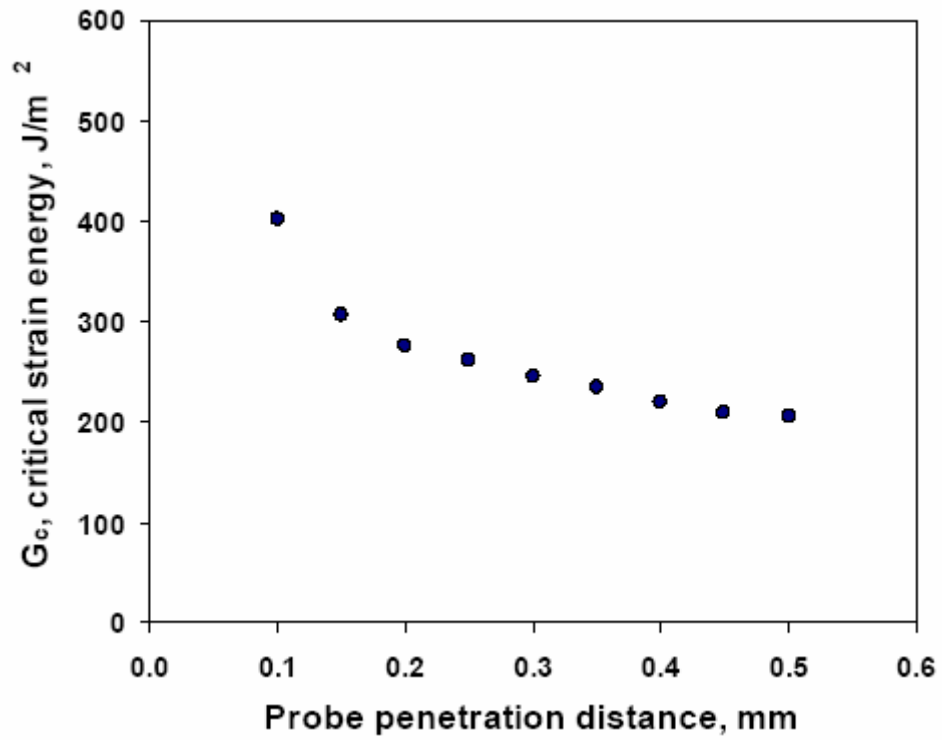


**Figure 6-7 Interfacial fracture energy ( $G_c$ ) versus probe penetration distance for a debond in the model epoxy/ Si specimen under dry conditions. Coating thickness is 80  $\mu\text{m}$**

**(Reprinted from [1], with permission from author)**

### Interfacial Fracture Energy ( $G_c$ ) vs Debond Radius (a)

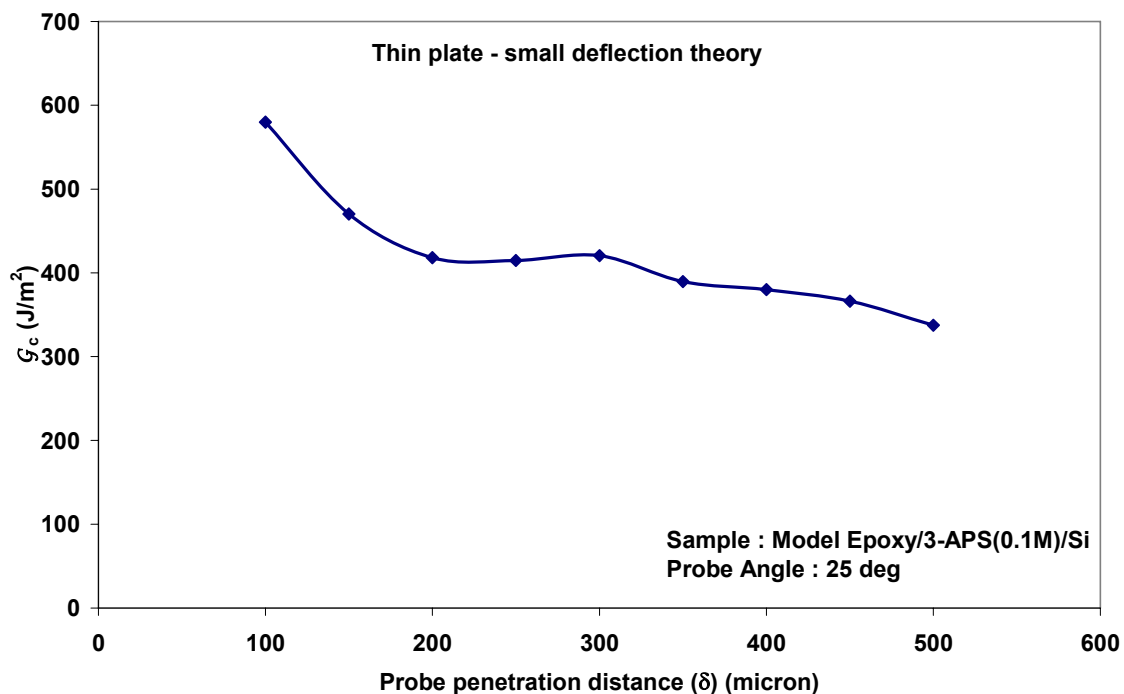


**Figure 6-8 Plot of interfacial fracture energy ( $G_c$ ) vs. probe penetration distance ( $\delta$ ) calculated using thin plate – small deflection theory. The  $G_c$  values shown were averaged over five different debonds which were created using the probe test technique in an epoxy coating(70  $\mu\text{m}$ )/Si substrate specimen and using a probe angle of 25°.**

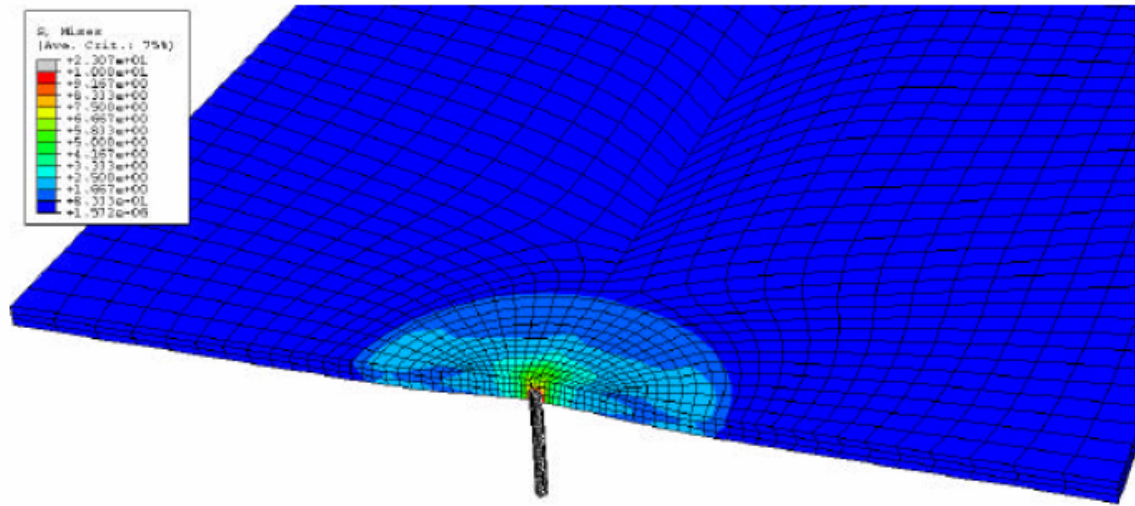


**Figure 6-9 Graphical representation of von Mises stresses of an edge-loaded thin film**

(Reprinted from [2], with permission from author)

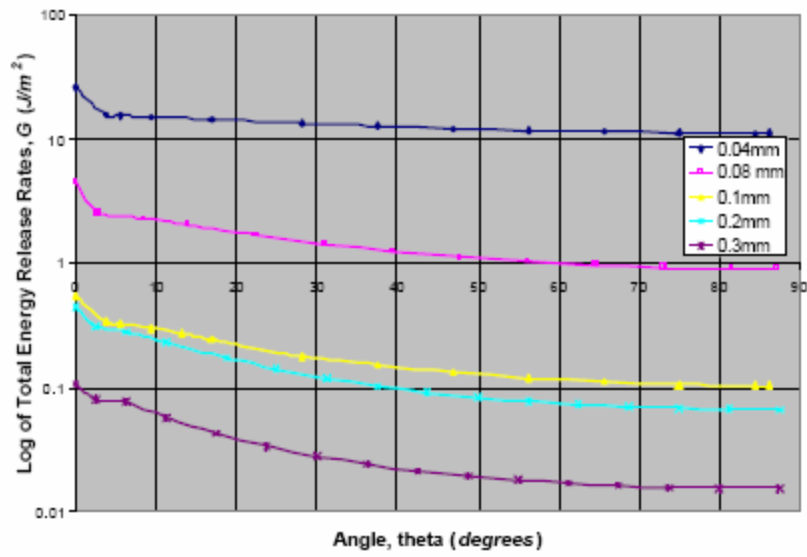


**Figure 6-10 Plot of  $\log$  of  $G_{tot}$  along the crack front with varying debond radius and no residual stress**  
**(Reprinted from [2], with permission from author)**

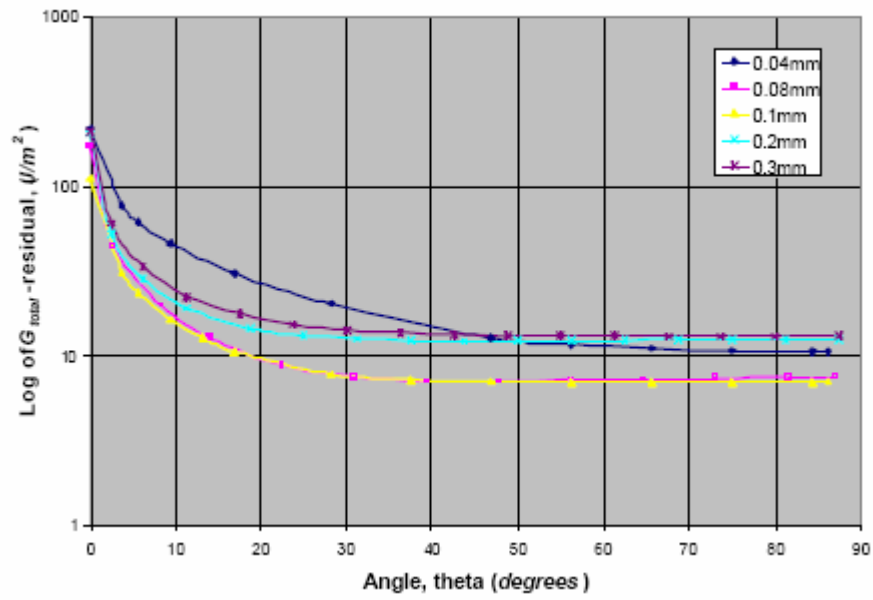


**Figure 6-11 Plot of log of  $G_{tot}$  along the crack front with varying debond radius and residual stress**

**(Reprinted from [2], with permission from author)**

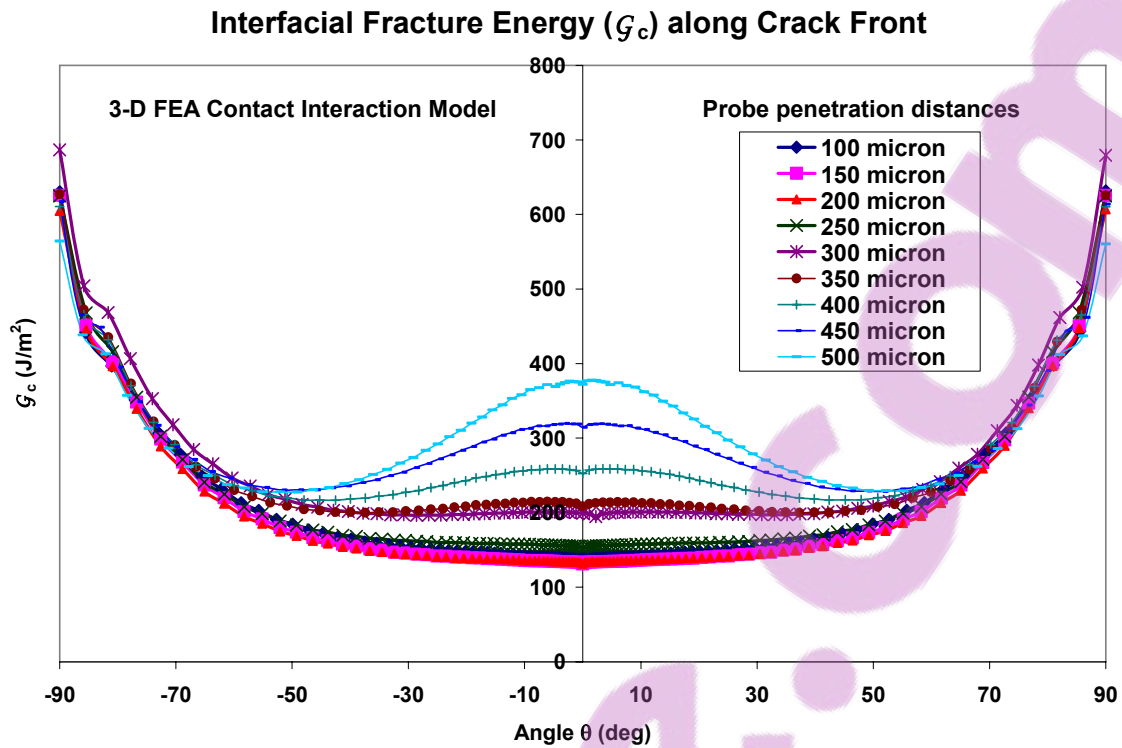
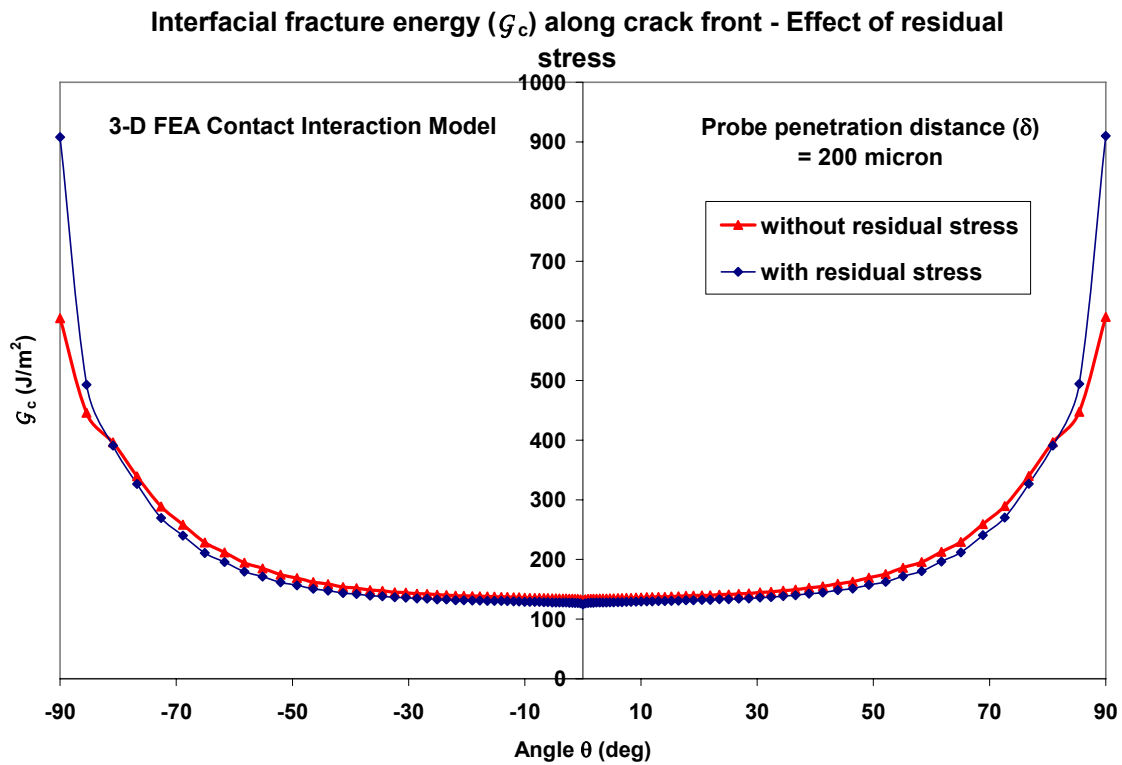
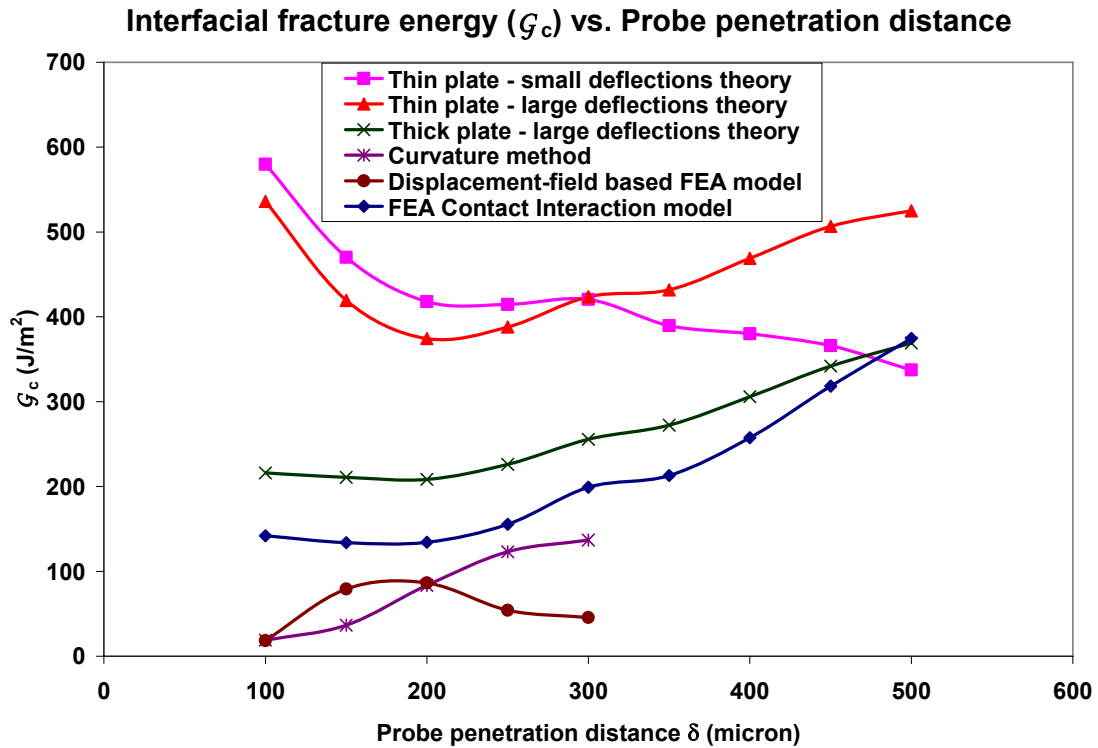


Figure 6-12 Plots of interfacial fracture energy,  $G_c$  along the crack front ( $-90^\circ \leq \theta \leq 90^\circ$ ) calculated using finite element contact interaction method. The debond was created using the probe test technique in an epoxy coating ( $70 \mu m$ )/Si substrate specimen and a probe angle of  $25^\circ$



**Figure 6-13 Plots of interfacial fracture energy,  $G_c$  along the crack front ( $-90^\circ \leq \theta \leq 90^\circ$ ) for  $\delta = 200$  micron calculated with and without the presence of residual stress in the finite element contact interaction model. The debond was created using the probe test technique in an epoxy coating( $70 \mu\text{m}$ )/Si substrate specimen and a probe angle of  $25^\circ$**



**Figure 6-14 Comparison of interfacial fracture energy ( $G_c$ ) calculated using different analytical and FEA based techniques in the present research. The debonds were created using the probe test technique in an epoxy coating(70  $\mu\text{m}$ )/Si substrate specimen and using a probe angle of  $25^\circ$**

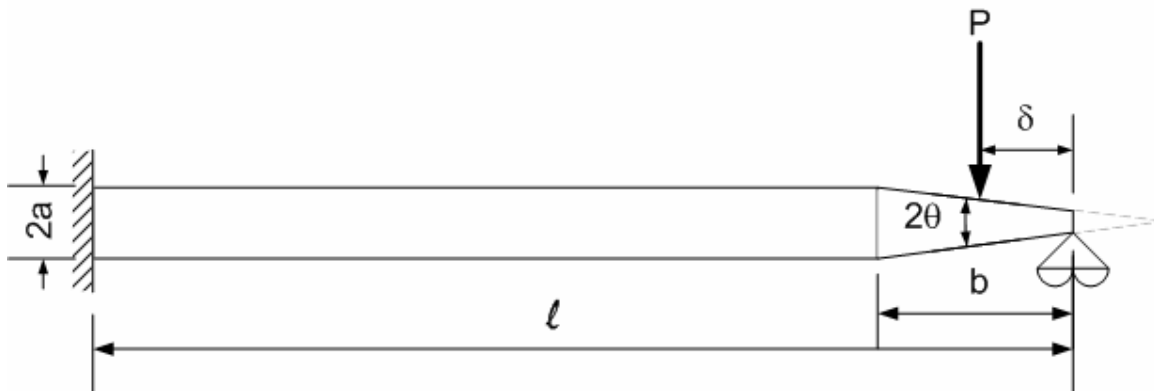


**Figure 6-15** A schematic illustration of the loading and boundary conditions on the probe in contact with the coating and the substrate in the probe test experiment.  $l$  is the total length,  $b$  is the taper length,  $a$  is the shank radius,  $\theta$  is the half cone angle of the probe;  $\delta$  is the distance from the probe tip to the point of contact with the coating

## 6.7 References

1. Xu, D., *Durability and adhesion of a model epoxy adhesive bonded to modified silicon substrates*, in *Chemistry*. 2004, University Libraries Virginia Polytechnic Institute and State University: Blacksburg, Va.
2. Mount, K.P., *Finite element analysis of probe induced delamination of a thin film at an edge interface*, in *Mechanical Engineering*. 2003, University Libraries Virginia Polytechnic Institute and State University: Blacksburg, Va.

## Appendix A

```
% MATLAB script to calculate interfacial fracture energy using Curvature Method

% Identify crack front from the experimental debond profile
clear all;
close all;

% User defined inputs
%Wyko data filename
wyko_file='ppd300';

% Coating Properties
thickness = 70e-6;
E_film = 2.7e9;
poisson=0.32;
D = (E_film * thickness^3)/(12*(1-poisson^2));

% Degree of polynomial for curve fitting at crack front
degree_fit=9;

% Threshold z for ignoring data values (In micron)
threshold = 1.0;

% Read Data from Wyko file
fid_wyko=fopen(strcat(wyko_file, '.asc'), 'r');

flag=true;
count=0;
pos(1)=0;
pos(2)=-1;

%Read parameters from Wyko file
while (flag)
    dataline=fgetl(fid_wyko);
    count=count+1;
    if (strncmpi(dataline, 'pixel_size', 10))
        [a1, a2, a3, pixel_size(1,1)]=strread(dataline, '%s %f %f %f', 'delimiter', ',');
        pixel_size(1,1)=pixel_size(1,1)*1000;
    end
    if (strncmpi(dataline, 'aspect', 6))
        [a1, a2, a3, aspect]=strread(dataline, '%s %f %f %f', 'delimiter', ',');
    end
    if (strncmpi(dataline, 'wavelength', 10))
        [a1, a2, a3, wavelength]=strread(dataline, '%s %f %f %f', 'delimiter', ',');
    end
    if (strncmpi(dataline, 'mult', 4))
        [a1, a2, a3, mult]=strread(dataline, '%s %f %f %f', 'delimiter', ',');
        mult=mult*1000;
    end
    a1 = sscanf(dataline, '%c', 1);
    if ((length(str2num(a1))>0) && (pos(1)==0))
        pos(1)=count-1;
    end
    if (strncmpi(dataline, 'intensity', 9))
        pos(2)=count-1;
        flag=false;
    end
    if feof(fid_wyko)
        flag=false;
    end
end
if pos(2) < 0
    pos(2) = pos(1)-1;
end
fclose(fid_wyko);

% Read [xyz] data from file
[x_pixel, y_pixel, z_pixel] = textread(strcat(wyko_file, '.asc'), '%f,%f,%s', pos(2)-
pos(1), 'headerlines', pos(1));
```

```

%Remove bad data
count=0;
size_x = length(x_pixel);
pixel_size(2,1) = pixel_size(1,1) * aspect;
threshold = (threshold*mul t)/wavelength; % Convert threshold value from micron to
waves

for i = 1: size_x
    if (length(str2num(z_pixel{i})) > 0) && (str2num(z_pixel{i}) > threshold)
        count=count+1;
        x(count, 1) = x_pixel(i)*pixel_size(1, 1);
        y(count, 1) = y_pixel(i)*pixel_size(2, 1);
        z(count, 1) = ((str2num(z_pixel{i}) - threshold)*wavelength/mul t);
    end
end

% Plot debond profile : [x y z] data
figure;
plot3(x, y, z, '.');
title(strcat('Debond Profile - ', wyko_file));
xlabel('x (micron)');
ylabel('y (micron)');
zlabel('z (micron)');
saveas(gcf, strcat('debond_profile_', wyko_file, '.fig'));

% Clear these variables since no longer needed
clear x_pixel y_pixel z_pixel a1 a2 a3 pos threshold mul t aspect wavelength
dataline;

% Identify Crack Front in experimental data file
count=0;
size_x=length(x);
for i = 1: size_x-1
    if (x(i)~=x(i+1))
        count=count+1;
        crack_front(count, 1)=x(i+1);
        crack_front(count, 2)=y(i+1);
    end
end
for i = size_x-1: -1: 1
    if (x(i)~=x(i+1))
        count=count+1;
        crack_front(count, 1)=x(i);
        crack_front(count, 2)=y(i);
    end
end

% Find center point of crack front
size_x = length(crack_front);
mid_point(1) = (crack_front(1, 1) + crack_front(size_x, 1))/2;
mid_point(2) = median(crack_front(:, 2));

% Angular locations of crack front points
count=0;
for i = 2: size_x-1
    theta = 180*(atan((crack_front(i, 2)-mid_point(2))/(crack_front(i, 1)-
mid_point(1))))/pi;
    if abs(theta)<60
        count=count+1;
        radi(count, 1) = sqrt((crack_front(i, 1)-mid_point(1))^2 +
(crack_front(i, 2)-mid_point(2))^2);
        angle(count, 1) = 180*(atan((crack_front(i, 2)-
mid_point(2))/(crack_front(i, 1)-mid_point(1))))/pi;
    end
end

% Plot experimental crack front
figure;
plot(crack_front(:, 1), crack_front(:, 2), 'r', 'MarkerSize', 12);
title(strcat('Crack Front - ', wyko_file));
xlabel('x (micron)');
ylabel('y (micron)');
set(gca, 'DataAspectRatio', [1 1 1]);
hold on;
plot([mid_point(1) max(crack_front(:, 1))], [mid_point(2) mid_point(2)], 'k');

clear crack_front ;

% Analytical Equation Fit to crack front --- Using Curve Fitting Toolbox
ltype=strcat('poly', num2str(degree_fit));

```

```

ftype=fittype(ltype);
opts=fitoptions(ltype, 'Normalize', 'on', 'Robust', 'Bisquare');
[fresult,gof] = fit(angle, radii, ftype, opts);

for i =1:(degree_fit+1)
    r.type = '.';
    r.subs = strcat('p', num2str(i));
    fit_coeff(i)=subsref(fresult, r);
end

r=datastats(angle);
mu(1)=r.mean;
mu(2)=r.std;

% Crack Front using Polynomial Fit Equation
count=0;
for i = -60:5:60
    count=count+1;
    r = polyval(fit_coeff, i, [], mu);
    crack_front(count, 1)= r*cos(deg2rad(i))+ mid_point(1);
    crack_front(count, 2)= r*sin(deg2rad(i))+ mid_point(2);
    crack_front(count, 3) = i;
end

% Plot Analytical fit to crack front
plot(crack_front(:, 1), crack_front(:, 2), '-b', 'LineWidth', 2);
hold off;
saveas(gcf, strcat('crack_front_', wyko_file, '.fig'));

% Clear these variables since no longer needed
clear r;

% Curvature Method
% Isolate Debond Profile along radial direction
figure;
size_x = length(crack_front);
for i=1:size_x
    % disp('Iteration #');
    % disp(i);

    % Equation of line between midpoint and point on crack front
    a=crack_front(i, 2)-mid_point(2);
    b=-1*(crack_front(i, 1)-mid_point(1));
    c=mid_point(2)*crack_front(i, 1)-crack_front(i, 2)*mid_point(1);

    % Calculate debond size
    debond_size(i, 1)=sqrt((crack_front(i, 1)-mid_point(1))^2 + (crack_front(i, 2)-
mid_point(2))^2);

    % Choose points along debond profile
    count=0;
    for j = 1: length(x)

        % Check if the point lies inside the crack front
        r = sqrt((x(j)-mid_point(1))^2 + (y(j)-mid_point(2))^2);
        theta = 180*(atan(y(j)-mid_point(2))/(x(j)-mid_point(1)))/pi;
        if (polyval(fit_coeff, theta, [], mu)-r) > 0

            % Perpendicular distance of point from line
            distance(1, 1)=abs((a*x(j)+b*y(j)+c)/sqrt(a^2+b^2));

            %Parallel distance of point from crack front point
            distance(2, 1)= sqrt((x(j)-crack_front(i, 1))^2 + (y(j)-
crack_front(i, 2))^2);

            % Line width = 2 micron and 50 % of debond size
            if ((distance(1, 1) < 2.0) && (distance(2, 1)<=0.5*debond_size(i, 1)))
                count=count+1;
                profile(count, 1)=x(j);
                profile(count, 2)=y(j);
                profile(count, 3)=z(j);
                profile_r(count, 1)=distance(2, 1);
                profile_z(count, 1)=z(j);
            end
        end
    end
end

% Plot 3D cropped debond profile
plot3(profile(:, 1), profile(:, 2), profile(:, 3), '.', 'MarkerSize', 12);
hold on;

```

```

% Analytical Equation Fit to debond profile --- Using Curve Fitting Toolbox
% Method 1 using z vs r (only displacement at crack tip is zero)
ftype=fittype('poly2');
opts=fitoptions('poly2','Robust','on');
opts.Lower = [-Inf -Inf 0];
opts.Upper = [Inf Inf 0];
[fresult1,gof1] = fit(profile_r, profile_z, ftype, opts);
curvature(i,1) = 2*fresult1.p1*1e6;
coeff(i,1)=fresult1.p1;
coeff(i,2)=fresult1.p2;
coeff(i,3)=fresult1.p3;

% Analytical Equation Fit to debond profile --- Using Curve Fitting Toolbox
% Method 2 using z vs r and clamped BC's (slope and displacement at
% crack tip is zero
ftype=fittype('poly2');
opts=fitoptions('poly2','Robust','off');
opts.Lower = [-Inf 0 0];
opts.Upper = [Inf 0 0];
[fresult2,gof2] = fit(profile_r, profile_z, ftype, opts);
curvature(i,2) = 2*fresult2.p1*1e6;
coeff(i,4)=fresult2.p1;
coeff(i,5)=fresult2.p2;
coeff(i,6)=fresult2.p3;

if (crack_front(i,3)==0)
    profile_data.r=profile_r;
    profile_data.z=profile_z;
    profile_data.result1=fresult1;
    profile_data.gof1=gof1;
    profile_data.result2=fresult2;
    profile_data.gof2=gof2;

%         % Plot 2D debond profile (z vs r) at theta = 0
%         figure;
%         plot(fresult, profile_a_r, profile_z);
%         xlabel('r (micron)');
%         ylabel('Deflection z (micron)');
end

% Calculate Fracture Energy using curvature method
fracture_energy_curvature(i,1) = crack_front(i,3);
fracture_energy_curvature(i,2) = 0.5 * D * curvature(i,1)^2;
fracture_energy_curvature(i,3) = 0.5 * D * curvature(i,2)^2;

%     input('Press return to continue');

clear profile profile_r profile_a_r profile_z;
end

title(strcat('Cropped Debond Profile - ', wyko_file));
xlabel('x (micron)');
ylabel('y (micron)');
zlabel('z (micron)');
saveas(gcf, strcat('cropped_debond_profile_', wyko_file, '.fig'));

figure;
plot(fracture_energy_curvature(:,1), fracture_energy_curvature(:,2), 'bo');
title(strcat('Interfacial Fracture Energy along Crack Front - ', wyko_file));
xlabel('Angular Location');
ylabel('G (J/m^2)');
legend('Method 1 using z vs r and zero displacement at crack tip');
grid on;

figure;
plot(fracture_energy_curvature(:,1), fracture_energy_curvature(:,3), 'bo');
title(strcat('Interfacial Fracture Energy along Crack Front - ', wyko_file));
xlabel('Angular Location');
ylabel('G (J/m^2)');
legend('Method 2 using z vs r and clamped BCs ');
grid on;

save(strcat('workspace_variables_', wyko_file));

```

## Appendix B

```

% MATLAB script to read the debond profile measurement data obtained using the
% WYKO profiler and identify the crack front from the experimental data
clear all;
close all;

% User defined inputs
%Wyko data filename
wyko_file='ppd150';

% Coating Properties
thickness = 70; % Micron
E_film = 2.7e3; % X 10E-3 GPa - Displacement is in micron
poisson=0.32;

% Degree of polynomial for curve fitting at crack front
degree_fit=9;

% Threshold z for ignoring data values (in micron)
threshold = 2;

% Read Data from Wyko file
fid_wyko=fopen(strcat(wyko_file, '.asc'), 'r');

flag=true;
count=0;
pos(1)=0;
pos(2)=-1;

%Read parameters from Wyko file
while (flag)
    dataline=fgetl(fid_wyko);
    count=count+1;
    if (strncmpi(dataline, 'pixel_size', 10))
        [a1, a2, a3, pixel_size(1,1)]=strread(dataline, '%s %f %f %f', 'delimiter', ',');
        pixel_size(1,1)=pixel_size(1,1)*1000;
    end
    if (strncmpi(dataline, 'aspect', 6))
        [a1, a2, a3, aspect]=strread(dataline, '%s %f %f %f', 'delimiter', ',');
    end
    if (strncmpi(dataline, 'wavelength', 10))
        [a1, a2, a3, wavelength]=strread(dataline, '%s %f %f %f', 'delimiter', ',');
    end
    if (strncmpi(dataline, 'mult', 4))
        [a1, a2, a3, mult]=strread(dataline, '%s %f %f %f', 'delimiter', ',');
        mult=mult*1000;
    end
    a1 = sscanf(dataline, '%c', 1);
    if ((length(str2num(a1))>0) && (pos(1)==0))
        pos(1)=count-1;
    end
    if (strncmpi(dataline, 'intensity', 9))
        pos(2)=count-1;
        flag=false;
    end
    if feof(fid_wyko)
        flag=false;
    end
end
if pos(2) < 0
    pos(2) = pos(1)-1;
end
fclose(fid_wyko);

% Read measurement [xyz] data from file
[x_pixel, y_pixel, z_pixel] = textread(strcat(wyko_file, '.asc'), '%f, %f, %s', pos(2)-
pos(1), 'headerlines', pos(1));

%Remove bad data
count=0;
size_x = length(x_pixel);
pixel_size(2,1) = pixel_size(1,1) * aspect;

```

```

threshold = (threshold*mul t)/wavel ength; % Convert threshol d val ue from mi cron to
waves
for i = 1: si ze_x
    if (l ength(str2num(z_pi xel {i})) > 0) && (str2num(z_pi xel {i}) > threshol d)
        count=count+1;
        x(count, 1) = x_pi xel (i)*pi xel _si ze(1, 1);
        y(count, 1) = y_pi xel (i)*pi xel _si ze(2, 1);
        z(count, 1)=(str2num(z_pi xel {i})- threshol d)*wavel ength/mul t;
    end
end

% Plot debond profil e : [x y z] data
fi gure;
plot3(x, y, z, ' . ');
ti tle(strcat(' Debond Profil e - ', wyko_fi le));
xl abel (' x (mi cron) ');
yl abel (' y (mi cron) ');
zl abel (' z (mi cron) ');
saveas(gcf, strcat(' debond_profi le_', wyko_fi le, '. fi g' ));

% Clear these vari ables si nce no longer needed
clear x_pi xel y_pi xel z_pi xel a1 a2 a3 pos threshol d mul t aspect wavel ength
dataLi ne;

% Iden ti fy Crack Front in experi mental data fi le
count=0;
si ze_x=l ength(x);
for i = 1: si ze_x-1
    if (x(i)~=x(i+1))
        count=count+1;
        crack_front(count, 1)=x(i+1);
        crack_front(count, 2)=y(i+1);
    end
end
for i = si ze_x-1: -1: 1
    if (x(i)~=x(i+1))
        count=count+1;
        crack_front(count, 1)=x(i);
        crack_front(count, 2)=y(i);
    end
end

% Find center poi nt of crack front
si ze_x = l ength(crack_front);
mi d_poi nt(1) = (crack_front(1, 1) + crack_front(si ze_x, 1))/2;
mi d_poi nt(2) = mean(crack_front(:, 2));

% Angular l ocati ons of crack front poi nts
radi i(1, 1) = sqrt((crack_front(1, 1)-mi d_poi nt(1))^2 + (crack_front(1, 2)-
mi d_poi nt(2))^2);
angl e(1, 1)=-90;

for i = 2: si ze_x-1
    radi i(i, 1) = sqrt((crack_front(i, 1)-mi d_poi nt(1))^2 + (crack_front(i, 2)-
mi d_poi nt(2))^2);
    angl e(i, 1) = 180*(atan((crack_front(i, 2)-mi d_poi nt(2))/(crack_front(i, 1)-
mi d_poi nt(1))))/pi ;
end

radi i(si ze_x, 1) = sqrt((crack_front(si ze_x, 1)-mi d_poi nt(1))^2 +
(crack_front(si ze_x, 2)-mi d_poi nt(2))^2);
angl e(si ze_x, 1)=90;

% Plot experi mental crack front
fi gure;
plot(crack_front(:, 1), crack_front(:, 2), ' . r', ' MarkerSi ze', 12);
ti tle(strcat(' Crack Front - ', wyko_fi le));
xl abel (' x (mi cron) ');
yl abel (' y (mi cron) ');
set(gca, ' DataAspectRati o', [1 1 1]);
hol d on;
plot([mi d_poi nt(1) max(crack_front(:, 1))], [mi d_poi nt(2) mi d_poi nt(2)], ' : k' );

clear crack_front ;

% Analytical Equati on Fit to crack front --- Usi ng Curve Fi tti ng Tool box
l i type=strcat(' pol y', num2str(degree_fi t));
fi ttype=fi ttype(l i type);
opt s=fi topti ons(l i type, ' Normal i ze', ' on', ' Robust', ' Bi square');

```

```

[fresult,gof] = fit(angle, radii, ftype, opts);
for i =1:(degree_fit+1)
    r.type = '.';
    r.subs = strcat('p', num2str(i));
    fit_coeff(i)=subsref(fresult,r);
end

r=datastats(angle);
mu(1)=r.mean;
mu(2)=r.std;

% Crack Front using Polynomial Fit Equation
count=0;
for i = -90:1:90
    count=count+1;
    r = polyval(fit_coeff, i, [], mu);
    crack_front(count, 1) = r*cos(deg2rad(i))+ mi_d_point(1);
    crack_front(count, 2) = r*sin(deg2rad(i))+ mi_d_point(2);
    crack_front(count, 3) = i;
end

% Plot Analytical fit to crack front
plot(crack_front(:, 1), crack_front(:, 2), '-b', 'LineWidth', 2);
hold off;
saveas(gcf, strcat('crack_front_', wyko_file, '.fig'));

% Clear these variables since no longer needed
clear r;

% Save debond measurement data and Curve Fit Equation parameters
save(strcat('debond_data_', wyko_file), 'x', 'y', 'z', 'fit_coeff', 'mu', 'mi_d_point');

% Min no of rows inside crack front
disp('Minimum no of rows inside crack front = ');
disp((max(x)-mi_d_point(1))/pixel_size(1, 1));

```

## Appendix C

```
% MATLAB script to generate input script for ABAQUS finite element model using data
% from WYKO profiler measurements
clear all;
close all;

% User defined inputs
%Wyko data filename
wyko_file='ppd200';

% Coating Properties
thickness = 70; % Micron
E_film = 2.7e3; % X 10E-3 GPa
poisson=0.32;

% No of layers of elements
no_layers=10;
% No of rows of elements inside the crack front
no_rows(1)=30;
% No of rows of elements outside the crack front
no_rows(2)=10;
% Bias to the spacing of nodes inside the crack front
bias(1)=0.8;
% Bias to the spacing of nodes outside the crack front
bias(2)=0.2;
% Bias to the spacing of nodes normal to the crack front plane
bias(3)=0.4;

% No of layer of nodes (Using Element type C3D27R)
no_layers=2*no_layers + 1;

%No. of elements rows to ignore for displacement values
element_rows_ignore=8;

%No of contours for contour integral evaluation
no_contours=5;

%Abaqus Script File
fid_abaqus=fopen(strcat('probe_disp_fea_', wyko_file, '.inp'), 'w');

fprintf(fid_abaqus, '*Heading\n');
fprintf(fid_abaqus, '*Preprint, echo=NO, model=NO, history=NO, contact=NO\n');
fprintf(fid_abaqus, '*Node, input=mesh_%s.inp\n', wyko_file);
fprintf(fid_abaqus, '*Include, input=nodes_bonded_%s.inp\n', wyko_file);

% Load debond measurement data and crack front polynomial fit results using Curve
Fitting Toolbox
load(strcat('debond_data_', wyko_file, '.mat'));

% Crack Front using Fit Equation
count=0;
for i = -90:2:90
    count=count+1;
    r = polyval(fit_coeff, i, [], mu);
    crack_front(count, 1) = r*cos(deg2rad(i))+ mid_point(1);
    crack_front(count, 2) = r*sin(deg2rad(i))+ mid_point(2);
    crack_front(count, 3) = i;
end

% Clear these variables since no longer needed
clear r;

% Identify Bonded nodes on lower surface
fid_bonded = fopen(strcat('nodes_bonded_', wyko_file, '.inp'), 'w');
fprintf(fid_bonded, '*Nset, nset=nodes_bonded\n');

% Mesh Generation
fid_mesh = fopen(strcat('mesh_', wyko_file, '.inp'), 'w');
size_x = length(crack_front);
count=0;
```

```

n_z = (no_layers-3)/2;
interval_z=thickness/ (2* (1 - bias(3)^(n_z+1))/ (1 - bias(3)));
z_level=0;
% for k = 0: (thickness/(no_layers-1)): thickness
for k = 0: no_layers-1

    % Generate mesh inside crack front
    % Using quarter-point spacing at the crack tip

    m=0;
    n_r = (no_rows(1)-1);
    interval_r = 1/ ((2* (1 - bias(1)^(n_r+1))/ (1 - bias(1))))+1);

    % Create quarter point spacing above the crack front to
    % give square root singularity at crack tip
    if (k==1)
        z_level=0.5*z_level;
    end

    for j = 0 : 1: 2*no_rows(1)

        % Create quarter point spacing next to crack front to
        % give square root singularity at crack tip
        if (j==1)
            m=0.5 * m;
        end
        for i = 1 : size_x
            count=count+1;
            fprintf(fid_mesh,'%d, %f, %f, %f \n',count, (1-m) * crack_front(i,1) +
m*mid_point(1), (1-m) * crack_front(i,2) + m*mid_point(2), z_level);

            % Only the bottom layer of nodes is included in the mesh
            % matrix and also exclude mid-nodes
            if ((z_level==0)&& (mod(i,2)~=0)&&(mod(j,2)~=0))
                mesh(count,1)= count;
                mesh(count,2) = (1-m) * crack_front(i,1) + m*mid_point(1);
                mesh(count,3) = (1-m) * crack_front(i,2) + m*mid_point(2);
                mesh(count,4) = z_level;
            end
            % Add the node at crack front in the bottom layer to the bonded node
            if ((z_level==0) && (j==0))
                fprintf(fid_bonded,'%d \n', count);
            end

        end

        % Quarter point spacing next to crack front
        if (j==1)
            m=m/0.5;
        end

        m = m + interval_r * (bias(1)^n_r);
        if (mod(j,2)==1)
            n_r = n_r -1;
        end
    end

    % Count for the number of nodes per layer inside the crack front
    if z_level==0
        nodes_per_layer_in = count;
    end

    % Generate mesh outside crack front
    % Using quarter-point spacing at the crack tip

    m=0;
    n_r = (no_rows(2)-1);
    interval_r = 1/ ((2* (1 - bias(2)^(n_r+1))/ (1 - bias(2))))+1);
    for j = 1 : 1: 2*no_rows(2)
        m = m + interval_r * (bias(2)^n_r);

        % Create quarter point spacing next to crack front to
        % give square root singularity at crack tip
        if (j==1)
            m=0.5 * m;
        end
        for i = 1 : size_x
            count=count+1;

```

```

        fprintf(fid_mesh,'%d, %f, %f, %f \n',count, (1+m) * crack_front(i,1) -
m*mid_point(1), (1+m) * crack_front(i,2) - m*mid_point(2), z_level);

        % Only the bottom layer of nodes is included in the mesh matrix
        if (z_level==0)
            mesh(count,1)= count;
            mesh(count,2) = (1+m) * crack_front(i,1) - m*mid_point(1);
            mesh(count,3) = (1+m) * crack_front(i,2) - m*mid_point(2);
            mesh(count,4) = z_level;
        end

        % Add the node in the bottom layer to the bonded node list
        if (z_level==0)
            fprintf(fid_bonded,'%d \n', count);
        end

        % Quarter point spacing next to crack front
        if (j==1)
            m=m/0.5;
        end
        if (mod(j,2)==0)
            n_r = n_r - 1;
        end
    end

    % Count for the number of nodes per layer
    if z_level==0
        nodes_per_layer = count;
    end

    if (k==1)
        z_level =z_level /0.5;
    end

    z_level =z_level + interval_z * (bias(3)^n_z);
    if (mod(k,2)==1)
        n_z = n_z - 1;
    end

end

fclose(fid_bonded);
fclose(fid_mesh);

% Plot generated mesh with node numbers
figure;
plot(mesh(:,2),mesh(:,3),'.');
% text(mesh(:,2),mesh(:,3),num2str(mesh(:,1)));
set(gca,'DataAspectRatio',[1 1 1]);
title(strcat('Generated mesh - ',wyko_file));
xlabel('x (micron)');
ylabel('y (micron)');
saveas(gcf,strcat('mesh_',wyko_file,'.fig'));

% Generate Element Connectivity for the Inside mesh
% Element options

fprintf(fid_abaqus,'*Element, type=C3D27\n');
fprintf(fid_abaqus,'1, %d, 1, 3, %d, \n',2*length(crack_front)+1,
2*length(crack_front)+3);
fprintf(fid_abaqus,'%d, %d, %d, \n', 2*length(crack_front)+1+2*nodes_per_layer,
1+2*nodes_per_layer, 3+2*nodes_per_layer, 2*length(crack_front)+3+2*nodes_per_layer);
fprintf(fid_abaqus,'%d, 2, %d, %d, \n', length(crack_front)+1, length(crack_front)+3, 2*length(crack_front)+2);
fprintf(fid_abaqus,'%d, %d, %d, %d, \n', length(crack_front)+1+2*nodes_per_layer, length(crack_front)+3+2
*nodes_per_layer, 2*length(crack_front)+2+2*nodes_per_layer);
fprintf(fid_abaqus,'%d, %d, %d, %d, \n', 2*length(crack_front)+1+nodes_per_layer, 1+nodes_per_layer, 3+nodes_per_layer,
2*length(crack_front)+3+nodes_per_layer);
fprintf(fid_abaqus,'%d, \n', length(crack_front)+2+nodes_per_layer);
fprintf(fid_abaqus,'%d, %d, \n', length(crack_front)+2,
length(crack_front)+2+2*nodes_per_layer);
fprintf(fid_abaqus,'%d, %d, %d, %d \n', length(crack_front)+1+nodes_per_layer, 2+nodes_per_layer,
length(crack_front)+3+nodes_per_layer, 2*length(crack_front)+2+nodes_per_layer);

% Elgen options
fprintf(fid_abaqus,'*Elgen\n');
fprintf(fid_abaqus,'1, %d, 2, 1, %d, %d, %d, %d, %d, %d \n',0.5*(length(crack_front)-1), no_rows(1), 2*length(crack_front),

```

```

0.5*(length(crack_front)-1), (no_layers-1)/2, 2*nodes_per_layer,
0.5*(length(crack_front)-1)*no_rows(1));

% Generate Element Connectivity for the Outside mesh next to crack front
% Element options
fprintf(fid_abaqus, '*Element, type=C3D27\n');

fprintf(fid_abaqus, '500001, 1, %d, %d, 3,
\n', length(crack_front)+1+nodes_per_layer_in, length(crack_front)+3+nodes_per_layer_in);
fprintf(fid_abaqus, '%d, %d, %d, %d, \n', 1+2*nodes_per_layer,
length(crack_front)+1+2*nodes_per_layer+nodes_per_layer_in,
length(crack_front)+3+2*nodes_per_layer+nodes_per_layer_in, 3+2*nodes_per_layer);
fprintf(fid_abaqus, '%d, %d, %d, 2, \n', nodes_per_layer_in+1,
length(crack_front)+2+nodes_per_layer_in, 3+nodes_per_layer_in);
fprintf(fid_abaqus, '%d, %d, %d, %d, \n', 1+2*nodes_per_layer+nodes_per_layer_in,
length(crack_front)+2+2*nodes_per_layer+nodes_per_layer_in,
3+2*nodes_per_layer+nodes_per_layer_in, 2+2*nodes_per_layer);
fprintf(fid_abaqus, '%d, %d, %d, %d, \n',
1+nodes_per_layer, length(crack_front)+1+nodes_per_layer_in,
length(crack_front)+3+nodes_per_layer+nodes_per_layer_in, 3+nodes_per_layer);
fprintf(fid_abaqus, '%d, \n', 2+nodes_per_layer+nodes_per_layer_in);
fprintf(fid_abaqus, '%d, %d, \n', 2+nodes_per_layer_in,
2+2*nodes_per_layer+nodes_per_layer_in);
fprintf(fid_abaqus, '%d, %d, %d, %d \n', nodes_per_layer+nodes_per_layer_in+1,
length(crack_front)+2+nodes_per_layer+nodes_per_layer_in, 3+nodes_per_layer+nodes_per_layer_in, 2+nodes_per_layer);

% Eigen options for single layer of elements just outside the crack front
fprintf(fid_abaqus, '*Eigen \n');
fprintf(fid_abaqus, '500001, %d, 2, 1, 1, %d, %d, %d, %d, %d
\n', 0.5*(length(crack_front)-1), 2*length(crack_front), 0.5*(length(crack_front)-1),
(no_layers-1)/2, 2*nodes_per_layer, 0.5*(length(crack_front)-1));

% Generate Element Connectivity for the remaining Outside mesh
% Element options
fprintf(fid_abaqus, '*Element, type=C3D27\n');
fprintf(fid_abaqus, '1000001, %d, %d, %d, %d,
\n', nodes_per_layer_in+1+length(crack_front), 3*length(crack_front)+1+nodes_per_layer_in,
3*length(crack_front)+3+nodes_per_layer_in,
nodes_per_layer_in+3+length(crack_front));
fprintf(fid_abaqus, '%d, %d, %d,
\n', 1+2*nodes_per_layer+nodes_per_layer_in+length(crack_front), 3*length(crack_front)+1+2*nodes_per_layer+nodes_per_layer_in,
3*length(crack_front)+3+2*nodes_per_layer+nodes_per_layer_in,
3+2*nodes_per_layer+nodes_per_layer_in+length(crack_front));
fprintf(fid_abaqus, '%d, %d, %d, %d,
\n', 2*length(crack_front)+1+nodes_per_layer_in, 3*length(crack_front)+2+nodes_per_layer_in,
2*length(crack_front)+3+nodes_per_layer_in,
nodes_per_layer_in+2+length(crack_front));
fprintf(fid_abaqus, '%d, %d, %d, %d, \n',
2*length(crack_front)+1+2*nodes_per_layer+nodes_per_layer_in,
3*length(crack_front)+2+2*nodes_per_layer+nodes_per_layer_in,
2*length(crack_front)+3+2*nodes_per_layer+nodes_per_layer_in,
2+2*nodes_per_layer+nodes_per_layer_in+length(crack_front));
fprintf(fid_abaqus, '%d, %d, %d, %d, \n',
1+nodes_per_layer+nodes_per_layer_in+length(crack_front),
3*length(crack_front)+1+nodes_per_layer+nodes_per_layer_in,
3*length(crack_front)+3+nodes_per_layer+nodes_per_layer_in,
3+nodes_per_layer+nodes_per_layer_in+length(crack_front));
fprintf(fid_abaqus, '%d, \n',
2*length(crack_front)+2+nodes_per_layer+nodes_per_layer_in);
fprintf(fid_abaqus, '%d, %d, \n', 2*length(crack_front)+2+nodes_per_layer_in,
2*length(crack_front)+2+2*nodes_per_layer+nodes_per_layer_in);
fprintf(fid_abaqus, '%d, %d, %d, %d \n',
2*length(crack_front)+1+nodes_per_layer+nodes_per_layer_in,
3*length(crack_front)+2+nodes_per_layer+nodes_per_layer_in,
2*length(crack_front)+3+nodes_per_layer+nodes_per_layer_in,
2+nodes_per_layer+nodes_per_layer_in+length(crack_front));

% Eigen options
fprintf(fid_abaqus, '*Eigen \n');
fprintf(fid_abaqus, '1000001, %d, 2, 1, %d, %d, %d, %d, %d, %d
\n', 0.5*(length(crack_front)-1), no_rows(2)-1, 2*length(crack_front),
0.5*(length(crack_front)-1), (no_layers-1)/2, 2*nodes_per_layer,
0.5*(length(crack_front)-1)*(no_rows(2)-1));

% Correlate Displacement Boundary Conditions with generated nodes numbers
fid_displacement=fopen(strcat('displacement_', wyko_file, '.inp'), 'w');
fprintf(fid_displacement, '*Boundary \n');

```

```

size_x=length(x);
displaced_node=zeros(1,3);
count=0;
for i = 1:size_x
    flag=true;

    % Check if the point (x,y) does not lie on the crack front
    r = sqrt((x(i)-mid_point(1))^2 + (y(i)-mid_point(2))^2);
    theta = 180*(atan(y(i)-mid_point(2))/(x(i)-mid_point(1)))/pi;
    if (polyval(fit_coeff, theta, [], mu)-r) > 0

        %Search for nearest node in the mesh
        pos=dsearchn(mesh(:,2:4), [x(i,1) y(i,1) 0]);

        % Check if the node lies inside the crack front
        r1 = sqrt((mesh(pos,2)-mid_point(1))^2 + (mesh(pos,3)-mid_point(2))^2);
        theta1 = 180*(atan((mesh(pos,3)-mid_point(2))/(mesh(pos,2)-
mid_point(1))))/pi;

        if (((polyval(fit_coeff, theta1, [], mu)-r1) > 0) && (mesh(pos,1) >
(2*element_rows_ignore+1)*length(crack_front)))

            d=sqrt((mesh(pos,2)-x(i))^2 + (mesh(pos,3)-y(i))^2);

            % Check if the node is already exists in the list
            for j=1:size(displaced_node,1)
                if (displaced_node(j,1)== mesh(pos,1))
                    displaced_node(j,2)=displaced_node(j,2) + z(i) * d;
                    displaced_node(j,3)=displaced_node(j,3) + d;
                    flag=false;
                end
            end
            if (flag)
                count=count+1;
                displaced_node(count,1) = mesh(pos,1);
                displaced_node(count,2)= z(i) * d;
                displaced_node(count,3)= d;
            end
        end
    end
end

size_x=length(displaced_node);
for i=1:2:no_layers
    for j = 1: size_x
        fprintf(fid_displacement, '%d, 3, 3, %f \n', displaced_node(j,1)+(i-
1)*nodes_per_layer, (displaced_node(j,2)/displaced_node(j,3)));
    end
end

fclose(fid_displacement);

% Clear these variables since no longer needed
clear r theta r1 theta1;

fprintf(fid_abaqus, '*El set, el set=all_elements, generate \n');
fprintf(fid_abaqus, '1, 2000000, 1 \n');
fprintf(fid_abaqus, '** Section: Coating \n');
fprintf(fid_abaqus, '*Solid Section, el set=all_elements, material=Epoxy \n');
fprintf(fid_abaqus, '1, \n');
fprintf(fid_abaqus, '** MATERIAL DEFINITION \n');
fprintf(fid_abaqus, '*Material, name=Epoxy \n');
fprintf(fid_abaqus, '*Elastic \n');
fprintf(fid_abaqus, '%f, %f \n', E_film, poisson);

% Define node sets for crack front
size_x=length(crack_front);
for i =1:size_x
    fprintf(fid_abaqus, '*Nset, Nset=crack_front%d \n', i);
    fprintf(fid_abaqus, '%d, \n', i);
end

fprintf(fid_abaqus, '*Step, name=Apply displacements, nlgeom=No \n');
fprintf(fid_abaqus, '*Static \n');
fprintf(fid_abaqus, '0.001, 1., 1e-05, 1. \n');
fprintf(fid_abaqus, '*Boundary \n');
fprintf(fid_abaqus, 'nodes_bonded, PINNED \n');
fprintf(fid_abaqus, '*Include, input=displacement%.inp \n', wyko_file);
fprintf(fid_abaqus, '** OUTPUT REQUESTS \n');

```

```

fprintf(fid_abaqus, '*Restart, write, frequency=0 \n');
fprintf(fid_abaqus, '** FIELD OUTPUT \n');
fprintf(fid_abaqus, '*Output, field, frequency=4 \n');
fprintf(fid_abaqus, '*Node Output \n');
fprintf(fid_abaqus, 'CF, RF, U \n');
fprintf(fid_abaqus, '*Element Output, directions=YES \n');
fprintf(fid_abaqus, 'S, E, \n');
fprintf(fid_abaqus, '** HISTORY OUTPUT \n');
fprintf(fid_abaqus, '*Output, history, frequency=0 \n');

fprintf(fid_abaqus, '*Contour Integral, contours=%d, crack tip nodes, type=J,
frequency=99999, normal \n', no_contours);
fprintf(fid_abaqus, '0.0, 0.0, 1.0 \n');
for i =1:size_x
    fprintf(fid_abaqus, 'crack_front%d, crack_front%d \n ', i, i);
end

fprintf(fid_abaqus, '*Contour Integral, contours=%d, crack tip nodes, type=K
Factors, direction=MTS, frequency=99999, normal \n', no_contours);
fprintf(fid_abaqus, '0.0, 0.0, 1.0 \n');
for i =1:size_x
    fprintf(fid_abaqus, 'crack_front%d, crack_front%d \n ', i, i);
end

fprintf(fid_abaqus, '*End Step \n');

fclose(fid_abaqus);
save(strcat(' workspace_variab les_', wyko_fi le));
quit;

```

## Appendix D

```
** ABAQUS input script for displacement field-based finite element model
*Heading
*Preprint, echo=NO, model=NO, history=NO, contact=NO
*Node, input=mesh_ppd100.inp
*Include, input=nodes_bonded_ppd100.inp
*Element, type=C3D27
1, 75, 1, 3, 77,
7253, 7179, 7181, 7255,
38, 2, 40, 76,
7216, 7180, 7218, 7254,
3664, 3590, 3592, 3666,
3628,
39, 7217,
3627, 3591, 3629, 3665
*Elgen
1, 18, 2, 1, 40, 74, 18, 8, 7178, 720
*Element, type=C3D27
500001, 1, 3035, 3037, 3,
7179, 10213, 10215, 7181,
2998, 3036, 3000, 2,
10176, 10214, 10178, 7180,
3590, 6624, 6626, 3592,
6588,
2999, 10177,
6587, 6625, 6589, 3591
*Elgen
500001, 18, 2, 1, 1, 74, 18, 8, 7178, 18
*Element, type=C3D27
1000001, 3035, 3109, 3111, 3037,
10213, 10287, 10289, 10215,
3072, 3110, 3074, 3036,
10250, 10288, 10252, 10214,
6624, 6698, 6700, 6626,
6662,
3073, 10251,
6661, 6699, 6663, 6625
*Elgen
1000001, 18, 2, 1, 7, 74, 18, 8, 7178, 126
*Elset, elset=all_elements, generate
1, 2000000, 1
** Section: Coating
*Solid Section, elset=all_elements, material=Epoxy
1,
** MATERIAL DEFINITION
*Material, name=Epoxy
*Elastic
2700.000000, 0.320000
*Nset, Nset=crack_front1
1,
*Nset, Nset=crack_front2
2,
*Nset, Nset=crack_front3
3,
*Nset, Nset=crack_front4
4,
*Nset, Nset=crack_front5
5,
*Nset, Nset=crack_front6
6,
*Nset, Nset=crack_front7
7,
*Nset, Nset=crack_front8
8,
*Nset, Nset=crack_front9
9,
*Nset, Nset=crack_front10
10,
*Nset, Nset=crack_front11
11,
```

```

*Nset, Nset=crack_front12
12,
*Nset, Nset=crack_front13
13,
*Nset, Nset=crack_front14
14,
*Nset, Nset=crack_front15
15,
*Nset, Nset=crack_front16
16,
*Nset, Nset=crack_front17
17,
*Nset, Nset=crack_front18
18,
*Nset, Nset=crack_front19
19,
*Nset, Nset=crack_front20
20,
*Nset, Nset=crack_front21
21,
*Nset, Nset=crack_front22
22,
*Nset, Nset=crack_front23
23,
*Nset, Nset=crack_front24
24,
*Nset, Nset=crack_front25
25,
*Nset, Nset=crack_front26
26,
*Nset, Nset=crack_front27
27,
*Nset, Nset=crack_front28
28,
*Nset, Nset=crack_front29
29,
*Nset, Nset=crack_front30
30,
*Nset, Nset=crack_front31
31,
*Nset, Nset=crack_front32
32,
*Nset, Nset=crack_front33
33,
*Nset, Nset=crack_front34
34,
*Nset, Nset=crack_front35
35,
*Nset, Nset=crack_front36
36,
*Nset, Nset=crack_front37
37,
*Step, name=Apply displacements, nl geom=No
*Static
0.001, 1., 1e-05, 1.
*Boundary
nodes_bonded, PINNED
*Include, input=displacement_ppd100.inp
** OUTPUT REQUESTS
*Restart, write, frequency=0
** FIELD OUTPUT
*Output, field, frequency=4
*Node Output
CF, RF, U
*Element Output, directions=YES
S, E,
** HISTORY OUTPUT
*Output, history, frequency=0
*Contour Integral, contours=5, crack tip nodes, type=J, frequency=99999, normal
0.0, 0.0, 1.0
crack_front1, crack_front1
crack_front2, crack_front2
crack_front3, crack_front3
crack_front4, crack_front4
crack_front5, crack_front5
crack_front6, crack_front6
crack_front7, crack_front7
crack_front8, crack_front8
crack_front9, crack_front9
crack_front10, crack_front10

```

```
crack_front11, crack_front11
crack_front12, crack_front12
crack_front13, crack_front13
crack_front14, crack_front14
crack_front15, crack_front15
crack_front16, crack_front16
crack_front17, crack_front17
crack_front18, crack_front18
crack_front19, crack_front19
crack_front20, crack_front20
crack_front21, crack_front21
crack_front22, crack_front22
crack_front23, crack_front23
crack_front24, crack_front24
crack_front25, crack_front25
crack_front26, crack_front26
crack_front27, crack_front27
crack_front28, crack_front28
crack_front29, crack_front29
crack_front30, crack_front30
crack_front31, crack_front31
crack_front32, crack_front32
crack_front33, crack_front33
crack_front34, crack_front34
crack_front35, crack_front35
crack_front36, crack_front36
crack_front37, crack_front37
*Contour Integral, contours=5, crack tip nodes, type=K Factors, direction=MTS,
frequency=99999, normal
0.0, 0.0, 1.0
crack_front1, crack_front1
crack_front2, crack_front2
crack_front3, crack_front3
crack_front4, crack_front4
crack_front5, crack_front5
crack_front6, crack_front6
crack_front7, crack_front7
crack_front8, crack_front8
crack_front9, crack_front9
crack_front10, crack_front10
crack_front11, crack_front11
crack_front12, crack_front12
crack_front13, crack_front13
crack_front14, crack_front14
crack_front15, crack_front15
crack_front16, crack_front16
crack_front17, crack_front17
crack_front18, crack_front18
crack_front19, crack_front19
crack_front20, crack_front20
crack_front21, crack_front21
crack_front22, crack_front22
crack_front23, crack_front23
crack_front24, crack_front24
crack_front25, crack_front25
crack_front26, crack_front26
crack_front27, crack_front27
crack_front28, crack_front28
crack_front29, crack_front29
crack_front30, crack_front30
crack_front31, crack_front31
crack_front32, crack_front32
crack_front33, crack_front33
crack_front34, crack_front34
crack_front35, crack_front35
crack_front36, crack_front36
crack_front37, crack_front37
*End Step
```